

Electroweak Symmetry Breaking in the Era of the Higgs Boson Discovery

by

Daniele Bertolini

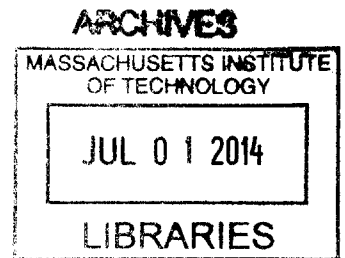
Submitted to the Department of Physics
in partial fulfillment of the requirements for the degree of

Doctor of Philosophy in Physics

at the

MASSACHUSETTS INSTITUTE OF TECHNOLOGY

June 2014



© Massachusetts Institute of Technology 2014. All rights reserved.

Signature redacted

Author

Department of Physics
May 23, 2014

Signature redacted

Certified by


Jesse Thaler
Assistant Professor of Physics
Thesis Supervisor

Signature redacted

Accepted by


Krishna Rajagopal
Associate Department Head for Education

Electroweak Symmetry Breaking in the Era of the Higgs Boson Discovery

by

Daniele Bertolini

Submitted to the Department of Physics
on May 23, 2014, in partial fulfillment of the
requirements for the degree of
Doctor of Philosophy in Physics

Abstract

In this thesis we study possible deviations from the electroweak symmetry breaking mechanism as predicted by the Standard Model (SM), and we introduce a new framework to analyze hadronic final states at colliders.

In the first part, we begin by considering supersymmetric extensions of the SM and by studying the connection between electroweak symmetry breaking and supersymmetry breaking. Contrary to the common lore, we show that a visible dynamics in the Higgs sector can contribute to supersymmetry breaking, as long as soft masses receive contributions also from one or more hidden sectors. A striking feature is the presence of a light pseudo-goldstino in the spectrum. We study potential collider signatures of visible supersymmetry breaking in Higgs and neutralino decays.

Then, we move to a study of the Higgs data collected at the Large Hadron Collider (LHC). By using both measurements of the Higgs boson couplings, and limits on Higgs-like states at higher masses, we investigate whether the data support the possibility that the SM Higgs is mixed with another scalar. We consider fits to simplified models and we find that mixing angles with $\sin^2 \theta \gtrsim 0.2$ are disfavored at 95% CL over a scalar mass range 200 – 1000 GeV.

In the second part, we propose a new way to define inclusive jet (and subjet) based observables at colliders. We introduce a new class of event shapes that characterize the jet-like structure of the event by using only information in the neighborhood of each particle. We show that conventional jet-based observables such as jet multiplicity, summed scalar transverse momentum, and missing transverse momentum can be recovered within this approach. We show that in this framework trimming can be recast as a particle weight assignment, without explicit jet identification. Finally, we comment on potential applications of the method both at trigger and analysis level.

Thesis Supervisor: Jesse Thaler
Title: Assistant Professor of Physics

Acknowledgments

I would like to thank my advisor Jesse Thaler, for his invaluable mentorship during these five years at MIT. His avid passion for physics has been an inspiration to me.

I would also like to thank Iain Stewart for teaching me QCD and for giving me the opportunity to work with him.

Finally, I would like to thank all my past and present collaborators, the entire CTP community, and my family for continuous support.

Contents

1	Introduction	13
1.1	The Standard Model: Successes and Limits	13
1.2	Outline	19
1.2.1	Visible Supersymmetry Breaking	20
1.2.2	Constraints on Singlet Extensions of the Higgs Sector	22
1.2.3	A New Approach to Jets	24
2	Visible Supersymmetry Breaking	27
2.1	Breaking Supersymmetry in the Visible Sector	27
2.1.1	Visible Sector SUSY Breaking	28
2.1.2	Hidden Sector SUSY Breaking	30
2.1.3	Soft Terms	31
2.1.4	A GeV-scale Pseudo-Goldstino?	32
2.2	Properties of the Pseudo-Goldstino	34
2.2.1	Mass with R Violation	35
2.2.2	Width with R Violation	38
2.2.3	The R-symmetric Case	40
2.3	Cosmological Constraints	43
2.4	Collider Phenomenology	44
2.4.1	The Pseudo-Sgoldstino	45
2.4.2	Modified Higgs Decays	47
2.4.3	Modified Neutralino Decays	50
2.5	Conclusions	52

3	Constraints on Singlet Extensions of the Higgs Sector	55
3.1	Higgs Friends and Accomplices	55
3.2	Statistical Methodology	58
3.2.1	Likelihood Estimation	58
3.2.2	Likelihood for Multiple Scalars	60
3.2.3	Estimating the Importance of Signal Overlap	64
3.3	Results	65
3.3.1	Data	65
3.3.2	Higgs Friend and Higgs Accomplice Scenarios	66
3.4	Electroweak Precision Constraints	67
3.5	Conclusions	69
4	A New Approach to Jets	71
4.1	Event Shapes for Inclusive Jet Observables	72
4.2	Characterizing Individual Jets	79
4.2.1	Jet Transverse Momentum	79
4.2.2	Jet Axes and Constituents	82
4.3	Shape Trimming	87
4.4	Generalizations	93
4.4.1	Other Jet-like Event Shapes	93
4.4.2	Subjet-like Jet Shapes	96
4.4.3	Subjet-like Event Shapes	97
4.5	Conclusions	99
5	Conclusions	103
A	One-Loop Pseudo-Goldstino Mass	105
B	Dominant Pseudo-Goldstino Annihilation Channel	109
C	Neutralino Decay Widths	111
D	Inverting Jet Multiplicity	113

List of Figures

1-1	Standard SUSY paradigm versus visible SUSY breaking	21
2-1	Estimate of the loop correction to the pseudo-goldstino mass	36
2-2	Mass of the pseudo-goldstino as a function of the parameters of the soft parameters	37
2-3	Mixing angle of the pseudo-goldstino with gauginos as a function of the soft parameters	38
2-4	Dominant decay mode for the pseudo-goldstino in the R -violating case	40
2-5	An illustration of the pseudo-goldstino mass as a function of the soft mass \tilde{m}_X	45
2-6	Representative diagrams that modify the Higgs width	47
2-7	Example of modified Higgs branching ratios	48
2-8	Representative diagrams contributing to the decays of a neutralino LOSP	50
2-9	Example of branching ratios for a neutralino LOSP as a function of its mass in the R -violating case	51
3-1	Relevance of the overlap between Higgs and Higgs friend signals . . .	64
3-2	95% confidence limits on the mixing angle as a function of the scalar mass for the Higgs friend and Higgs accomplice scenarios	67
3-3	Best fit points and confidence contours for $\sin \theta$ and α when the Higgs accomplice is beyond collider reach	68
3-4	Electroweak precision constraints	68
4-1	Strategy for defining jet based observables without clustering	74

4-2	Jet multiplicity for QCD dijet events	75
4-3	Summed scalar transverse momentum for QCD dijet events	76
4-4	Missing transverse momentum for $Z(\rightarrow \nu\bar{\nu}) + j$ events	76
4-5	Average jet transverse momentum for QCD dijet events	77
4-6	Missing transverse momentum significance for $Z(\rightarrow \nu\bar{\nu}) + j$ events . .	78
4-7	Number of jet as a function of $p_{T\text{cut}}$ for fixed R	80
4-8	Transverse momentum of the three hardest jets for QCD dijet events	81
4-9	Number of jets as a function of R for a single QCD dijet event	82
4-10	Two QCD dijet event displays	86
4-11	Position of the hardest jet axis for QCD dijet events	88
4-12	Comparison of the hardest jet found with anti- k_T and the hybrid event shape result, all for QCD dijet events	88
4-13	Boosted top sample and corresponding QCD background	91
4-14	Pileup mitigation for $Z(\rightarrow \nu\nu) + j$ events	92
4-15	Summed transverse momentum inverse for QCD dijet events	94
4-16	Summed jet mass analysis	94
4-17	Subjet multiplicity on a boosted top sample	97
4-18	Summed subjet multiplicity on a QCD four-jet sample	98
A-1	One-loop self-energy diagrams contributing to the pseudo-goldstino mass	106
B-1	Pseudo-goldstino dominant annihilation channel	109
C-1	Neutralino LOSP decay to a pseudo-goldstino	111

List of Tables

2.1	The R -charge assignments for the minimal model of visible sector SUSY breaking.	28
3.1	Approximate light Higgs search mass resolutions	64

Chapter 1

Introduction

1.1 The Standard Model: Successes and Limits

The Standard Model (SM) of particle physics is a quantum field theory that describes the interactions of fundamental constituents of matter. Since its original formulation in the sixties by Glashow, Weinberg, and Salam [103, 161, 146, 147] a variety of experiments have probed its validity at increasingly higher energies. The SM provides a description of electromagnetic, weak, and strong interactions approximately up to energies $E \sim \mathcal{O}(10^2 \text{ GeV})$, or equivalently distances $d \sim \mathcal{O}(10^{-18} \text{ m})$. It is able to describe at unprecedented accuracy an enormous variety of phenomena at subatomic and subnuclear distances. However, as experimental evidences for the theory were building up, a series of open questions also started to emerge. This motivated, over the past twenty years, an intense theoretical and experimental effort in studying extensions of the SM, which generically go under the name of Beyond the Standard Model physics (BSM). In this thesis we will present results both within the SM and BSM frameworks.

Let us begin by briefly recall the structure of the SM. The SM is a gauge quantum field theory based on the gauge group

$$SU(2)_L \times U(1)_Y \times SU(3)_C. \tag{1.1}$$

$SU(2)_L \times U(1)_Y$ describes electroweak interactions, and $SU(3)_C$ describes strong interactions. The lagrangian can be written schematically in a few lines:

$$\begin{aligned} \mathcal{L}_{\text{SM}} = & -\frac{1}{4}F_{\mu\nu}^a F^{\mu\nu a} + i\bar{\psi}\not{D}\psi \\ & + |D_\mu H|^2 - V(H) \\ & + \lambda_{ij}\bar{\psi}_i\psi_j H + \text{h.c.} \end{aligned} \tag{1.2}$$

The first line describes the dynamics of the gauge fields and their interactions with fermions. The second line describes the spontaneous breaking of the electroweak symmetry through the Higgs field H . Finally, the last line describes interactions of the fermions with the Higgs field, including fermion mass terms. We will refer to these interactions as the flavor sector. The form of the lagrangian Eq. (1.2) is dictated by locality, Lorentz invariance and gauge invariance under Eq. (1.1).

The Higgs sector has been only partially probed so far. Indeed, electroweak symmetry breaking takes place at energies $E \sim \mathcal{O}(10^2 \text{ GeV})$, which are being explored for the first time by the Large Hadron Collider (LHC). At present, the major discovery of the LHC has been the observation of an elementary scalar with a mass $m_h \simeq 126 \text{ GeV}$, consistent with the Higgs boson, the scalar excitation of the Higgs field H [9, 51].

As said, there are several open questions in the SM. Some of them are more concerned with the theoretical structure of the theory, others more related to experimental evidences. Broadly speaking, with “theoretical issues” we mean unsatisfactory features of the SM given its matter and interaction content. Let us mention a few examples:

- **Charge quantization.** If one regards the symmetry Eq. (1.1) as classical, the hypercharge assignment under $U(1)_Y$ is arbitrary. That is, abelian gauge invariance does not constrain charges, as opposed to non-abelian gauge invariance where the couplings of different matter representations with the gauge bosons are fixed in terms of a single coupling constant. Hypercharges of different fermion representations have to be set by hand to match the observed

electromagnetic charges. This arbitrariness is partially resolved when considering the full quantum theory. In this case, the cancellation of anomalies for the gauge group in Eq. (1.1) requires the quantization of the charge. However, it suffices to modify the matter content of the SM by adding a single Weyl spinor (e.g. a right-handed neutrino field) to relax the quantization condition and allow again for arbitrary charges, while keeping the theory anomaly free. As pointed out, the failure of the SM in predicting unambiguously charge quantization is inherent to the abelian factor in Eq. (1.1). The most promising solution to this problem consists of embedding the SM gauge group into a larger non-abelian group, with $SU(5)$ being the minimal candidate.

- **Strong CP problem.** Quantum chromodynamics (QCD) is the part of the SM that describes strong interactions. Due to its non-trivial vacuum structure, QCD lagrangian contains a term $\mathcal{L}_\theta = \frac{\theta}{16\pi^2} F_{\mu\nu}^a \tilde{F}^{\mu\nu a}$, with $0 \leq \theta < 2\pi$ specifying the vacuum of the theory. Since \mathcal{L}_θ violates CP, the size of θ is experimentally constrained (mainly) by neutron electric dipole moment measurements. Current limits are as stringent as $\theta \lesssim 10^{-10}$. The fact that this unnaturally small value has to be set by hand is known as the strong CP problem. Several solutions have been studied, probably the most well known is the introduction of a new dynamical field called the axion [139, 140, 163, 162].
- **Naturalness.** The naturalness problem is related to the presence of a scalar in the spectrum of the SM. Specifically, the mass of the scalar is not protected by any symmetry, so that it potentially receives quantum corrections proportional to high energy thresholds (as opposed to fermions for which chiral symmetry limits the sensitivity to energy thresholds to be only logarithmic). This would set the natural value for the Higgs mass at the scale of this high energy thresholds (for example at M_{Planck} , where quantum gravity becomes relevant). The unexplained hierarchy between the Higgs mass (or equivalently the electroweak scale) and the Planck scale (or any other lower threshold) is known as the naturalness problem. A large fraction of particle physics research has been devoted

to study solutions to this problem over the past two decades. Remarkably, solutions to the naturalness problem require the presence of new particles and interactions at energies not too far from the electroweak scale. This is what ultimately motivated the construction of the LHC. On one side, the discovery of what seems to be an elementary Higgs boson by the LHC, reinstates the naturalness problem. On the other side however, the lack of any evidence of new physics, puts naturalness as a guiding principle for new physics under increasing pressure. Supersymmetry is one of the most appealing solutions to the naturalness problem. In particular, we shall return to supersymmetry and its connections to electroweak symmetry breaking in Chapter 2.

- Flavor puzzle. Fermion masses and mixings between generations show a non trivial hierarchical structure. Such a structure is accounted for in the SM by setting by hand the appropriate yukawa couplings λ_{ij} in the last line of Eq. (1.2). The origin of such structure, which could possibly originate from a symmetry breaking pattern, is known as the flavor puzzle.
- Cosmological constant. Measurements of the Cosmic Microwave Background (CMB) and of the current acceleration of the universe indicate a non vanishing, albeit small, cosmological constant. The measured vacuum energy density is $\rho_\Lambda \sim \mathcal{O}(\text{meV}^4)$. Depending on the choice of the cutoff, known contributions from the SM to the vacuum energy density are off by 60 to 120 orders of magnitude. This discrepancy is known as the cosmological constant problem.

These “theoretical issues” are all related to free parameters of the SM that need to be fixed by some experimental measurement. One might think that these represent minor problems, in the sense that once the parameters are fixed we are left with a well-defined and predictive theory. Indeed, if we regard the SM as an effective field theory, using experimental data to fix parameters is a standard procedure. However, we could rephrase the issues above by asking whether and how these parameters are linked to some fundamental symmetry of the theory at higher energies. Then, we

would like to know what the cutoff of the effective theory is and whether we will be able to probe the more fundamental structure of the theory.

A second category of shortcomings of the SM are related to direct experimental evidences that (most likely) require an extension of the matter and/or interaction content. Examples are:

- **Dark Matter.** Astrophysical measurements (e.g. rotational curves of galaxies, CMB anisotropies spectrum, gravitational lensing) show very strong evidence for a non-baryonic component of matter in the Universe. Such a component, named dark matter, makes up 26% of the energy content of the Universe today. Dark matter cannot be accounted for within the SM field content.
- **Neutrino mass and matter-antimatter asymmetry.** Neutrino flavor oscillations suggest that neutrinos have mass. There are several ways to implement a neutrino mass which either require the extension of the SM field content (e.g. with right-handed neutrinos) or the introduction of higher dimensional operators in Eq. (1.2), which again would signal new physics above some cutoff scale. Also, a related problem in the flavor sector, is the amount of CP-violation. CP-violation in the SM seems to be not enough to explain the observed matter-antimatter asymmetry in the Universe. Again, this would require some modification of the SM.
- **Quantum gravity.** The SM can be augmented with classical general relativity to account for gravitational interactions. More generally, at energies $E \ll M_{\text{Planck}} \sim 10^{18}$ GeV, quantum gravity effects can be consistently included within an effective field theory approach. However, above M_{Planck} , a full quantum theory of gravity is required. As general relativity is not renormalizable, a modification of the SM is necessary. As pointed out in [121], the recent observation of primordial gravitational waves through B-mode polarization of the CMB [16], if confirmed, would represent a genuine quantum gravity effect thus confirming that gravity, like the other interactions, must obey the laws of quantum mechanics and a coherent quantum description must exist.

There are several other open questions in the SM. The goal here is to provide the reader with a sense of the vibrant and active research environment of particle physics today, rather than giving a complete inventory. Moreover, one expects those two “theoretical” and “experimental” categories to be connected, with the ultimate goal of solving all the issues within a unique and coherent framework. There are several examples of this interplay, let us mention a few. Supersymmetry provides a solution to the naturalness problem, but also provides candidates for dark matter and hints for a unification of the couplings. Axions would solve the strong CP problem, but would also be dark matter candidates. A theory of quantum gravity could help solving the cosmological constant problem.

In searching for solutions to the SM shortcomings we need inputs from experiments. Current experiments are commonly grouped according to three categories. Experiments at the energy frontier probe previously unexplored energy scales. The LHC is the largest experiment at the energy frontier and it explores for the first time the electroweak scale up to 14 TeV. At the intensity frontier experiments accumulate intense beams of particles to study rare processes. Although the typical energy scale is much lower than for experiments at the energy frontier, studying very rare processes gives access to higher dimensional operators in the SM and so can give indirect information about the physics at very high energy scales, typically much higher than those directly accessible at the energy frontier. Finally, the cosmic frontier is the realm of astrophysical observations and measurements. Basically, the visible Universe itself serves as a laboratory.

A separate discussion concerns the theory of strong interactions. Although QCD is a complete and well established theory of strong interactions and it has been probed by several experiments over the past fifty years, we do not fully understand its incredibly rich dynamics yet. At high energies QCD is essentially a theory of free quarks and gluons (this property is known as asymptotic freedom). Interactions can be accounted for in a systematic way by using perturbation theory. Instead, at energies $E \lesssim \Lambda_{\text{QCD}} \sim 200 \text{ MeV}$ (or distances roughly larger than the size of the proton), QCD exhibits confinement and we observe colorless bound states. In this regime the the-

ory becomes strongly coupled and much harder to treat analytically. Several tools have been developed, like lattice simulations, large- N expansion, AdS/CFT correspondence, effective field theories valid in particular regimes (e.g. chiral perturbation theory, heavy quark effective theory, soft collinear effective theory). Such a rich dynamics is reflected into a complex phase diagram. Dedicated experiments explore exotic phases of QCD, such as the quark-gluon plasma.

On the other hand, QCD has a crucial role in collider experiments that search for new physics at the electroweak scale. Colliding particles can be hadrons, as for the case of the LHC, but even more importantly quarks and gluons can be produced in the final state of the collision. As an example, a SM Higgs boson with a mass $m_h \sim 126$ GeV, has a branching ratio into pairs of b -quarks $\text{BR}(h \rightarrow b\bar{b}) \sim 57\%$. Because of confinement, we can only observe hadrons in the final state. Jets are clusters of hadrons and are used as a proxy for the original partons produced in the hard interaction. For a center of mass energy $E_{\text{CM}} \gg \Lambda_{\text{QCD}}$, jet physics is remarkably for the most part based on perturbative QCD.

In this thesis we will focus both on BSM extensions of the electroweak symmetry breaking mechanism, and on jet physics. In the next section we will introduce the reader to the topics studied in this thesis in more detail.

1.2 Outline

Chapters 2 and 3 of this thesis are concerned with the electroweak symmetry breaking mechanism. In Chapter 2 we will analyze the relationship between electroweak symmetry breaking and supersymmetry breaking and its phenomenological and cosmological consequences [34]. In Chapter 3 we will use Higgs measurements performed at the LHC to constrain non minimal Higgs sectors [33]. In Chapter 4 we will introduce a new way to treat hadronic final states at hadron colliders [32].

1.2.1 Visible Supersymmetry Breaking

Spontaneously broken supersymmetry (SUSY) is an appealing solution to the naturalness problem. In particular, by relating fermionic and bosonic states, it enforces cancellations in radiative corrections to the scalar masses and weakens their sensitivity to higher energy thresholds. Supersymmetry must be broken in Nature, as we do not observe partners of known particles with the same mass and with different spin. Essentially, the many different ways SUSY can be broken give rise to the plethora of different supersymmetric models studied in literature.

A crucial question for SUSY phenomenology is how SUSY breaking is communicated to the Supersymmetric Standard Model (SSM). The well-known supertrace sum rule prohibits SUSY breaking from occurring directly in the SSM through renormalizable tree-level interactions [108, 132, 128]. This observation has led to the standard two-sector paradigm, where a hidden sector is responsible for SUSY breaking, and the visible sector (i.e. the SSM) feels SUSY breaking indirectly via messenger fields.

Recently, it has been argued that the standard two-sector paradigm may be too restrictive, as there could exist multiple hidden sectors which independently break SUSY [58]. A striking signature of this proposal is that if SUSY is broken by N independent sectors, then there is a corresponding multiplicity of “goldstini”. One linear combination is eaten to form the longitudinal component of the gravitino, while the remaining $N - 1$ modes remain in the spectrum as uneaten goldstini.¹ Motivated by the possibility of multiple SUSY breaking, we reexamine the usual assumption that SUSY cannot be broken in the visible sector. As long as there are one or more hidden sectors contributing to SSM soft masses, then the supertrace sum rule constraint does not apply, and SUSY can indeed be broken in the SSM at tree-level. This leads to an uneaten goldstino in the visible sector. The uneaten goldstino mixes with SSM fields, but despite this mixing, there is still a light mass eigenstate which we refer to as a pseudo-goldstino. For concreteness, we study the simplest example of visible

¹The phenomenological implications of goldstini have been studied in detail in Refs. [58, 57, 69, 133, 54, 116, 22, 154, 56]. The idea of pseudo-goldstinos first appeared in the context of brane-worlds in Ref. [29].

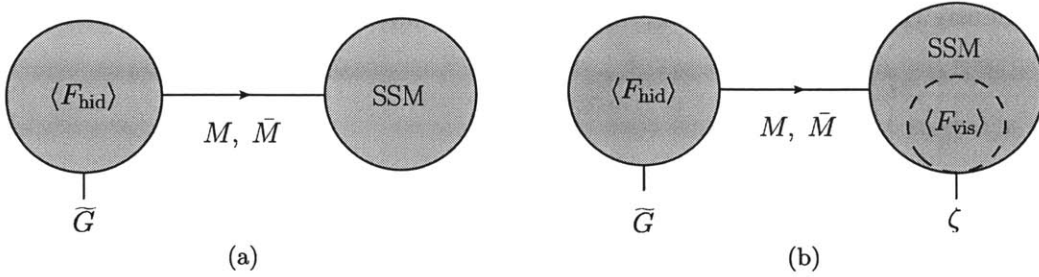


Figure 1-1: Left: In the standard paradigm, SUSY is broken in the hidden sector and communicated to the visible sector via messenger fields. The hidden sector goldstino is eaten by gravitino \tilde{G} . Right: SUSY can also be broken in the visible sector, giving rise to a visible pseudo-goldstino ζ . To evade the supertrace sum rule, there must be additional SSM soft masses mediated from the hidden sector. While the standard assumption is that this mediation is R -violating, we will also consider R -symmetric mediation.

sector SUSY breaking from Ref. [116], where the minimal R -symmetric SSM [122] is extended to allow for F -term breaking. The generic setup we envision is shown in Fig. 1-1.

The phenomenology of the pseudo-goldstino depends sensitively on its mass, which in turn depends on how hidden sector SUSY breaking is mediated to the SSM. In the usual case with R -violating SSM soft parameters, the pseudo-goldstino has a mass of $\mathcal{O}(10 \text{ MeV} - 1 \text{ GeV})$, which implies significant cosmological constraints. Thus, the standard lore that SUSY cannot be broken in the (R -violating) SSM is essentially correct, albeit not because of the supertrace sum rule but because of pseudo-goldstino overproduction in the early universe. That said, there are small corners of parameter space with healthy pseudo-goldstino cosmology.

On the other hand, if the mediation mechanism preserves an R -symmetry, then the pseudo-goldstino will only get a mass from (R -violating) supergravity (SUGRA) effects proportional to $m_{3/2}$. Thus, if the gravitino \tilde{G} is sufficiently light (as expected to avoid the cosmological gravitino problem [137]), then the pseudo-goldstino is also cosmologically safe. There are potential collider implications for the R -symmetric limit, since the light pseudo-goldstino ζ is typically accompanied by a light pseudo-goldstino ϕ . We find that, if kinematically allowed, the physical Higgs boson h^0 would

dominantly decay invisibly as $h^0 \rightarrow \phi\phi \rightarrow \zeta\tilde{G}\zeta\tilde{G}$, affecting Higgs phenomenology at the LHC.

1.2.2 Constraints on Singlet Extensions of the Higgs Sector

The discovery of the Higgs boson [9, 51] represents a fundamental step forward in our understanding of the dynamics of electroweak symmetry breaking. A crucial question is whether the observed Higgs boson shows deviations from the couplings predicted in the SM. From a theoretical perspective some modification of Higgs physics has long been expected, since substantial theoretical motivation for BSM physics is aimed at resolving the naturalness problem, which is concerned with the Higgs sector. Solutions to this problem often require the existence of additional electroweak-charged states and/or additional scalars coupled to, or mixed with, the Higgs.

Even if one abandons the naturalness problem as motivation there is always the possibility that additional hidden sectors exist, perhaps related to dark matter or baryogenesis. The Higgs sector of the SM contains a super-renormalizable Lorentz and gauge invariant operator, which can easily accommodate couplings to new hidden sector physics, the so-called ‘Higgs Portal’ [149, 134, 38, 75, 138, 131, 19, 143, 112, 129, 94, 27, 82, 130]. Such couplings may allow for Higgs decays to neutral particles, leading to an additional invisible width for the Higgs. The main consequence of this scenario is that all detectable branching ratios become equally suppressed, leading to a democratic reduction in the Higgs signal rates. In addition to this, hidden sector scalars can also mix with the Higgs through the Higgs portal interaction.

Motivated by these simple considerations we study the implications of the LHC Higgs searches on simple models of a singlet scalar mixed with the Higgs. If additional neutral scalars mix with the Higgs the mass eigenstates and interaction eigenstates are not aligned and the properties of the Higgs are altered, similar to the so-called ‘Higgs look-alike’, or ‘Higgs Friend’ scenario [79, 98, 115, 78, 107].² If this mixing

²Although we do not assume that the neutral scalars have couplings to extra colored particles, as in [98], the scenario considered here is sufficiently similar in spirit to the proposals in [98] that we adopt the ‘Higgs Friend’ terminology.

alone is present the individual branching ratios of the Higgs remain the same and the production of the Higgs is suppressed. The overall effect is thus, at the level of the current Higgs searches, indistinguishable from the case where the Higgs has an additional invisible width. However, with careful study the two can be distinguished. For example, an invisible width can be measured by searching for mono-jet signals coming from initial state radiation in Higgs production [87, 81, 76, 77, 152, 82]. On the other hand, mixing with a neutral scalar can be confirmed more directly by searching for the extra scalar, exploiting the fact that it inherits many properties of the Higgs. In this work we are concerned with the latter scenario. We assume a Higgs boson with mass of 125.5 GeV, and then consider limits from the Higgs searches on a Higgs friend. Of course, it is plausible that the friend might be much more massive and thus effectively decoupled, in which case it would be very difficult to unambiguously confirm its presence. We consider fits to this scenario as well. We will also consider the addition of charged vector-like fields, which could be scalar or fermionic, and couple to the Higgs friend.³ This interaction enhances the coupling of the friend to photons at one-loop. Once the Higgs mixes with the friend this can enhance the Higgs decays to photons. We call this the ‘Higgs accomplice’ scenario.

Although simplified, we believe these models should map on to some theoretically motivated scenarios, such as the Next to Minimal Supersymmetric Standard Model (NMSSM) where the Higgs mixes with an extra singlet which has and induced coupling to photons through its Yukawa coupling to charged Higgsinos.

In order to test the viability of the Higgs friend and Higgs accomplice scenarios it is necessary to confront these models with data. There has been significant interest in determining how best to extract Higgs couplings from the data, leading to a number of studies [24, 45, 96, 100, 23, 127, 65, 99, 37, 86, 135, 95, 46]. We do this by approximating the likelihood functions for the Higgs signal strength in particular decay channels by using the best fit values provided by the collaborations. This information can then be used to estimate confidence contours for the models considered. We also

³It is often the case that additional electroweak-charged fields are present in extensions of the SM Higgs sector, so the introduction of extra charged fields is a plausible augmentation of the Higgs friend scenario.

define a method to estimate the cross contamination between the two Higgs-like signals due to finite mass resolution. Given that the contamination cannot be precisely quantified, we determine a mass region where it can be safely neglected.

We find that, even if still compatible with data, both the Higgs friend and Higgs accomplice scenarios are already very constrained. Mixing angles with $\sin^2 \theta \gtrsim 0.2$ are excluded at 95% CL over the mass range 200 – 1000 GeV. A substantial improvement in sensitivity comes from combining Higgs coupling measurements with exclusion limits set at higher masses.

1.2.3 A New Approach to Jets

When quarks and gluons are produced in high energy particle collisions, they undergo a process of showering and hadronization, and the resulting final state can be organized in terms of clusters of hadrons called jets. Jets play a key role at experiments like the LHC, both for testing SM physics and for searching for new phenomena beyond the SM. At present, most jet studies at the LHC are based on jets identified with a jet algorithm [88, 148]. Algorithms such as anti- k_T [42] cluster final state hadrons into jet objects, whose four-momenta are then used as inputs for subsequent analyses. An alternative approach is provided by event shape observables, which are functions involving all final state hadrons in a collision event. Event shapes were extensively used for precision tests of QCD at e^+e^- colliders [74, 113, 13, 15, 12], and various event shapes have been proposed and used at hadron colliders [25, 26, 11, 118, 8].

Here, we will blur the distinction between jet algorithms and event shapes by constructing jet-like event shapes. These event shapes incorporate a jet-like radius R as well as a jet-like transverse momentum cut $p_{T\text{cut}}$, and they can be viewed as counterparts to some of the most commonly used jet-based observables. While these event shapes do not involve any kind of clustering procedure, they are correlated with their jet-based cousins and yield comparable information about the jet-like structure of an event. We will mainly discuss jet-like event shapes, but the generalization to subjet-like jet shapes is straightforward, with potential applications in jet substructure studies [14, 17].

We will start by constructing three jet-like event shapes that mirror the three inclusive jet observables—jet multiplicity, summed scalar transverse momentum, and missing transverse momentum—that appear ubiquitously in jet studies at both the trigger and analysis levels. For example, we will construct the jet multiplicity event shape as

$$\tilde{N}_{\text{jet}}(p_{T\text{cut}}, R) = \sum_{i \in \text{event}} \frac{p_{Ti}}{p_{Ti,R}} \Theta(p_{Ti,R} - p_{T\text{cut}}), \quad (1.3)$$

where $p_{Ti,R}$ is the transverse momentum contained in a cone of radius R around particle i . Our technique for building jet-like event shapes can be generalized to a broad class of inclusive jet observables, namely observables built as a sum over all jets in an event.

We will then show how to manipulate these event shapes to characterize individual jets. By inverting \tilde{N}_{jet} , we can characterize the p_T of the n -th hardest jet without explicitly identifying the set of hadrons that form that jet. Of course, for practical jet studies, one often wants to know the actual constituents of a jet. Since our jet-like event shapes do not have a natural clustering interpretation, we develop a hybrid method that incorporates local jet clustering into an “event shape density”. The integral over this density gives the corresponding event shape, but the density distribution itself has spikes in the direction of candidate jet axes.

A perhaps surprising application of our method is for jet grooming [40, 92, 93, 123]. Jet grooming methods aim to mitigate the effects of jet contamination from initial state radiation, underlying event, and pileup by removing soft wide-angle radiation from a jet. In the case of pileup, one can use jet grooming in concert with area subtraction techniques [41, 43, 151]. Here, we show how jet trimming [123] can be recast as an event shape. Our method is equivalent to assigning a weight to every particle in the event of

$$w_i = \Theta \left(\frac{p_{Ti,R_{\text{sub}}}}{p_{Ti,R}} - f_{\text{cut}} \right) \Theta(p_{Ti,R} - p_{T\text{cut}}). \quad (1.4)$$

This “shape trimming” method involves the same f_{cut} and R_{sub} parameters as the original “tree trimming” procedure, but does not require the explicit identification of jets or subjets.

There are a number of potential applications for these jet-like event shapes. At the trigger level, they offer a “local” way to characterize the gross properties of an event. By local, we mean that the event shape is defined as a sum over regions of interest of radius R , without needing global clustering information. This local structure allows for efficient parallel computation of the event shape. If desired, one could even include (local) pileup suppression at the trigger level by incorporating (local) trimming. At the analysis level, these event shapes offer an alternative way to characterize jets in regions of phase space where jets are overlapping. In particular, whereas standard jet algorithms always give an integer value for the jet multiplicity N_{jet} , the corresponding event shape \tilde{N}_{jet} in Eq. (1.3) typically returns a non-integer value, reflecting the inherent ambiguity in defining jets. At minimum, one can use these event shapes to test the robustness of standard jet selection criteria, since a cut on the jet-like event shape should give similar results to a cut on jet objects for the same value of R and $p_{T\text{cut}}$. Ultimately, one would like to study the analytic properties of these jet-like event shapes in perturbative QCD, though such studies are beyond the scope of the work presented here.

We also provide an implementation of all event shapes described in this chapter as an add-on to FASTJET 3 [44] as part of the FASTJET contrib project, which can be found at <http://fastjet.hepforge.org/contrib/>.

Chapter 2

Visible Supersymmetry Breaking

This chapter is organized as follows: in Sec. 2.1, we describe the simplest model of visible sector SUSY breaking, and discuss R -violating and R -symmetric mediation. In Sec. 2.2, we calculate the mass and lifetime of the pseudo-goldstino for both types of mediation. We discuss cosmological constraints in Sec. 2.3 and LHC signatures in Sec. 2.4. We conclude in Sec. 2.5, leaving calculational details to the appendices. We will use the superfield formalism, for a pedagogical introduction refer to e.g. [132, 35]. This chapter is based on [34].

2.1 Breaking Supersymmetry in the Visible Sector

There are a variety of models which break SUSY at tree-level, generalizing the familiar O’Raifeartaigh model. To truly have SUSY breaking in the visible sector, SUSY breaking must involve SSM multiplets in some way. Because gauge quantum numbers restrict the types of interactions possible, it is most natural for SUSY breaking to involve just the Higgs multiplets of the SSM.

In this section, we review the minimal model of visible sector SUSY breaking previously studied in Ref. [116], and identify the pseudo-goldstino mode. We then introduce the effects of the hidden sector, and explain why the pseudo-goldstino remains light even in the presence of SSM soft masses. Though we will confine our discussion to the minimal model, more general SUSY breaking scenarios are likely

Superfield	$U(1)_R$
H_u, H_d	0
Q, U^c, D^c, L, E^c	1
R_u, R_d, X	2

Table 2.1: The R -charge assignments for the minimal model of visible sector SUSY breaking.

to share much of the same phenomenology, since our analysis is largely based on the symmetries of the low energy theory. The key ingredient is a pseudo-goldstino of R -charge 1 that can mix with higgsino and gaugino modes after electroweak symmetry breaking.

2.1.1 Visible Sector SUSY Breaking

The minimal model of visible sector SUSY breaking is [116]

$$\mathcal{W} = \mathcal{W}_{\text{Yukawa}} + X(\lambda H_u H_d - \kappa) + \mu_u H_u R_u + \mu_d H_d R_d, \quad (2.1)$$

where the standard Yukawa interactions are

$$\mathcal{W}_{\text{Yukawa}} = y_u Q H_u U^c + y_d Q H_d D^c + y_e L H_d E^c. \quad (2.2)$$

Like the minimal R -symmetric SSM, there are two sets of Higgs doublets $H_{u,d}$ and $R_{u,d}$ with vector-like mass terms. Like the next-to-minimal SSM, there is a gauge singlet field X . This superpotential respects a $U(1)_R$ symmetry with the charge assignments in Table 2.1. We will not dwell on the ultraviolet (UV) origin of the mass parameters in Eq. (2.1), though such mass terms are often dynamically generated in composite Higgs theories [111, 49, 80, 70, 71].¹

In the absence of SSM soft masses, Eq. (2.1) spontaneously breaks SUSY. The

¹We note that the μ -terms in Eq. (2.1) are consistent with being generated by the Giudice-Masiero mechanism [101], however κ is not.

electromagnetically neutral part of the tree-level scalar potential is:

$$V_{\text{vis}} = V_F + V_D, \quad (2.3)$$

where

$$V_F = |\lambda h_u^0 h_d^0 - \kappa|^2 + |\lambda x h_d^0 + \mu_u r_u^0|^2 + |\lambda x h_u^0 + \mu_d r_d^0|^2 + \mu_u^2 |h_u^0|^2 + \mu_d^2 |h_d^0|^2, \quad (2.4)$$

$$V_D = \frac{1}{8}(g^2 + g'^2) \left(|h_u^0|^2 - |h_d^0|^2 + |r_d^0|^2 - |r_u^0|^2 \right)^2, \quad (2.5)$$

and we use a notation where lower-case characters stand for the scalar components of the corresponding superfield.

Since there is no way to simultaneously satisfy all of the F -term equations of motion, SUSY is spontaneously broken. At tree-level, there are two types of minima in terms of $(x, h_u^0, h_d^0, r_u^0, r_d^0)$:

- SUSY breaking but gauge-preserving minima: $\text{Min}_1 = (\langle x \rangle, 0, 0, 0, 0)$;
- SUSY breaking and gauge-breaking minima: $\text{Min}_2 = (\langle x \rangle, \langle h_u^0 \rangle, \langle h_d^0 \rangle, \langle r_u^0 \rangle, \langle r_d^0 \rangle)$.

Formulas for the gauge-breaking minima appear in Ref. [116]. In both cases, the x flat direction is lifted by quantum corrections and the vacuum expectation value (vev) $\langle x \rangle$ is stabilized at zero. Since $\langle r_u^0 \rangle$ and $\langle r_d^0 \rangle$ are proportional to $\langle x \rangle$, both kinds of minima preserve the R -symmetry of Table 2.1.

Notice that the R -symmetry predicts three massless neutral fermions at tree level. This is because only two linear combinations of the the R -charge +1 fermions $(\tilde{x}, \tilde{r}_u^0, \tilde{r}_d^0, \tilde{B}, \tilde{W}_3)$ can marry the two R -charge -1 fermions $(\tilde{h}_u^0, \tilde{h}_d^0)$ to make R -invariant Dirac masses. Therefore, three linear combinations of the R -charge +1 fermions must be massless. Spontaneous SUSY breaking ensures that one of the three massless states is the visible sector goldstino:

$$\chi_{\text{vis}} \simeq \langle F_X \rangle \tilde{x} + \langle F_{R_u} \rangle \tilde{r}_u^0 + \langle F_{R_d} \rangle \tilde{r}_d^0 + \langle D_Y \rangle \tilde{B} + \langle D_3 \rangle \tilde{W}_3, \quad (2.6)$$

where $\langle F_{R_u} \rangle$, $\langle F_{R_d} \rangle$, $\langle D_Y \rangle$, and $\langle D_3 \rangle$ are only non-vanishing for the gauge-breaking

minima. Note that because of the preserved R symmetry, the $H_{u,d}$ multiplets do not have F -components in the vacuum. The other two massless fermions correspond roughly to the bino and wino of the SSM.

2.1.2 Hidden Sector SUSY Breaking

In order to evade the supertrace sum rule, Eq. (2.1) must be augmented by hidden sector SUSY breaking. Regardless of the details of the hidden sector dynamics, this implies a hidden sector goldstino χ_{hid} in addition to the visible sector goldstino χ_{vis} . One linear combination is eaten via the super-Higgs mechanism to form the longitudinal component of the gravitino

$$\chi_{\text{eaten}} = \frac{\langle F_{\text{vis}} \rangle \chi_{\text{vis}} + \langle F_{\text{hid}} \rangle \chi_{\text{hid}}}{F}, \quad (2.7)$$

where $F_{\text{vis}} \equiv \sqrt{V_{\text{vis}}}$ and $F_{\text{hid}} \equiv \sqrt{V_{\text{hid}}}$ are the respective contributions to SUSY breaking from the visible and hidden sectors, and the total amount of SUSY breaking is

$$F \equiv \sqrt{\langle F_{\text{vis}} \rangle^2 + \langle F_{\text{hid}} \rangle^2}. \quad (2.8)$$

In the limit where the visible and hidden sectors are completely sequestered, the orthogonal combination of fermions

$$\chi_{\text{uneaten}} = \frac{\langle F_{\text{hid}} \rangle \chi_{\text{vis}} - \langle F_{\text{vis}} \rangle \chi_{\text{hid}}}{F} \quad (2.9)$$

is an uneaten goldstino. After zeroing the cosmological constant, the gravitino mass is

$$m_{3/2} = \frac{F}{\sqrt{3}M_{\text{Pl}}}, \quad (2.10)$$

and the uneaten goldstino gets a mass proportional to $m_{3/2}$ from SUGRA effects [58, 56].

Taking $m_{3/2}$ to be much smaller than the weak scale, the fermionic spectrum contains two light states, the gravitino and the uneaten goldstino. For the rest of the chapter, we assume $\langle F_{\text{vis}} \rangle \ll \langle F_{\text{hid}} \rangle$ such that $\chi_{\text{eaten}} \simeq \chi_{\text{hid}}$ and $\chi_{\text{uneaten}} \simeq \chi_{\text{vis}}$ in the sequestered limit.

2.1.3 Soft Terms

To generate SSM soft terms, the hidden and visible sectors cannot be completely sequestered and must interact via messengers. The leading phenomenological effect of the messenger sector can be captured by the resulting SSM soft terms. The soft terms consistent with SSM charge assignments but not necessarily with the R -symmetry in Table 2.1 are

$$\begin{aligned}
\mathcal{L}_{\text{soft}} = & -\frac{1}{2}M_1\tilde{B}\tilde{B} - \frac{1}{2}M_2\tilde{W}\tilde{W} - \frac{1}{2}M_3\tilde{g}\tilde{g} + \text{h.c.} \\
& - A_h x h_u h_d - B_u h_u r_u - B_d h_d r_d - T x + \text{h.c.} \\
& - \tilde{m}_{H_u}^2 |h_u|^2 - \tilde{m}_{H_d}^2 |h_d|^2 - \tilde{m}_{R_u}^2 |r_u|^2 - \tilde{m}_{R_d}^2 |r_d|^2 - \tilde{m}_X^2 |x|^2 \\
& + \mathcal{L}_{\text{soft}}^{\text{Matter}},
\end{aligned} \tag{2.11}$$

where $\mathcal{L}_{\text{soft}}^{\text{Matter}}$ stands for SSM matter field soft terms. For simplicity we have elided soft terms that do not have any counterpart in the superpotential Eq. (2.1) and off-diagonal scalar soft masses.² If the mediation respects an R -symmetry, then only the soft masses \tilde{m}^2 are generated.³

In the presence of SSM soft terms, the $H_{u,d}$ multiplet can now obtain non-zero F -components, deforming the visible sector goldstino away from χ_{vis} :

$$\chi'_{\text{vis}} \sim \chi_{\text{vis}} + \langle F_{H_u} \rangle \tilde{h}_u^0 + \langle F_{H_d} \rangle \tilde{h}_d^0. \tag{2.12}$$

²Such terms do not arise if SUSY breaking is mediated to the visible sector solely through a superfield of R -charge 2, where the R -symmetry is spontaneously broken by its vev. This is indeed the case, for instance, in gauge mediation and anomaly mediation. More generally, although additional soft terms like $B_r r_u r_d$ or $B_h h_u h_d$ do modify the vacuum structure, the mass of the goldstino is not substantially modified, as explained by the persistent zero mode argument in Sec. 2.1.4.

³Majorana masses for the gauginos violate the R -symmetry, necessitating new field content to achieve Dirac gaugino masses. We will discuss this in more detail in Sec. 2.2.3.

However, since the soft terms affect the vacuum structure, there is no guarantee that χ'_{vis} will even be a mass eigenstate,⁴ but we will see that there is still a light fermion in the spectrum.

2.1.4 A GeV-scale Pseudo-Goldstino?

There are two facts which conspire to ensure a light fermion in the visible sector spectrum. This state is generically different from Eq. (2.12), so we will refer to it as a pseudo-goldstino and denote it by ζ .

- **Persistent Zero Mode in Wess-Zumino Models:** In the absence of gauge interactions, the visible sector superpotential in Eq. (2.1) is an example of a (renormalizable) Wess-Zumino model. With a minimal Kähler potential, the fermionic mass matrix is

$$\mathcal{M}_{ab}(\phi) = \frac{\partial^2 W}{\partial \phi_a \partial \phi_b}, \quad (2.13)$$

and because Eq. (2.1) spontaneously breaks SUSY, $\det \mathcal{M}_{ab}(\langle \phi \rangle) = 0$ in the vacuum. Moreover, for Wess-Zumino models that spontaneously break SUSY, $\det \mathcal{M}_{ab}(\phi) = 0$ for *arbitrary* scalar field configurations.⁵

Now consider adding SSM soft masses. At tree-level and in the absence of gauge interactions, the only effect of adding Eq. (2.11) is to change the vacuum configuration of the visible sector fields. However, since $\det \mathcal{M}_{ab}(\phi) = 0$ for all field configurations, there is guaranteed to be a massless fermion at tree-level. Thus, the pseudo-goldstino can only get a tree-level mass through gauge interactions, namely through mixing with the gauginos. We will see that this mixing angle is quite small, thus the leading pseudo-goldstino mass is loop suppressed.

⁴In addition, the messenger sector generically introduces new fermionic mass terms that mix the hidden sector and visible sector goldstinos. In the $\langle F_{\text{vis}} \rangle \ll \langle F_{\text{hid}} \rangle$ limit, we can safely ignore such effects.

⁵This result is reasonably well-known in the literature, though much of it unpublished. See Ref. [158] for a straightforward argument using the Witten index [164].

- **R Symmetry:** As discussed in Sec. 2.1.1, the visible sector R -symmetry implies three massless fermions. Thus, the pseudo-goldstino mass is proportional to the degree of R -violation. If the mediation preserves an R -symmetry, then at minimum, the pseudo-goldstino will get a mass from SUGRA effects proportional to $m_{3/2}$. In the usual case that R -symmetry is broken by SSM soft masses, the pseudo-goldstino mass will depend on the R -violating gaugino masses, A -terms, B -terms, and x tadpole. As already mentioned, the tree-level effect is small because it is proportional to the small goldstino/gaugino mixing angle. The R -violating scalar soft terms contribute to the pseudo-goldstino mass only at loop level.⁶

To illustrate these points, consider a hidden sector field S with R -charge 2 and the visible sector field X also of R -charge 2. In the $\langle F_{\text{vis}} \rangle \ll \langle F_{\text{hid}} \rangle$ limit, we can apply the arguments above to understand the mass of the visible sector fermion in X . Integrating out the messenger sector at loop level leads to non-minimal Kähler couplings between the hidden and visible sectors. The Kähler operator

$$\frac{c_1}{\Lambda}(S + S^\dagger)(X^\dagger X) \tag{2.14}$$

is an example of an R -violating operator which contributes to SSM soft terms. However, this term does not contain a fermion mass for X so it does not evade the first point.⁷ The R -symmetric Kähler operator

$$\frac{c_2}{\Lambda^2}(X^\dagger X)^2 \tag{2.15}$$

does contain a fermion mass for X proportional to $\langle x \rangle$, but it cannot induce a mass unless the R -symmetry is broken by another operator to give a non-zero value of $\langle x \rangle$. Therefore, only when both types of operators are present can a pseudo-goldstino mass be generated.

⁶In addition, the R -violating scalar soft terms themselves are often suppressed (notably in gauge mediation), leading to an additional suppression of the pseudo-goldstino mass.

⁷This operator appears to induce a Dirac mass between the fermion in S and the fermion in X , but this mass must vanish in the vacuum to have a massless true goldstino.

To summarize, even after coupling the visible sector to a hidden source of SUSY breaking, a light pseudo-goldstino persists as a remnant of the original visible SUSY breaking dynamics. Its tree-level mass is suppressed because it is only induced by small mixings with the gauginos. At one loop, its mass is protected by the R -symmetry. These two effects imply that the pseudo-goldstino mass is typically a loop factor below the scale of R -violation in the SSM soft parameters, putting it in the (cosmologically dangerous) mass range $\mathcal{O}(10 \text{ MeV} - 1 \text{ GeV})$. For R -symmetric mediation, the mass is suppressed and proportional to $m_{3/2}$ (and cosmologically safe for $m_{3/2} \ll 1 \text{ keV}$). Since the above arguments are based mainly on R -symmetry and SUSY, one expects them to hold on quite general grounds independent of the details of the visible SUSY breaking dynamics.

The cosmological bounds in Sec. 2.3 on the R -violating scenario would be weakened if the pseudo-goldstino could be made heavier than a few GeV. In principle, and at the price of tuning electroweak symmetry breaking, the loop-induced mass could be raised above naive estimates by increasing the size of the R -violating soft parameters, though arbitrarily large soft terms will spoil electroweak symmetry breaking. We could try to increase the size of R violation by considering visible sector SUSY breaking which spontaneously breaks R [120], but by the Wess-Zumino zero mode argument, this R violation would feed into the pseudo-goldstino mass only at loop level. Finally, we note that the mass of the light fermion can be raised with an operator $\mathcal{W} \supset mX^2$. Of course, with such an operator, SUSY is no longer broken in the visible sector, and there is no sense in which the light fermionic state can be referred to as a pseudo-goldstino.

2.2 Properties of the Pseudo-Goldstino

As discussed in the previous section, the properties of the pseudo-goldstino are strongly influenced by the SUSY breaking mediation mechanism. In the case of R -violating mediation, there are significant one-loop corrections to pseudo-goldstino mass. Conversely, if the mediation is R -symmetric, the mass of the pseudo-goldstino

is proportional to $m_{3/2}$ but typically lighter than the gravitino. We begin by calculating the mass and width of the pseudo-goldstino in the presence of R -violation, and then study the R -symmetric case.

2.2.1 Mass with R Violation

For arbitrary vevs of the neutral scalars, the tree-level neutralino mass matrix in the basis

$$\psi = \left(\tilde{x}, \tilde{h}_u^0, \tilde{h}_d^0, \tilde{r}_u^0, \tilde{r}_d^0, \tilde{B}, \tilde{W}_3 \right) \quad (2.16)$$

is

$$\mathcal{M} = \begin{pmatrix} 0 & \lambda \langle h_d^0 \rangle & \lambda \langle h_u^0 \rangle & 0 & 0 & 0 & 0 \\ \lambda \langle h_d^0 \rangle & 0 & \lambda \langle x \rangle & \mu_u & 0 & \frac{g' \langle h_u^0 \rangle}{\sqrt{2}} & -\frac{g \langle h_u^0 \rangle}{\sqrt{2}} \\ \lambda \langle h_u^0 \rangle & \lambda \langle x \rangle & 0 & 0 & \mu_d & -\frac{g' \langle h_d^0 \rangle}{\sqrt{2}} & \frac{g \langle h_d^0 \rangle}{\sqrt{2}} \\ 0 & \mu_u & 0 & 0 & 0 & -\frac{g' \langle r_u^0 \rangle}{\sqrt{2}} & \frac{g \langle r_u^0 \rangle}{\sqrt{2}} \\ 0 & 0 & \mu_d & 0 & 0 & \frac{g' \langle r_d^0 \rangle}{\sqrt{2}} & -\frac{g \langle r_d^0 \rangle}{\sqrt{2}} \\ 0 & \frac{g' \langle h_u^0 \rangle}{\sqrt{2}} & -\frac{g' \langle h_d^0 \rangle}{\sqrt{2}} & -\frac{g' \langle r_u^0 \rangle}{\sqrt{2}} & \frac{g' \langle r_d^0 \rangle}{\sqrt{2}} & M_1 & 0 \\ 0 & -\frac{g \langle h_u^0 \rangle}{\sqrt{2}} & \frac{g \langle h_d^0 \rangle}{\sqrt{2}} & \frac{g \langle r_u^0 \rangle}{\sqrt{2}} & -\frac{g \langle r_d^0 \rangle}{\sqrt{2}} & 0 & M_2 \end{pmatrix}. \quad (2.17)$$

As argued in Sec. 2.1.4, the tree-level pseudo-goldstino mass is induced only by mixing with the gauginos. Expanding in the gauge couplings, the first-order (unnormalized) mass eigenstate is

$$\zeta : \left(1, 0, 0, -\frac{\lambda \langle h_d^0 \rangle}{\mu_u}, -\frac{\lambda \langle h_u^0 \rangle}{\mu_d}, -\frac{g'}{\sqrt{2}} \frac{\lambda \langle r' \rangle}{M_1}, \frac{g}{\sqrt{2}} \frac{\lambda \langle r' \rangle}{M_2} \right) + \mathcal{O}(g^2), \quad (2.18)$$

where we have defined the R -charge 2 combination

$$r' \equiv \frac{h_u^0}{\mu_d} r_d^0 - \frac{h_d^0}{\mu_u} r_u^0. \quad (2.19)$$

The tree-level mass of the pseudo-goldstino is

$$m_\zeta^{\text{tree}} = \frac{\lambda^2}{2} \langle r' \rangle^2 \left(\frac{g'^2}{M_1} + \frac{g^2}{M_2} \right) + \mathcal{O}(g^2). \quad (2.20)$$

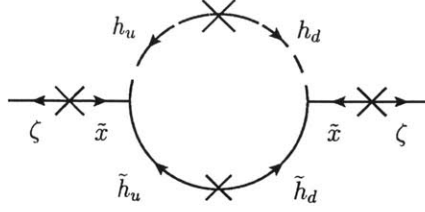


Figure 2-1: Estimate of the loop correction to the pseudo-goldstino mass. Fermion and scalar insertions come from the superpotential Eq. (2.1) and from the A_h term in Eq. (2.11). The fermion insertion is $\lambda\langle x \rangle$ and the scalar insertion is $2\lambda\kappa - A_h\langle x \rangle - \lambda^2\langle h_u^0 \rangle\langle h_d^0 \rangle$. The full set of diagrams appear in Fig. A-1.

After solving for the vacuum configuration, we find that for typical weak-scale values for the soft masses and superpotential parameters ($\mathcal{O}(100 \text{ GeV})$), the pseudo-goldstino mass is $m_\zeta^{\text{tree}} \simeq \mathcal{O}(1 - 10 \text{ MeV})$. In particular, as long as all of the Higgs sector soft parameters have a similar scale, then there is a cancellation in Eq. (2.19) which yields a small value of $\langle r' \rangle$, and thus a small pseudo-goldstino mass.⁸

Given the small tree-level effect, we need to take into account loop corrections. At this order, the contribution from gauginos is small, and the pseudo-goldstino can be treated as a linear combination of \tilde{x} , \tilde{r}_u^0 , and \tilde{r}_d^0 . Throughout this chapter, we will use the notation

$$\Theta_{g,m} \tag{2.21}$$

to denote the mixing angle between the gauge eigenstate g and the mass eigenstate m . The diagram shown in Fig. 2-1 gives a naive estimate for the one loop correction:

$$\delta m_\zeta^{\text{loop}} \approx \frac{2\lambda^2\Theta_{\tilde{x},\zeta}^2}{16\pi^2} \frac{\lambda\langle x \rangle (2\lambda\kappa - A_h\langle x \rangle - \lambda^2\langle h_u^0 \rangle\langle h_d^0 \rangle)}{m_{\text{eff}}^2}. \tag{2.22}$$

Here, $\lambda^2/(16\pi^2)$ is a loop factor and the 2 accounts for both neutral and charged particles in the loop. The fermion mass insertion $\lambda\langle x \rangle$ and the scalar mass insertion $2\lambda\kappa - A_h\langle x \rangle - \lambda^2\langle h_u^0 \rangle\langle h_d^0 \rangle$ come from Eq. (2.1) and Eq. (2.11), and m_{eff} is the

⁸It is possible to increase the tree-level pseudo-goldstino mass to $\mathcal{O}(1 \text{ GeV})$ by imposing a large up/down hierarchy on the Higgs sector soft parameters. That said, this larger mass is still constrained by the cosmological bounds in Sec. 2.3.

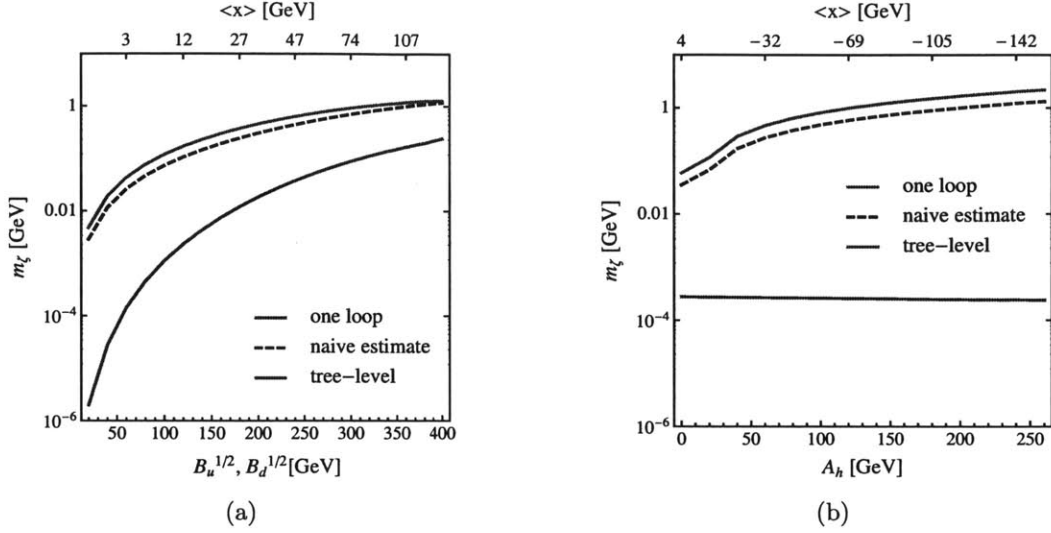


Figure 2-2: Left: mass of the pseudo-goldstino as a function of $B_u^{1/2} = B_d^{1/2}$. For concreteness, we fix $\tilde{m}_{H_u}^2 = \tilde{m}_{H_d}^2 = \tilde{m}_{R_u}^2 = \tilde{m}_{R_d}^2 = (600 \text{ GeV})^2$, $\mu_u = 200 \text{ GeV}$, $\mu_d = 300 \text{ GeV}$, $M_1 = 100 \text{ GeV}$, $M_2 = 150 \text{ GeV}$, and $\lambda = 1$. The value of κ is chosen to obtain the correct value of m_Z , and all other soft parameters are set to zero. The red line indicates the mass including one loop corrections and the dashed line is the naive estimate according to Eq. (2.22) with $m_{\text{eff}}^2 = \tilde{m}_{H_u}^2 + \tilde{m}_{H_d}^2 + \mu_u^2 + \mu_d^2$. For comparison, the green line shows the small tree-level contribution. The value of $\langle x \rangle$ is shown as a reference, since this vev controls the mass according to Eq. (2.22). For R -breaking soft terms around the weak scale, the mass falls in the range $\mathcal{O}(10 \text{ MeV} - 1 \text{ GeV})$. Right: mass of the pseudo-goldstino as a function of A_h with $B_u = B_d = (70 \text{ GeV})^2$ and all other soft parameters as in the left figure.

characteristic mass scale for the particles in the loop.

A full calculation of the one-loop pseudo-goldstino mass appears in App. A, but we can estimate the size of the effect from Eq. (2.22). If we take $\kappa \gg \langle h_u^0 \rangle \langle h_d^0 \rangle$, $A_h \langle x \rangle$ we find

$$\begin{aligned}
 \delta m_\zeta^{\text{loop}} &\approx \frac{\lambda^4 \Theta_{\bar{x}, \zeta}^2 \langle x \rangle \kappa}{4\pi^2 m_{\text{eff}}^2} \\
 &\approx 100 \text{ MeV} \left(\frac{\lambda}{1.0} \right)^4 \left(\frac{\Theta_{\bar{x}, \zeta}}{0.7} \right)^2 \left(\frac{\langle x \rangle}{35 \text{ GeV}} \right) \left(\frac{\kappa}{(100 \text{ GeV})^2} \right) \left(\frac{300 \text{ GeV}}{m_{\text{eff}}} \right)^2,
 \end{aligned} \tag{2.23}$$

where we have indicated typical values for the parameters.⁹ This loop correction

⁹One might be tempted to lift this mass by raising κ , however this implies large fine tuning for electroweak symmetry breaking.

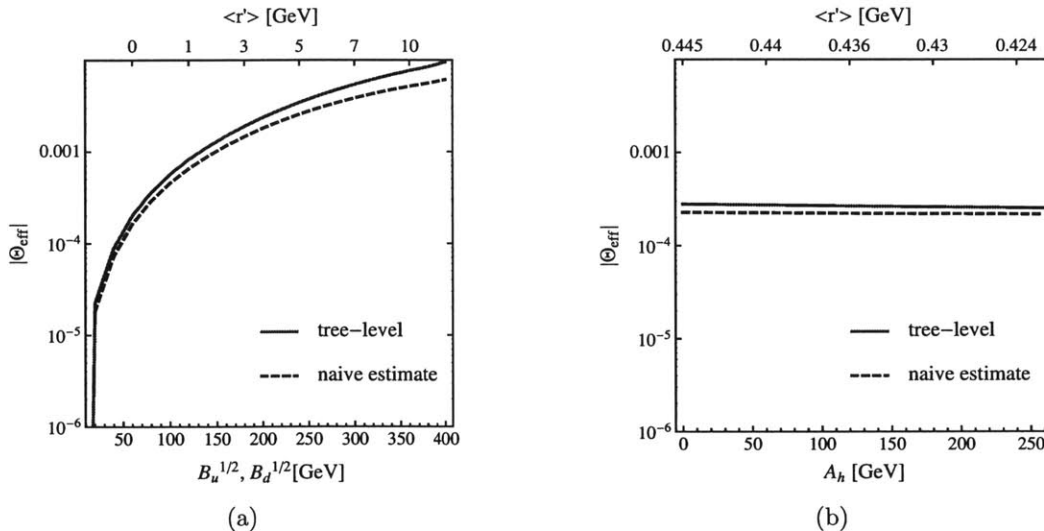


Figure 2-3: Effective mixing angle of the pseudo-goldstino with gauginos as defined in Eq. (2.27). The left and right plots use the same parameters as Figs. 2-2a and 2-2b, respectively. The blue line represents the exact tree-level result and the dashed line shows the naive estimate according to Eq. (2.18). As a reference, the value of $\langle r' \rangle$ is shown, since this controls the mixing angle in Eq. (2.18). Notice that in right plot, $\langle r' \rangle$ is small compared to the left plot and almost constant. According to Eq. (2.18), this leads to a smaller and almost constant mixing angle (and tree-level mass).

almost always dominates over the tree-level mass. Fig. 2-2 compares the the full one-loop calculation to the estimate in Eq. (2.22).

2.2.2 Width with R Violation

In the presence of R -violating soft masses, the pseudo-goldstino mixes with the bino and neutral wino states. From Eq. (2.18), we see that this mixing is suppressed, both by gauge couplings and by the small size of the R -violating parameter $\langle r' \rangle$. The typical mixing angle can be read off from Eq. (2.18) by normalizing the state. The full expression is not insightful, however for weak-scale soft parameters we generally obtain

$$\Theta_{\tilde{B},\zeta} \sim \Theta_{\tilde{W},\zeta} \sim \mathcal{O}(10^{-2} - 10^{-4}), \quad (2.24)$$

where the range is set by the size of $\langle r' \rangle$ as illustrated in Fig. 2-3.

This small mixing with the gauginos induces a coupling of the pseudo-goldstino

to the gravitino and photon, permitting the decay $\zeta \rightarrow \gamma + \tilde{G}$ as shown in Fig. 2-4. Since no other final states are kinematically allowed, this is the dominant decay mode of the pseudo-goldstino.

We can calculate the pseudo-goldstino width using the goldstino equivalence theorem. The longitudinal gravitino \tilde{G}_L (approximated by the true goldstino in Eq. (2.7)), couples derivatively to the supercurrent:

$$\mathcal{L} = \frac{1}{F}(\partial_\mu \tilde{G}_L)j^\mu + \text{h.c.} \quad (2.25)$$

The supercurrent contains the coupling of the pseudo-goldstino ζ to the photon

$$j^\mu \supset -\frac{\Theta_{\text{eff}}}{2\sqrt{2}}(\sigma^\nu \bar{\sigma}^\rho \sigma^\mu \zeta^\dagger)F_{\nu\rho}, \quad (2.26)$$

where the effective ‘‘photino’’ mixing angle is determined by the weak mixing angle θ_w ,

$$\Theta_{\text{eff}} = \cos \theta_w \Theta_{\tilde{B},\zeta} + \sin \theta_w \Theta_{\tilde{W},\zeta}. \quad (2.27)$$

Using various equations of motion, the interaction term Eq. (2.25) contains

$$\mathcal{L} \supset \frac{\Theta_{\text{eff}}}{\sqrt{2}F}m_\zeta^2(\tilde{G}_L\sigma^\mu\zeta^\dagger)A_\mu + \text{h.c.} \quad (2.28)$$

where m_ζ is the physical mass of the pseudo-goldstino. The width of the pseudo-goldstino is thus¹⁰

$$\Gamma(\zeta \rightarrow \gamma + \tilde{G}_L) = \frac{|\Theta_{\text{eff}}|^2}{16\pi F^2}m_\zeta^5. \quad (2.29)$$

¹⁰Instead of using a derivatively coupled basis for the true goldstino, one could use a non-derivative basis where the goldstino coupling is proportional to the gaugino soft mass M . One might worry that in the non-derivative basis, the decay width would scale as $m_\zeta^3 M^2/F^2$ instead of scaling as m_ζ^5/F^2 . However, one can show that a cancellation occurs when proper mixing angles are taken into account, namely $\cos \theta_w \Theta_{\tilde{B},\zeta} M_1 + \sin \theta_w \Theta_{\tilde{W},\zeta} M_2 \equiv m_\zeta \Theta_{\text{eff}}$, and the two bases give consistent results.

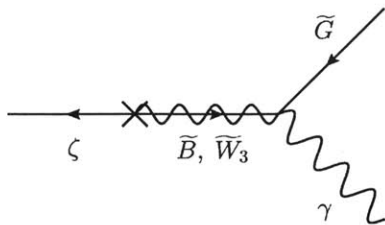


Figure 2-4: Dominant decay mode for the pseudo-goldstino in the R -violating case. This decay occurs through the (small) mixing angle between the pseudo-goldstino and the neutral gauginos.

The lifetime of the pseudo-goldstino is

$$\tau \equiv \frac{1}{\Gamma_\zeta} \simeq 10^9 \text{ sec} \left(\frac{10^{-3}}{\Theta_{\text{eff}}} \right)^2 \left(\frac{F}{10^{10} \text{ GeV}^2} \right)^2 \left(\frac{100 \text{ MeV}}{m_\zeta} \right)^5, \quad (2.30)$$

which is generically a cosmological problem, as discussed further in Sec. 2.3.

2.2.3 The R -symmetric Case

Because of the cosmological difficulties in the R -violating case, it is worthwhile to consider the possibility that the visible sector R -symmetry is not violated by SUSY breaking mediation from the hidden sector. In this case, only the soft masses \tilde{m}^2 in Eq. (2.11) are relevant. As in the minimal R -symmetric SSM [122], we can generate Dirac gaugino masses by introducing chiral superfields Φ_i in the adjoint representation of the SM gauge groups [97]:

$$\int d^2\theta \frac{\theta_\alpha D'}{\Lambda} W_i^\alpha \Phi_i, \quad (2.31)$$

where $\theta_\alpha D'$ is a D -type spurion with R -charge 1, and the index i runs over the SM gauge groups. The fermionic components of Φ_i marry the SSM gauginos with a Dirac mass term proportional to D'/Λ .¹¹

As touched on in Sec. 2.1.2, an exact R -symmetry in the visible sector implies an

¹¹A similar mechanism could generate a Dirac mass for the pseudo-goldstino, a possibility we will not pursue.

exactly massless state, which in the sequestered limit corresponds to the goldstino of the visible sector. Of course, there is an irreducible contribution to R -violation from SUGRA, since canceling the cosmological constant by hand explicitly violates any R -symmetry. In Ref. [58], it was argued that if two sequestered sectors independently break SUSY and couple solely through SUGRA, then one linear combination of the goldstini is eaten by the gravitino, while the orthogonal combination obtains a mass $2m_{3/2}$. However, in the present case, the SUSY breaking sectors are not even approximately sequestered, since the hidden sector is necessary to achieve weak-scale superpartners and evade the supertrace sum rule.

It is straightforward to calculate the SUGRA contribution to the pseudo-goldstino mass (for example, using the methods introduced in Ref. [55, 56]), but a toy model is sufficient to understand the parametric scaling. Consider a visible sector Lagrangian with a single chiral multiplet X

$$\mathcal{K} = X^\dagger X - \frac{1}{2\Lambda^2} (X^\dagger X)^2, \quad \mathcal{W} = \mu_x X. \quad (2.32)$$

In the absence of SUGRA, the higher-dimensional Kähler term stabilizes the goldstino x at 0 with a mass

$$(m_x^{\text{vis}})^2 = \frac{\mu_x^2}{\Lambda^2}, \quad (2.33)$$

where the “vis” superscript indicates that this is the contribution from the visible sector alone. For small field vevs, the Kähler term also implies a mass term for the pseudo-goldstino¹²

$$m_\zeta = -2 \frac{\mu_x \langle x \rangle^\dagger}{\Lambda^2}. \quad (2.34)$$

where the factor of 2 is a Majorana symmetry factor. The leading SUGRA effect is

¹²For larger field vevs, we would have to account for the change in kinetic normalization of the X multiplet. We are implicitly assuming $\langle x \rangle \ll \Lambda$.

to generate a tadpole term for x proportional to $m_{3/2}$,¹³

$$\mathcal{L} = 2m_{3/2}\mu_x x + \text{h.c.} \quad (2.35)$$

The x scalar is then stabilized away from zero due to this tadpole, giving rise to a pseudo-goldstino mass in agreement with Ref. [58],

$$\text{Visible Sector Only : } \langle x \rangle = -\frac{\mu_x}{(m_x^{\text{vis}})^2} m_{3/2} = -\frac{\Lambda^2}{\mu_x} m_{3/2}, \quad m_\zeta = 2m_{3/2}. \quad (2.36)$$

If SUSY breaking is mediated from the hidden sector, this will generate an additional soft mass term for x , $(m_x^{\text{hid}})^2 |x|^2$.¹⁴ The new scalar mass is:

$$(m_x^{\text{tot}})^2 = (m_x^{\text{vis}})^2 + (m_x^{\text{hid}})^2. \quad (2.37)$$

Thus, in the presence of the hidden sector, x is stabilized at a different (typically smaller) field value:

$$\text{Visible \& Hidden Sectors : } \langle x \rangle = -\frac{\mu_x}{(m_x^{\text{tot}})^2} m_{3/2}, \quad m_\zeta = 2\frac{(m_x^{\text{vis}})^2}{(m_x^{\text{tot}})^2} m_{3/2}. \quad (2.38)$$

The degree to which the soft mass from the hidden sector dominates the visible sector Kähler mass is the degree to which the pseudo-goldstino is lighter than $2m_{3/2}$. This feature of the toy model is shared by the model in Sec. 2.1 albeit with complications coming from the fact the pseudo-goldstino is a linear combination of the visible sector fermions and the sgoldstino is generically not a mass eigenstate. Numerically, the pseudo-goldstino ends up being a few orders of magnitude lighter than the gravitino.

¹³In the conformal compensator formalism, these terms arise from $\mathcal{W} \rightarrow \Phi^2(\mu_x X)$ where $\Phi \simeq 1 + \theta^2 m_{3/2}$. For large field vevs, there are additional contributions to the mass from the Kähler potential discussed in Ref. [69] and detailed in Ref. [56].

¹⁴We are considering the limit $\langle F_{\text{vis}} \rangle \ll \langle F_{\text{hid}} \rangle$ so we can ignore modifications to the fermion mass matrix from the hidden sector goldstino.

2.3 Cosmological Constraints

It is well known that long-lived particles with masses above 1 keV can be cosmologically dangerous if they are produced in the early universe; this is the usual gravitino problem [137]. This implies significant cosmological constraints on the pseudo-goldstino in the R -violating case, since it has a mass in the range $\mathcal{O}(10 \text{ MeV} - 1 \text{ GeV})$ and a lifetime that is typically longer than a second. In contrast, R -symmetric mediation yields a pseudo-goldstino lighter than the gravitino, which can be as light as a few eV. We discuss the cosmological implications of each scenario in turn.

In the R -violating case, stringent bounds apply to the pseudo-goldstino because it is generically a long-lived hot relic. From Eq. (2.30), the pseudo-goldstino has a lifetime which is typically much longer than the time at which Big Bang Nucleosynthesis (BBN) begins ($t_{\text{BBN}} \approx 1 \text{ sec}$). In principle, a long lifetime is not constrained as long as the energy density stored in the pseudo-goldstino is much smaller than the radiation energy density at the time of BBN. However, this is not the case, as shown in App. B. The pseudo-goldstino has couplings which are strong enough to allow it to be in thermal equilibrium with the SSM when the temperature of the universe is above the weak scale. But the couplings of the pseudo-goldstino are sufficiently small that the pseudo-goldstino freezes out while it is still relativistic, leading to a large number density $n_\zeta \propto T^3$ and a correspondingly large energy density $\rho_\zeta \propto m_\zeta T^3$ which is grossly at odds with BBN for masses in the range $\mathcal{O}(10 \text{ MeV} - 1 \text{ GeV})$.

The only way to avoid these BBN constraints is for the pseudo-goldstino to decay more quickly.¹⁵ In fact, for sufficiently low hidden sector breaking and large enough R -violation (in the form of $\langle x \rangle$ and $\langle r' \rangle$) the lifetime can be short enough to decay before BBN. With a maximally favorable spectrum with the lowest scale of SUSY breaking, we can achieve

$$\tau_\zeta \approx 5 \times 10^{-3} \text{ sec} \left(\frac{7 \times 10^{-3}}{\Theta_{\text{eff}}} \right)^2 \left(\frac{F}{10^8 \text{ GeV}^2} \right)^2 \left(\frac{1 \text{ GeV}}{m_\zeta} \right)^5, \quad (2.39)$$

¹⁵Alternatively, one could try to arrange additional annihilation channels for the pseudo-goldstino such that it becomes a cold relic.

which is cosmological safe (though perhaps unrealistically optimistic). Note that the decay rate scales as the fifth power of the mass, but the arguments in Sec. 2.1.4 preclude a pseudo-goldstino heavier than a few GeV. Alternatively, it is possible that the universe did not reheat up to the weak scale, in which case our cosmological considerations are not applicable.

A more favorable cosmology occurs if the mediation is R -symmetric. As discussed in Sec. 2.2.3, the pseudo-goldstino is then much lighter than the gravitino. For light gravitino masses that evade cosmological constraints ($m_{3/2} \lesssim 1$ keV), the pseudo-goldstino is also cosmologically safe.¹⁶ This is because the pseudo-goldstino never carries an appreciable fraction of the total energy density of the universe, and its contribution at late times is further diluted by the QCD phase transition.

2.4 Collider Phenomenology

With visible sector SUSY breaking, there can be dramatic effects on collider phenomenology from the presence of new light states below the weak scale. We have seen that there is always a light pseudo-goldstino in the spectrum. As we will explain in more detail in Sec. 2.4.1, there is also typically a light complex scalar which is related to the sgoldstino and denoted by ϕ .

These light pseudo-(s)goldstino states affect the decay widths of SSM particles. As is evident from the superpotential in Eq. (2.1), the only couplings of the pseudo-(s)goldstino to the SSM are through the Higgs sector and the gauge sector. Therefore, the presence of these light states generically alters the decay width of the Higgs boson and the lightest neutralino (since it is a linear combination of fields originating in the Higgs and gauge sectors).

A detailed discussion of modified Higgs decays appears in Sec. 2.4.2. We will find that Higgs decays are potentially modified by pseudo-sgoldstino channel, if kinemati-

¹⁶In the case that the gravitino is much heavier ($\mathcal{O}(100$ GeV)), the bounds discussed in the R -violating case would apply to the pseudo-goldstino. In particular, R -symmetry is no longer a good symmetry since the pseudo-goldstino feels substantial R -violation from anomaly mediation [144, 102], pushing its mass above 1 keV.

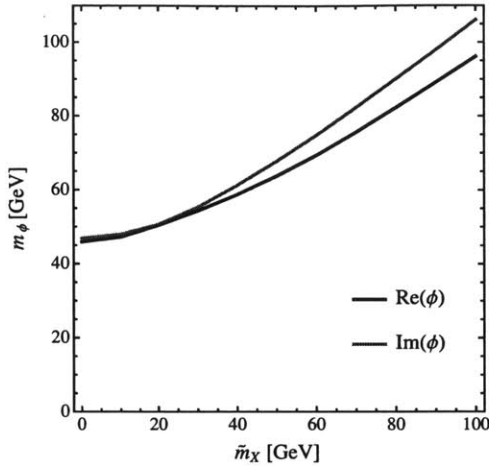


Figure 2-5: An illustration of the pseudo-goldstino mass as a function of the soft mass \tilde{m}_X . We fix $\tilde{m}_{H_u}^2 = \tilde{m}_{H_d}^2 = \tilde{m}_{R_u}^2 = \tilde{m}_{R_d}^2 = (140 \text{ GeV})^2$, $\mu_u = 300 \text{ GeV}$, $\mu_d = 500 \text{ GeV}$, $B_u = B_d = (100 \text{ GeV})^2$, $\lambda = 1$, κ is fixed by m_Z , and all other soft parameters are set to zero. Shown are the masses of both the scalar and pseudo-scalar components of ϕ , which split as \tilde{m}_X increases. Since X is a singlet, \tilde{m}_X is expected to be small in many mediation schemes. In the R -symmetric case (i.e. $B_u = B_d = 0$), the behavior is qualitatively similar except $\text{Re } \phi$ and $\text{Im } \phi$ are degenerate.

cally allowed. In Sec. 2.4.3, we discuss the lightest observable-sector supersymmetric particle (LOSP), focusing on the case of a neutralino LOSP. In contrast to typical light-gravitino phenomenology, a neutralino LOSP dominantly decays to the pseudo-goldstino rather than the gravitino, and typically in association with a Z .

2.4.1 The Pseudo-Sgoldstino

Spontaneous SUSY breaking in a Wess-Zumino model leads to a goldstino, namely, a complex scalar that is massless at tree-level and which is the superpartner of the goldstino. Its mass is in general lifted by loops within the sector that breaks SUSY. Thus, if the hidden and visible sectors were completely sequestered, we would expect a light complex scalar that corresponds to the pseudo-goldstino direction.

In the presence of soft masses generated from hidden sector mediation, the pseudo-goldstino ϕ can get a weak-scale mass. Here we will focus on the case where X has a relatively small soft mass, as in this case we would have the most dramatic

consequences for collider phenomenology. One motivation for a small X soft mass is that if the gravitino is light, then SUSY breaking mediation is most easily achieved via gauge interactions, and therefore it is reasonable to assume that the soft mass for X is small relative to other SSM soft masses since it is a gauge singlet. With this assumption, the pseudo-sgoldstino is mostly aligned along the X direction and is the lightest scalar in the spectrum. In Fig. 2-5, we show how the mass of ϕ changes as the X soft mass is varied.

A light pseudo-sgoldstino has important consequences for collider phenomenology because it opens new decay modes for the Higgs boson and the LOSP. We discuss this further in the following subsections, currently focusing on the decay modes of the pseudo-sgoldstino itself.

If the soft parameters violate the R -symmetry, typically x , r_u^0 , and r_d^0 get vevs proportional to a linear combination of B_u and B_d . This implies that all of the neutral scalars $(x, h_u^0, h_d^0, r_u^0, r_d^0)$ mix, which in turn gives the light pseudo-sgoldstino decay modes to SM fermions through the SSM Yukawa couplings. The pseudo-sgoldstino is generically more massive than the $b\bar{b}$ threshold and tends to decay through this channel. The width is

$$\Gamma_{\phi \rightarrow b\bar{b}} = \frac{3}{16\pi^2} y_b^2 |\Theta_{h_d^0, \phi}|^2 m_\phi \left(1 - \frac{4m_b^2}{m_\phi^2}\right)^{3/2}, \quad (2.40)$$

where y_b is the bottom Yukawa coupling. This decay is prompt on collider scales for any reasonable value of $\Theta_{h_d^0, \phi}$.

In the case that the mediation is R -symmetric, there is an irreducible contribution to R -violation from SUGRA effects. At tree-level in SUGRA, the soft terms

$$B_u \simeq m_{3/2} \mu_u, \quad B_d \simeq m_{3/2} \mu_d, \quad T \simeq 2m_{3/2} \kappa, \quad (2.41)$$

are generated. After electroweak symmetry breaking, this implies that ϕ will have small mixings with the neutral Higgses and can therefore decay to SM fermions. In particular, the mixing angle $\Theta_{h_d^0, \phi}$ in Eq. (2.40) scales as $\Theta_{h_d^0, \phi} \simeq m_{3/2} \mu_d / (\mu_d^2 + \tilde{m}_{h_d}^2)$,

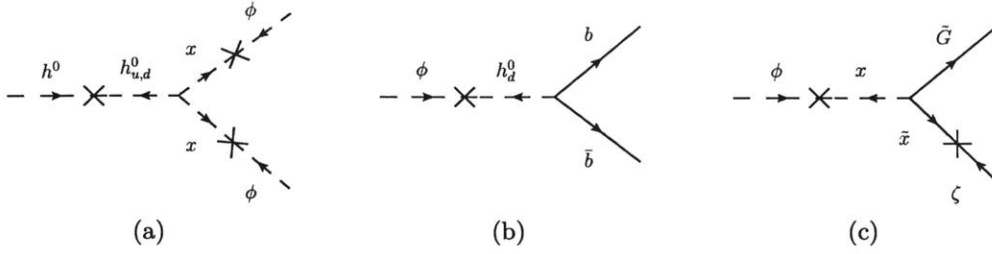


Figure 2-6: Representative diagrams that modify the Higgs width. On the left, we show the dominant decay mode of the Higgs when the pseudo-goldstino is light: $h^0 \rightarrow \phi\phi$. The pseudo-goldstino decays dominantly as $\phi \rightarrow b\bar{b}$ in the R -violating case (middle), while it decays as $\phi \rightarrow \zeta\tilde{G}$ in the R -symmetric case with a sub-keV gravitino (right).

leading to

$$\Gamma_{\phi \rightarrow b\bar{b}} \approx 10^4 \text{ sec}^{-1} \left(\frac{y_b}{0.05} \right)^2 \left(\frac{m_{3/2}}{1 \text{ keV}} \right)^2 \left(\frac{300 \text{ GeV}}{\mu_d} \right)^2 \times \left(\frac{1}{1 + \tilde{m}_{h_d}^2/\mu_d^2} \right) \left(\frac{m_\phi}{50 \text{ GeV}} \right). \quad (2.42)$$

However for the cosmologically preferred region $m_{3/2} \ll \text{keV}$, the R -symmetric decay $\phi \rightarrow \zeta\tilde{G}$ dominates over $\phi \rightarrow b\bar{b}$. The width of this channel is

$$\Gamma_{\phi \rightarrow \zeta\tilde{G}} = \frac{1}{16\pi} |\Theta_{x,\phi} \Theta_{\tilde{x},\zeta}|^2 \frac{m_\phi^5}{F^2} \approx 10^4 \text{ sec}^{-1} \left(\frac{\Theta_{\phi,x} \Theta_{\tilde{x},\zeta}}{1.0} \right)^2 \left(\frac{1 \text{ keV}}{m_{3/2}} \right)^2 \left(\frac{m_\phi}{50 \text{ GeV}} \right)^5, \quad (2.43)$$

where we have neglected mixing with the R_i fields. Since $m_{3/2}$ is expected to be lighter than 1 keV to avoid the cosmological gravitino problem, we expect ϕ to have an invisible decay in the R -symmetric case.

2.4.2 Modified Higgs Decays

One interesting prediction of visible SUSY breaking is that the Higgs boson will cascade decay through two pseudo-goldstinos if it is kinematically allowed. This statement is independent of the mediation mechanism because the interaction between

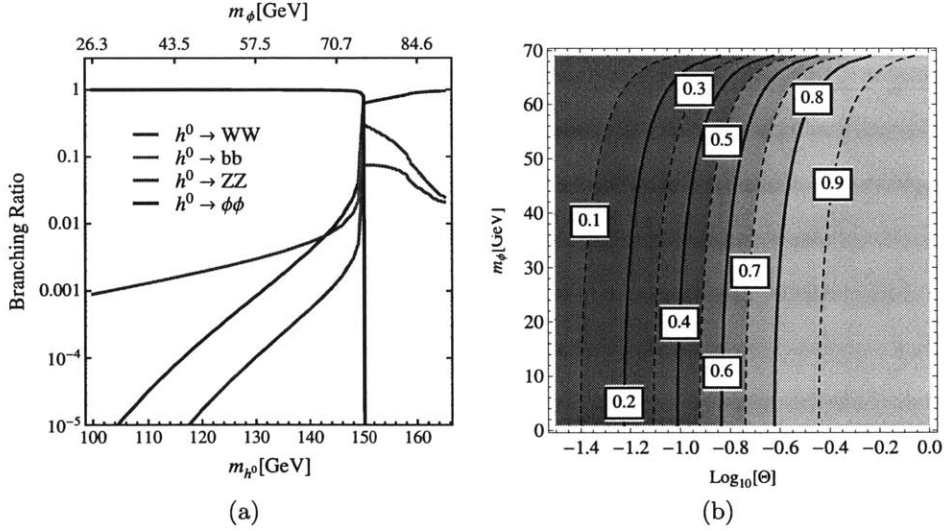


Figure 2-7: Left: the Higgs branching ratios as a function of its mass in the R -symmetric case. We fix $\tilde{m}_{H_u}^2 = \tilde{m}_{H_d}^2 = (140 \text{ GeV})^2$, $\tilde{m}_{R_u}^2 = \tilde{m}_{R_d}^2 = (150 \text{ GeV})^2$, $\mu_u = 150 \text{ GeV}$, $\lambda = 1$, κ is fixed by m_Z , and all other soft parameters are set to zero. We have traded μ_d for m_{h^0} , and the corresponding value of m_{ϕ} is indicated for reference. When kinematically allowed, the decay $h^0 \rightarrow \phi\phi$ is dominant. Right: the branching ratio for $h^0 \rightarrow \phi\phi$ as a function of m_{ϕ} and the mixing angle Θ according to Eq. (2.45). Here, we have fixed $m_{h^0} = 140 \text{ GeV}$, $\lambda = 1$, and assumed SM decay widths to $b\bar{b}$, ZZ^* , and WW^* .

the Higgs boson and the pseudo-goldstino arises from the (R -symmetric) F -term potentials from H_u and H_d . The decay $h^0 \rightarrow \phi\phi$ is reminiscent of certain regions of NMSSM parameter space [48].

The final state of the Higgs cascade decay depends on the amount of R -violation in the visible sector. The decay $h^0 \rightarrow \phi\phi \rightarrow b\bar{b}b\bar{b}$ is expected in the R -violating case, and the invisible final state $h^0 \rightarrow \phi\phi \rightarrow \zeta\tilde{G}\zeta\tilde{G}$ is expected in the R -symmetric case with a light gravitino, as shown in Fig. 2-6.

The interaction leading to a modified Higgs decay is

$$\mathcal{L}_{\text{int}} \supset \lambda^2 |x|^2 (|h_u^0|^2 + |h_d^0|^2), \quad (2.44)$$

which yields a decay width

$$\Gamma(h^0 \rightarrow \phi\phi) = \frac{\lambda^4 |\Theta|^2 v_{\text{EW}}^2}{16\pi m_{h^0}} \left(1 - \frac{4m_{\phi}^2}{m_{h^0}^2}\right)^{1/2}, \quad (2.45)$$

where $v_{\text{EW}} = \sqrt{\langle h_u^0 \rangle^2 + \langle h_d^0 \rangle^2}$ and $\Theta \simeq \Theta_{h_u^0, h^0} \Theta_{x, \phi}^2$. We find that Θ is typically of $\mathcal{O}(0.3)$ or greater. We estimate the width as

$$\Gamma(h^0 \rightarrow \phi\phi) \approx 10^{-1} \text{ GeV} \left(\frac{\lambda}{1.0} \right)^2 \left(\frac{\Theta}{0.3} \right)^2 \left(\frac{125 \text{ GeV}}{m_{h^0}} \right), \quad (2.46)$$

which can easily dominate over SM decay channels. In Fig. 2-7, we illustrate the branching ratios of $h \rightarrow \{\phi\phi, b\bar{b}, WW^{(*)}, ZZ^{(*)}\}$ for a representative sweep of parameter space. As advertised, if $h \rightarrow \phi\phi$ is kinematically allowed, then it dominates the width.¹⁷ We note that the physical Higgs mass can be significantly larger than m_Z because λ contributes to the Higgs quartic coupling. This fact is reflected in Fig. 2-7a.

In addition to the SM-like Higgs, the enlarged Higgs sector can give rise to a rich phenomenology. While a full study is beyond the scope of this work, we wish to highlight some interesting features. In the R -symmetric case, heavier scalars in the Higgs sector are neatly separated between $R_{u,d}$ -like states and $H_{u,d}$ -like states because the mixing is proportional to $m_{3/2}$. Searching for $R_{u,d}$ -like states would help to distinguish our scenario from the NMSSM. While single production of $R_{u,d}$ is heavily suppressed by $\langle r_{u,d}^0 \rangle / v_{\text{EW}} \ll 1$, $R_{u,d}$ can be produced in the decays of heavier states, as well as through electroweak pair production [60]. The neutral $R_{u,d}$ -like scalars typically decay to $h^0\phi$ or $\chi^0\zeta$, where χ^0 is the lightest neutralino.¹⁸ The charged $R_{u,d}$ states typically decay to $\chi^\pm\zeta$ or $W^\pm R^0$, where R^0 is the lightest $R_{u,d}$ -like neutral state, so one expects the $R_{u,d}$ -like decays to be invisible or semi-invisible.

Among the $H_{u,d}$ -like states, the heavy CP-even and CP-odd Higgs-like states H^0 and A^0 dominantly decay to $t\bar{t}$ for the same parameter sweep as Fig. 2-7a. Since the Higgs decays invisibly but the heavy Higgs state is visible, the heavy Higgs could be a ‘‘Higgs impostor’’, although with altered branching ratios with respect to a SM Higgs boson of the same mass [28, 79, 98]. There do exist regions of parameter space where the heavy Higgs-like states are below the $t\bar{t}$ threshold, in which case they dominantly decay to an $R_{u,d}$ -like scalar and h^0 if kinematically allowed, leading to an invisible

¹⁷Depending on the region of parameter space, this can even be true above the WW threshold.

¹⁸Subsequent decays of the χ^0 are discussed in Sec. 2.4.3.

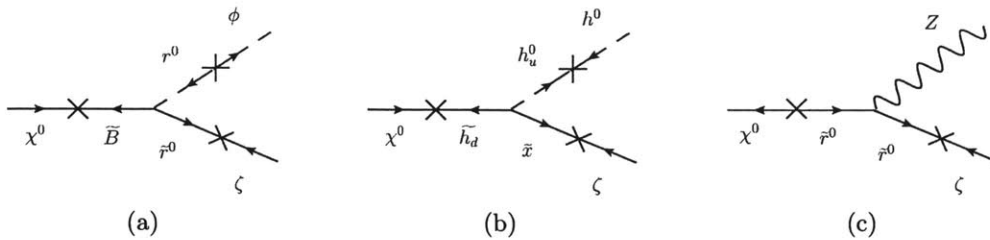


Figure 2-8: Representative diagrams contributing to the decays of a neutralino LO SP: $\chi^0 \rightarrow \phi\zeta$ (left), $\chi^0 \rightarrow h^0\zeta$ (middle), $\chi^0 \rightarrow Z\zeta$ (right). The relative size of the decay widths is sensitive to the scale of R violation, with $\chi^0 \rightarrow \phi\zeta$ becoming suppressed in the R -symmetric limit. The full set of diagrams appear in Fig. C-1.

or semi-invisible decay of the heavy Higgs. The charged $H_{u,d}$ -like states dominantly decay to $t\bar{b}$ or $\bar{t}b$ for the same parameter sweep as Fig. 2-7a.

2.4.3 Modified Neutralino Decays

As in usual SUSY theories, pair- and associated-production of superpartners result in cascade decays that terminate in two LO SPs. This follows from the R -charge assignments in Table 2.1 and the fact that R -parity is conserved regardless of whether the R -symmetry is broken. Thus, it is important to identify the decay modes of the LO SP, since this decay will appear in every cascade decay. For simplicity, we will assume that the LO SP is a neutralino, though other LO SP possibilities can also result in modified phenomenology.

For simplicity, we will ignore decays to gravitinos because are suppressed by the hidden SUSY breaking scale. We will also ignore decays to photons, since they arise only from higher dimensional operators (since the neutralino is neutral).¹⁹ The dominant diagrams contributing to these modes for a neutralino LO SP are shown in Fig. 2-8:

$$\chi^0 \rightarrow \{\phi\zeta, h^0\zeta, Z\zeta\}. \quad (2.47)$$

The presence of these decay modes are independent of the R -symmetry properties

¹⁹The decay $\chi^0 \rightarrow \gamma\zeta$ can occur from mixing between the visible and hidden sector goldstinos, but this is suppressed by $\langle F_{\text{vis}} \rangle / \langle F_{\text{hid}} \rangle$.

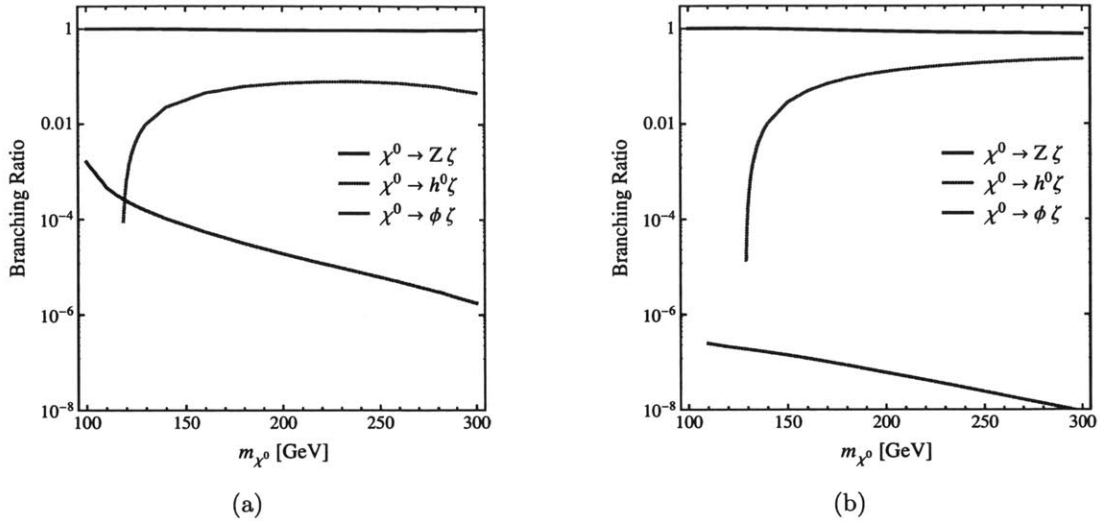


Figure 2-9: Left: branching ratios for a neutralino LOSP as a function of its mass m_{χ^0} in the R -violating case. We fix $\tilde{m}_{h_u}^2 = \tilde{m}_{h_d}^2 = \tilde{m}_{r_u}^2 = \tilde{m}_{r_d}^2 = (140 \text{ GeV})^2$, $\mu_u = 500 \text{ GeV}$, $B_u = B_d = (70 \text{ GeV})^2$, $M_1 = M_2 = 400 \text{ GeV}$, $\lambda = 1$, κ is fixed by m_Z , and all other soft parameters are set to zero. We have traded μ_d for m_{χ} . Right: branching ratios for a neutralino LOSP in the R -symmetric case. We use the same parameters as in the left figure, except we set the Majorana gaugino masses and B -terms equal to zero, and we set the Dirac mass for gauginos $m_D = 1 \text{ TeV}$. The dominant decay mode for the neutralino LOSP is $\chi^0 \rightarrow Z\zeta$ over much of parameter space.

of mediation, however the resulting widths are not. The R -symmetry forbids mixing between the gauginos and the pseudo-goldstino and also forbids mixing between the pseudo-goldstino and h_u^0/h_d^0 . This effect suppresses $\chi^0 \rightarrow \phi\zeta$ in the R -symmetric case.

The explicit formulae for the decay widths are given in App. C. We find that in most of the parameter space, $\chi^0 \rightarrow Z\zeta$ is the dominant channel for either mediation scheme, as illustrated in Fig. 2-9. Moreover, this result is largely independent of the higgsino vs. gaugino fractions of the LOSP. One can understand this by examining Fig. 2-8 and noting that the typical mixing angles in the $\chi^0 \rightarrow Z\zeta$ diagram are $\mathcal{O}(1)$. In contrast, the diagrams contributing to $\chi^0 \rightarrow \phi\zeta$ have at least one suppressed mixing, and the decay to Higgs bosons is phase space suppressed.

Our LOSP decay is similar to a wino-like decay in ordinary gauge mediation,

$\widetilde{W}_3 \rightarrow Z + \widetilde{G}$. However, a distinctive feature is that $Z + \zeta$ dominates even if the mass of the LOSP is comparable to m_Z . In ordinary gauge mediation, such a decay is phase space suppressed and $\widetilde{W}_3 \rightarrow \gamma + \widetilde{G}$ becomes dominant. Therefore, observing this decay without an accompanying $\gamma + \widetilde{G}$ channel could provide evidence for the pseudo-goldstino if the LOSP is not too much heavier than m_Z .²⁰ Similar modified LOSP decays were studied in Ref. [154], and a recent study of neutralino LOSP decays in gauge mediation can be found in Ref. [145].

2.5 Conclusions

The possibility that SUSY could be broken in multiple sectors challenges the standard lore concerning the SSM sparticle spectrum. In particular, the SSM can feel SUSY breaking at tree-level without being constrained by the supertrace sum rule. The immediate consequence of tree-level SUSY breaking in the SSM is the presence of a light pseudo-goldstino state which mixes with SSM gauginos and higgsinos.

In this chapter, we have studied the simplest extension of the SSM that affords tree-level SUSY breaking. We expect that many of the conclusions hold in more generic visible sector SUSY breaking models, since the pseudo-goldstino mass and couplings are largely determined by symmetries. Phenomenologically, the most important symmetry to understand is a $U(1)_R$ symmetry, and we have argued that the properties of the pseudo-goldstino are sensitive to whether the R symmetry is preserved when hidden sector SUSY breaking is mediated to the SSM.

In the usual case of R -violating soft parameters, the pseudo-goldstino mass is typically one loop factor suppressed relative to the weak scale, and the pseudo-goldstino inherits modest couplings to SSM fields through mixing with the gauginos and higgsinos. The cosmological constraints on such a state are severe, since a pseudo-goldstino in thermal equilibrium at early times implies overclosure at late times. In this way, the common assertion that SUSY cannot be broken at tree-level in the SSM still holds,

²⁰An additional distinguishing characteristic is that, depending on the mass of the gravitino, neutralino decays in gauge mediation can be displaced whereas decays to the pseudo-goldstino are prompt.

but the reason is pseudo-goldstino cosmology rather than sum rules. That said, this scenario can be phenomenologically viable if the reheat temperature is $\mathcal{O}(\text{GeV})$ such that the pseudo-goldstino is never in thermal equilibrium. Also, there are small corners of parameter space where the pseudo-goldstino decays before BBN.

Conversely, if the mediation respects the visible sector R -symmetry, then the mass of the pseudo-goldstino is protected. The R -violating effects come only from SUGRA, and the pseudo-goldstino mass is proportional to (but generically smaller than) the gravitino mass. The same region of parameter space that solves the gravitino problem also prevents cosmological overproduction of the pseudo-goldstino.

The distinguishing collider signatures of the simplest visible sector SUSY breaking scenario involve modified Higgs and neutralino decays. Generically, there exists a light pseudo-goldstino ϕ that would dominate the Higgs width through $h^0 \rightarrow \phi\phi$. If the mediation is R -violating, then this state has mixing with h_u and h_d , and the four-body final state $h^0 \rightarrow \phi\phi \rightarrow b\bar{b}b\bar{b}$ is the dominant decay mode. This is similar to the Higgs phenomenology in some regions of the NMSSM. On the other, if the mediation is R -symmetric, then the Higgs boson dominantly decays invisibly to $\zeta\tilde{G}\zeta\tilde{G}$. Since the invisible final state involves the gravitino and the pseudo-goldstino, the Higgs sector becomes an interesting probe of spontaneous SUSY breaking dynamics.

Chapter 3

Constraints on Singlet Extensions of the Higgs Sector

In this chapter we will present an updated version of the analysis in [33] that includes combined 7 and 8 TeV Higgs data. The content is organized as follow: we will briefly review our extended Higgs sector model in Sec. 3.1 and our statistical methods in Sec. 3.2. We will present results in Sec. 3.3. We also consider precision electroweak constraints in Sec. 3.4 and draw conclusions in Sec. 3.5.

3.1 Higgs Friends and Accomplices

We consider a simple set-up in which an extra field, s , mixes with the neutral Higgs through a Higgs portal coupling. In the mass-eigenstate basis the two neutral scalars are \tilde{h} and \tilde{s} , which are related to the interaction eigenstates through

$$\begin{pmatrix} h \\ s \end{pmatrix} = \begin{pmatrix} \cos \theta & -\sin \theta \\ \sin \theta & \cos \theta \end{pmatrix} \cdot \begin{pmatrix} \tilde{h} \\ \tilde{s} \end{pmatrix}. \quad (3.1)$$

This is the Higgs friend scenario. We also consider the Higgs accomplice scenario in which s couples to additional charged particles. At one loop this leads to a coupling

$$\mathcal{L} = \alpha c_{h\gamma\gamma} s F^{\mu\nu} F_{\mu\nu} \quad , \quad (3.2)$$

where $c_{h\gamma\gamma}$ is the usual SM coupling of the Higgs to photons, and α parameterizes deviations from this coupling.¹ Without loss of generality we impose $0 < \theta < \pi/2$. We will refer to the scalar at 125.5 GeV, \tilde{h} , as the Higgs.

All relevant Higgs production cross-sections at the LHC now come suppressed by a factor of $\cos^2 \theta$ and every decay width is suppressed by the same factor, with the exception of decays to photons which are now accompanied by a factor of $(\cos \theta + \alpha \sin \theta)^2$. Since decays to photons are far subdominant then, to a good approximation, all branching ratios remain the same as the SM Higgs, with the exception of the branching ratio to photons which is accompanied by the factor $(1 + \alpha \tan \theta)^2$. Thus for the search channels $h \rightarrow bb, \tau\tau, WW, ZZ$ the total event rate normalized to the event rate for a SM Higgs, otherwise known as the strength modifier, μ , is simply $\mu = \cos^2 \theta$ and for $h \rightarrow \gamma\gamma$ it is $\mu_{\gamma\gamma} = (\cos \theta + \alpha \sin \theta)^2$.

Production of the Higgs friend, \tilde{s} , is suppressed by a factor of $\sin^2 \theta$ compared to SM Higgs production. Whenever $m_{\tilde{s}} < 2m_{\tilde{h}}$, the strength modifier for the friend in the diphoton channel is $(\sin \theta - \alpha \cos \theta)^2$ and is $\sin^2 \theta$ for all other channels.

Whenever $m_{\tilde{s}} > 2m_{\tilde{h}}$ the trilinear scalar interactions allow for the decays $\tilde{s} \rightarrow 2\tilde{h}$. These decays could lead to interesting signatures, such as $4b$ final states, however such signals are not currently accessible at the LHC. As we are considering the sensitivity of the dedicated Higgs searches to Higgs friends and accomplices we can treat this additional width as invisible. Given the physical masses, mixing angle, and scalar potential parameters, one can determine the magnitude of this interaction, which is essentially a free parameter, and the resultant width (see e.g. [94]). As the trilinear coupling is a free parameter we do not lose generality by taking the invisible branching ratio as a free parameter.² We can express this branching ratio in a model-independent sense as

$$\text{BR}(\tilde{s} \rightarrow 2\tilde{h}) = \kappa \left(1 - 4 \frac{m_{\tilde{h}}^2}{m_{\tilde{s}}^2} \right)^{1/2}, \quad (3.3)$$

¹In general α can either be positive or negative.

²Both \tilde{h} and \tilde{s} could also have additional widths to invisible states. For \tilde{s} this is automatically accommodated in this analysis since the invisible width is a free parameter. For \tilde{h} the overall effect is to democratically reduce event rates.

where κ is the branching ratio in the limit $m_{\tilde{s}} \rightarrow \infty$ and the kinematic factors are included such that the branching ratio vanishes at threshold.

Hence for a Higgs friend or accomplice the strength modifiers become

$$\mu = \sin^2 \theta \left(1 - \kappa \sqrt{1 - 4 \frac{m_h^2}{m_{\tilde{s}}^2}} \right), \quad \mu_{\gamma\gamma} = (\sin \theta - \alpha \cos \theta)^2 \left(1 - \kappa \sqrt{1 - 4 \frac{m_h^2}{m_{\tilde{s}}^2}} \right) \quad (3.4)$$

for the $\tilde{s} \rightarrow b\bar{b}, \tau\tau, WW, ZZ$ and $\tilde{s} \rightarrow \gamma\gamma$ channels respectively.

Counting parameters, we have the recently determined parameter of the SM, $m_{\tilde{h}}$, along with four new free parameters $m_{\tilde{s}}$, α , θ and κ . We set $m_{\tilde{h}} = 125.5$ GeV and consider the mass range $120 < m_{\tilde{s}} < 1000$ GeV. As argued above, to a good approximation, the only search channel sensitive to the parameter α is for the decays $h \rightarrow \gamma\gamma$.

One could also consider coupling the scalars to additional colored fields, which would lead to enhanced production in the gluon fusion channel. We will not consider this scenario here for two reasons. Since the enhancement of the diphoton channel, and suppression of the non-diphoton channels, can be easily accommodated in the Higgs accomplice scenario there is little to gain by boosting the Higgs production in this way and the introduction of this additional parameter will not lead to a significant improvement in fitting the data. Also, all Higgs production cross-sections in the models considered here are re-scaled in the same way, so above 150 GeV, where the diphoton searches are not sensitive, one can employ the reported fits for all sub-channels combined. Whereas to consider boosting gluon fusion alone means that all production sub-channels should be treated independently and the relative contributions of gluon fusion and vector boson fusion should be considered independently. As these relative contributions and subsequent likelihoods must be estimated somehow, this leads to the introduction of further error.³

³For a treatment of this scenario with the friend decoupled see [135, 46].

3.2 Statistical Methodology

3.2.1 Likelihood Estimation

Before considering scenarios with multiple Higgs-like scalars we briefly review some methodology regarding Higgs signal strength likelihood functions, which determine the compatibility of Higgs-like signal with the Higgs search results.⁴ Within a particular search channel, limits on a single Higgs particle of mass m_h are expressed in terms of the strength modifier μ , which relates the signal strength to that of a SM Higgs at a given mass, $\mu = n_s/(n_s)^{SM}$, where n_s is the number of signal events expected for the particular search channel. Given the number of observed events n_{obs} , one can construct the likelihood function $\mathcal{L}(n_{obs}|\mu, \theta)$ which is a function of the parameters μ and θ . Here θ stands for a set of nuisance parameters, which are fitted from the data to account for systematic effects and unknown background estimation parameters.

The standard quantity used to test hypotheses or set limits on μ is the so-called profile likelihood ratio [68]

$$\lambda(\mu) = \frac{\mathcal{L}(n_{obs}|\mu, \hat{\theta})}{\mathcal{L}(n_{obs}|\hat{\mu}, \hat{\theta})} , \quad (3.5)$$

where $\hat{\theta}$ is the value of θ that maximizes the likelihood for a specified value of μ , while $\hat{\mu}$ and $\hat{\theta}$ are the maximum likelihood estimators for μ and θ respectively. We do not have access to the full likelihood functions $\mathcal{L}_i(n_{obs}|\mu, \theta_i)$ for the different channels, but given the information available from the experimental collaborations we can reconstruct approximate profile likelihood ratios $\lambda_i(\mu)$. In order to combine results from multiple search channels and different experiments, one should in principle calculate the profile likelihood ratio from the combined likelihood, which can be taken as the product of the different likelihoods if the channels are independent. Given that we

⁴Throughout we employ a frequentist approach. Employing a Bayesian approach allows the likelihoods for strength modifiers to be turned into probability density functions when one includes priors. In this case, if strength modifiers depend on additional parameters then a Jacobian must be used when changing variables, so that the mode of the probability density function may not occur at the same place as the maximum of the likelihood (see for example [67]). The non-invariance of Bayesian estimators under reparametrization motivates our choice of a frequentist approach.

do not know the full likelihood functions, we will take the combined profile likelihood ratio as the product of the $\lambda_i(\mu)$ reconstructed from single channels or experiments

$$\lambda_C(\mu) \simeq \prod_i \lambda_i(\mu) \quad . \quad (3.6)$$

It should be noted, however, that this approximation introduces an additional source of error if significant correlations between channels arise, possibly through the nuisance parameters.

In an abuse of terminology, we will henceforth refer to $\lambda(\mu)$ as the likelihood for μ . In order to reconstruct $\lambda_i(\mu)$, we note that, as described in [160, 68, 24], in the limit where the number of events is sufficiently large, with $n_{obs} \gtrsim 10$, the likelihood for a given channel can be approximated by

$$\lambda(\mu) \simeq e^{-(\mu-\hat{\mu})^2/2\sigma_{obs}^2} \quad , \quad (3.7)$$

where σ_{obs} is in general a function of μ . For the 7 TeV run the best fit strength modifier $\hat{\mu}$ and the error σ_{obs} in individual $\gamma\gamma, \tau\tau, bb, WW$ and ZZ search channels are reported by the ATLAS and CMS collaborations [1, 2] as a function of the Higgs mass.

For most channels the Gaussian approximation, which assumes that σ_{obs} is independent of μ , works well and using the best fit parameters and uncertainties the 95% confidence limits can be reproduced well. However in the $ZZ \rightarrow 4l$ channel the likelihood function is clearly not Gaussian, as can be seen from the asymmetric confidence contours in [1, 2]. Thus the Gaussian assumption is not valid and its use can introduce artificial bias into parameter fits.

We choose to approximate $\lambda(\mu)$ as a two-sided Gaussian, since this captures the approximately Gaussian nature of the likelihood and employs the three pieces of information available at a given mass, namely the best fit point and two values of the log-likelihood away from the best fit point. Using the 7 TeV data we can test this approximation by taking σ on either side of the best fit value of μ from the

1σ values (CMS [2]), or $\Delta(-2\log\lambda) = 1$ contours (ATLAS [1]) provided for the individual channels. Although this approximation is crude, using the 7 TeV data we find that when combining all channels and comparing with the reported combined best fit values the two-sided Gaussian assumption fares reasonably well, and typically better than the standard Gaussian approximation with symmetrized errors. It should be kept in mind that errors of $\mathcal{O}(10-15\%)$ are typical using this approach, combined with an inherent error due to digitization of the data, which we estimate to be as large as $\mathcal{O}(10\%)$.

In some cases μ is the only free parameter, however in more complicated models involving modified Higgs couplings or additional invisible decay widths μ becomes a function (in general different for different channels) of the additional parameters of the model, $\mu^i(\omega)$ where ω denotes all the additional parameters and the superscript denotes the particular search channel. One can find best fit parameters by maximizing the likelihood function and, since the quantity $-2\log\lambda$ should approximately follow a chi-squared distribution [68], one can also test the hypotheses of different models or signal strengths.

3.2.2 Likelihood for Multiple Scalars

Thus far we have only been concerned with models in which the hypothesis is of a single Higgs particle. However in this work we consider models containing two Higgs-like scalars of mass $m_{\bar{h}}$ and $m_{\bar{s}}$, and we must estimate a combined likelihood for both.

The individual searches have differing mass resolutions, from as small as 1 – 3% in the $h \rightarrow \gamma\gamma$ and $h \rightarrow ZZ \rightarrow 4l$ channels up to 20% in the $h \rightarrow \tau\tau$ and $h \rightarrow WW$ channels. Whenever masses are greatly separated, i.e. $|m_{\bar{h}} - m_{\bar{s}}| \gg \sigma_i$ the hypothesized signal from one does not contaminate the search for the other, making the searches effectively independent. In this case the likelihood can be taken as the

product of the two independent likelihoods⁵

$$\lambda_C [\mu_{\tilde{h}}, \mu_{\tilde{s}}, \omega, m_{\tilde{h}}, m_{\tilde{s}}] = \lambda_C [\mu_{\tilde{h}}, \omega, m_{\tilde{h}}] \times \lambda_C [\mu_{\tilde{s}}, \omega, m_{\tilde{s}}] \quad . \quad (3.8)$$

Whenever the Higgs and friend or accomplice are separated by mass splittings within or close to the mass resolution of a given search channel, $|m_{\tilde{h}} - m_{\tilde{s}}| \lesssim \sigma_i$, the situation becomes more complicated. Without performing a full simulation we can still estimate the likelihood in such a scenario based on the mass resolutions provided. However, in a conservative approach, we will not use this estimate to make precise statements about fits in regions where the signal from both scalars overlap, but will instead use it to determine the mass range in which the factorized likelihoods for the scalars can be trusted.

To understand how we estimate the combined likelihood whenever $|m_{\tilde{h}} - m_{\tilde{s}}| \lesssim \sigma_i$, one can first focus on a single search channel and consider a hypothetical situation in which signal from a SM Higgs, of mass m_h , is present in the data. Performing a search for a Higgs of mass m_h , with cuts optimized for this mass, one expects to observe a certain number of signal events $n_s(m_h)$, and to reconstruct a strength modifier at that mass of $\mu(m_h) \approx 1$, up to statistical and systematic errors. However, due to the finite mass resolution, a certain number of events, originating from the Higgs of mass m_h , may also pass the cuts for a Higgs search for a different mass m'_h . Hence looking at searches for different masses one expects to observe a certain number of events $n_s(m'_h) < n_s(m_h)$ and to reconstruct a strength modifier at that mass $\mu(m'_h) < \mu(m_h)$, even though the true Higgs mass is m_h . This makes intuitive sense: for a SM Higgs at mass m_h , with a finite amount of data one would not expect the reconstructed strength modifier to be a precise delta-function but rather it should follow some distribution which is peaked at m_h .

Given that we know $\mu \propto (n_{obs} - n_b) = n_s$ then, regardless of the mass-dependence of the backgrounds, we need only know the dependence of the eventual signal on the

⁵The parameter dependence of the individual likelihoods is not necessarily independent. In the case considered here one might wish, for example, to increase the mixing, which increases the signal from \tilde{s} to explain some excess at $m_{\tilde{s}} \gg m_{\tilde{h}}$. However doing so decreases the signal from \tilde{h} , which may be disfavored by the likelihood for \tilde{h} .

Higgs mass if we want to reconstruct the mass dependence of $\mu(m_h)$. We choose to approximate the functional form to be Gaussian, such that if a SM Higgs is present at mass m_h the number of signal events observed when applying the cuts, and hence searching, for a Higgs of mass m'_h , is

$$n_s(m'_h) = n_s(m_h) e^{\frac{-(m'_h - m_h)^2}{2\sigma^2}} , \quad (3.9)$$

where σ is the mass resolution for that search. For the case of multiple scalars the ATLAS $h \rightarrow WW$ search has been studied in [107]. The mass-dependence of the signal after cuts has been calculated and is shown in Fig 2. of [107] for hypothetical Higgs-like scalars of mass 125 and 170 GeV. One can see that due to the nature of the search the signal is not a delta-function centered at the Higgs mass but is rather a smooth distribution peaked at the true mass. We find that a Gaussian provides a good fit to the data, and so we assume that $\mu(m_h)$ follows the same functional dependence.

Since the signal strength modifier is, by construction, normalized such that if a SM Higgs of mass m_h is present in the data the strength modifier must be $\mu(m_h) \approx 1$, we normalize the Gaussian distribution to have a peak value of 1. Given this assumption, combined with the approximate experimental resolution of the search channel, $\sigma_i(m)$, we estimate the strength modifier contributed by a SM Higgs of mass m_h in a particular search channel to be

$$\mu^i(m) = e^{\frac{-(m - m_h)^2}{2\sigma_i^2(m_h)}} , \quad (3.10)$$

where the normalization is chosen for a SM Higgs. Clearly, to extend this to a non-SM Higgs one includes dependence on any additional parameters by rescaling production cross-sections and branching ratios accordingly. Now to construct a likelihood for two Higgs scalars of mass $m_{\tilde{h}}$ and $m_{\tilde{s}}$ we estimate overlap of strength modifiers through

the combination

$$\begin{aligned}\mu^i(\omega, m_{\tilde{h}}) &= \mu_{\tilde{h}}^i(\omega) + \mu_{\tilde{s}}^i(\omega) e^{-\frac{(m_{\tilde{s}} - m_{\tilde{h}})^2}{2\sigma_i^2(m_{\tilde{h}})}}, \\ \mu^i(\omega, m_{\tilde{s}}) &= \mu_{\tilde{s}}^i(\omega) + \mu_{\tilde{h}}^i(\omega) e^{-\frac{(m_{\tilde{h}} - m_{\tilde{s}})^2}{2\sigma_i^2(m_{\tilde{s}})}}.\end{aligned}\tag{3.11}$$

In this way, if the mass splittings far exceed the experimental resolution the strength modifiers become independent and the likelihood factorizes into individual likelihoods for the independent scalars. However as the masses approach one another signal overlap becomes important, and in the limit where the masses are equal the strength modifiers simply add together, as expected. Alternatively one can think of this as the signal from one scalar acting as known background in the search for the other. This method is clearly approximate, however it should give a reasonable estimate of the combined likelihood given the available information and is useful to determine the mass range in which the factorized likelihoods can be trusted.

We are combining multiple channels and so we must use different resolutions for each channel. CMS reports the approximate mass resolution of the individual channels in [50], which we use, taking the maximum value whenever a range is quoted. We use 3% for the ZZ channel since this is the largest resolution in the individual ZZ sub-channels which are sensitive to a light Higgs. Our results will not be sensitive to this choice, since the dominant source of signal overlap is in the low-resolution channels unless $m_{\tilde{s}} \approx m_{\tilde{h}}$. For ATLAS some resolutions are reported in [1] which are similar to those for the CMS searches. When not reported, we assume the same resolution as in the CMS searches. This assumption does introduce additional error whenever considering limits on scenarios where the scalars are close in mass, however in this region the dominant ATLAS sensitivity is in the $h \rightarrow \gamma\gamma$ and $h \rightarrow ZZ$ channels, with published resolutions, and the $h \rightarrow WW$ channel for which, by comparing with the results of [107], the assumption of 20% mass resolution is valid. As a result it is likely that the overall error introduced into the combined limits and fits through this assumption is subdominant to other sources of error. The chosen mass resolutions are detailed in Table 3.1.

Channel	Resolution [%]
$\gamma\gamma$	3
ZZ	3
bb	10
$\tau\tau$	20
WW	20

Table 3.1: Approximate light Higgs search mass resolutions

3.2.3 Estimating the Importance of Signal Overlap

To estimate the impact of signal overlap on best fit parameters we consider the case with pure Higgs-singlet mixing, setting $\alpha = 0$. In this case strength modifiers for different search channels re-scale in the same way, simplifying the analysis. To perform this estimate we only use the 7 TeV data since best fit parameters and confidence contours are available for both CMS and ATLAS for the $h \rightarrow bb, \tau\tau, WW, ZZ$ and $h \rightarrow \gamma\gamma$ search channels.

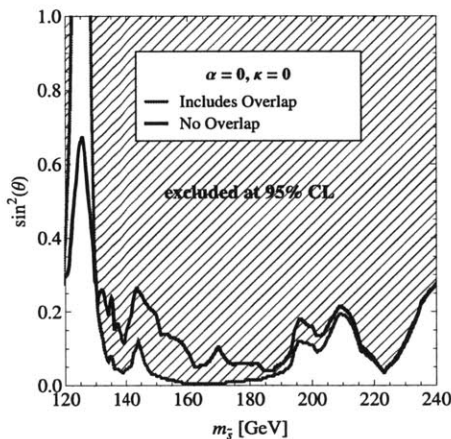


Figure 3-1: The best fit mixing angle as a function of the Higgs friend mass, $m_{\bar{s}}$, for the combined likelihood with signal overlap included (red) and omitted (black). 95% confidence bands are also shown. Above $m_{\bar{s}} \sim 210$ GeV the difference between both methods becomes negligible, demonstrating that above this mass the simple product of individual likelihoods can be trusted. Below this mass the overlap of signal becomes important, suggesting that the simple individual likelihood products lose accuracy.

In Fig. 3-1 we plot, in red, the best fit mixing angle as a function of the singlet mass, $m_{\bar{s}}$, for the combination of likelihoods of both scalars with signal overlap in-

cluded according to Eq. (3.11). Due to a deficit in background events a negative Higgs event rate is, at some masses, preferred by the data. However, since we are fitting to a model restricted to real mixing angles, such negative event rates are not within the parameter space of the model, and these points usually correspond to a best-fit value of $\theta = 0$. We calculate 95% confidence bands by finding the mixing angle at which $\Delta(-2 \log \lambda) \equiv -2(\log \lambda(\mu) - \log \lambda(\hat{\mu})) = 3.84$. As argued in the caption, for $m_{\tilde{s}} \lesssim 210$ GeV the overlap in signal clearly becomes important, and the simple product of likelihoods should not be used.

However, since the best fit values shown in red do accommodate the signal overlap to some degree, we can still extract some qualitative features. Typically for masses $m_{\tilde{s}} \lesssim 200$ GeV the preferred mixing angle is $\theta \approx 0$. This is due to two dominant effects. First of all, small mixing angles are preferred for the fit of $m_{\tilde{h}} = 125.5$ GeV to the 7 TeV data since the signal at this mass prefers $\mu \sim 0.8$, and larger mixing angles which reduce the signal further are penalized. Second, the strong limits for $m_{\tilde{s}} \lesssim 200$ GeV also prefer the signal from the friend to be small, requiring a small mixing angle. One can also see that for $m_{\tilde{s}} \approx m_{\tilde{h}}$ the mixing angle essentially becomes unconstrained. This is due to the fact that in this case each strength modifier is almost independent of θ since $\mu \approx \sin^2(\theta) + \cos^2(\theta) \approx 1$.

3.3 Results

3.3.1 Data

As demonstrated in Sec. 3.2.3, for $m_{\tilde{s}} \gtrsim 210$ GeV we can effectively treat the likelihoods for the scalars individually, taking the product to find the combined likelihood. In this mass range the diphoton search is not sensitive, so we use WW and ZZ channels. Whenever available we use best fit values and confidence contours for the strength modifier. When best fit values are not directly provided we employ expected and observed 95% confidence limits. In [68] it is shown that the best fit strength modifier can be simply approximated by the difference of the observed and expected

upper limits, and the error is given by $\sigma \approx \mu_{exp}^{95\%}/1.64$. We use combined 7 and 8 TeV data from ATLAS and CMS [4, 64, 63, 6, 7, 62].

For the Higgs likelihood at 125.5 GeV we use again the 7 and 8 TeV combined best fit values and corresponding errors for the couplings from ATLAS and CMS [3, 5].

We also use the recent Tevatron data [106], taking the best fit values and uncertainties for the $\gamma\gamma$, WW and bb channels.

With this information we can estimate the full likelihood for both scalars to determine whether a social Higgs allows for any improvement in fitting the data when compared with a SM (antisocial) Higgs.

3.3.2 Higgs Friend and Higgs Accomplice Scenarios

First we consider the friend scenario, where the Higgs is mixed with a singlet scalar. On the left-hand panel of Fig. 3-2 we plot the 95% CL contours for the mixing angle as a function of the singlet mass for $m_{\tilde{s}} > 200$ GeV. The contour for vanishing invisible width is shown in red. We also plot results allowing for the decays $\text{BR}(\tilde{s} \rightarrow 2\tilde{h})$ following Eq. (3.3) with $\kappa = 0.5$ in green. Constraints are weakened by this effectively invisible width due to suppression of the signal, and fits previously requiring some mixing now require greater mixing due to dilution of the signal at high masses.

On the whole, $\sin^2 \theta \gtrsim 0.2$ is excluded at 95% CL over the entire mass range. As a reference, the dashed line shows the limits that we would get by using only the Higgs couplings data at 125.5 GeV. It is interesting to note that the Higgs searches are already sensitive to relatively minor modifications of the Higgs sector.

Whenever we allow for enhancement of the decays $\tilde{h} \rightarrow \gamma\gamma$ by coupling the friend to photons then, regardless of the value of θ , we can always choose the coupling, α , such that $\mu_{\gamma\gamma} > 1$ can be reproduced for the Higgs signals at 125.5 GeV. The other search channels only constrain θ . Furthermore, as the diphoton searches look for resonances below 150 GeV, for $m_{\tilde{s}} > 150$ GeV the likelihood function for \tilde{s} is independent of α . This allows to accommodate better the slight excess in the diphoton channel reported by ATLAS without degrading the fit to the Higgs friend.

On the right-hand panel of Fig. 3-2 we show the 95% confidence contours for θ as

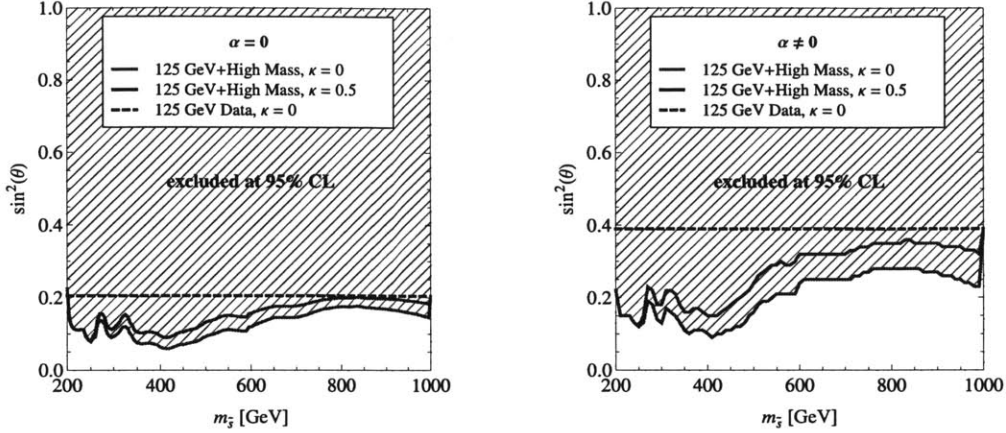


Figure 3-2: 95% confidence limits on the mixing angle as a function of the scalar mass, $m_{\tilde{s}}$, at high masses. The limit of vanishing $\tilde{s} \rightarrow 2\tilde{h}$ branching ratio is shown in red and for $\kappa = 0.5$ (see Eq. (3.3)) in green. On the left panel we set $\alpha = 0$ and allow only mixing with the Higgs friend, with 95% confidence contours determined via $\Delta(-2 \log \lambda) = 3.84$. On the right panel we allow for enhanced $\tilde{h} \rightarrow \gamma\gamma$ decays in the Higgs accomplice scenario and find the best fit values of θ and α . In this case we find 95% confidence contours by finding the maximum value of θ for which $\Delta(-2 \log \lambda) = 5.99$. On both panels it is clear that due to strong limits the SM is preferred over both scenarios over the entire mass range.

a function of $m_{\tilde{s}}$. Although the limits are less stringent compared to the Higgs friend scenario, there is no significant improvement over the SM.

In Fig. 3-3 we show the best fit values as well as 68% and 95% confidence contours, corresponding to $\Delta(-2 \log \lambda) = 2.28$ and $\Delta(-2 \log \lambda) = 5.99$, for α and $\sin^2(\theta)$ whenever \tilde{s} is decoupled and doesn't contribute any signal in the search window. Again, there is no preference for the accomplice scenario as the SM ($\theta = 0, \alpha = 0$) lies within the 68% confidence contour.

3.4 Electroweak Precision Constraints

As pointed out in [36], if the Higgs mixes with a friend then precision electroweak observables are altered in comparison to the SM. In particular, W and Z boson couplings to the Higgs are suppressed, and the friend can also enter at one loop into self-energy graphs. Here we study the differences in the S and T parameters [141, 142] relative

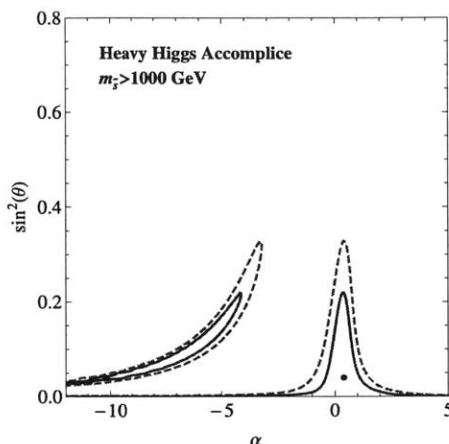


Figure 3-3: Best fit points and 68% and 95% confidence contours, corresponding to $\Delta(-2 \log \lambda) = 2.28, 5.99$ for the specific scenario of a Higgs accomplice beyond collider reach. The SM, $\sin^2(\theta) = 0$, is within the 68% confidence contour, showing no fit improvement of the accomplice scenario over the SM.

to the SM for the Higgs friend model. We calculate these differences at one loop by taking the Higgs contributions to S and T from [109, 110] and re-scaling them by $\cos^2(\theta)$. We also add a similar contribution for the friend and then subtract off values for a SM Higgs at 125.5 GeV.

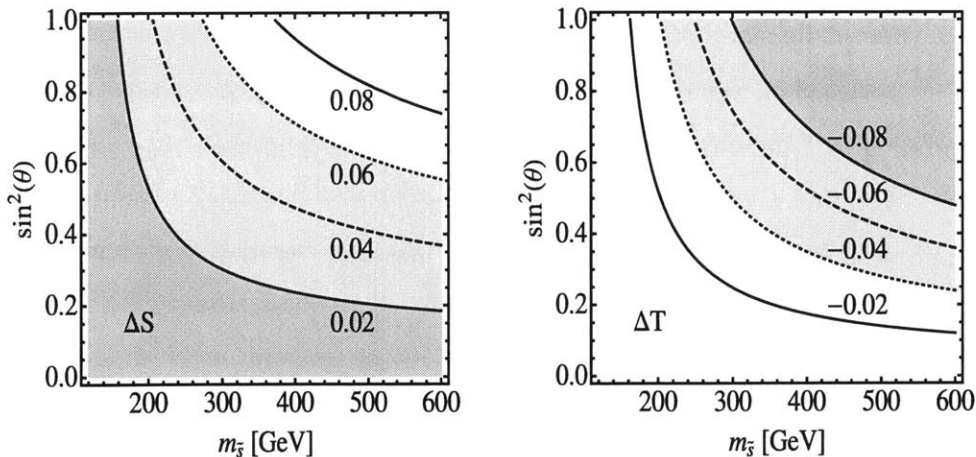


Figure 3-4: Contours of $\Delta S = S(\tilde{h}, \tilde{s}, \theta) - S(h)$ and $\Delta T = T(\tilde{h}, \tilde{s}, \theta) - T(h)$, for the simple Higgs friend model. We have set $m_{\tilde{h}} = m_h = 125.5$ GeV. For the majority of parameter space this model is consistent with electroweak precision data at 1σ .

In Fig. 3-4 we show contours of the change in the S and T parameters relative to the SM with a Higgs at 125.5 GeV. In [31] for a Higgs mass in the range $115.5 < m_h < 127$

GeV the S and T parameters are given as $S = 0.00_{-0.10}^{+0.11}$ and $T = 0.02_{-0.12}^{+0.11}$, so in this model deviations from the SM are typically within 1σ , even with relatively large mixing angles, hence electroweak precision places no strong constraints on models with a relatively light Higgs friend. Heavier Higgs friends are less consistent with electroweak precision constraints, however agreement at close to 1σ can still be found for friends with masses greater than 1 TeV [36].

Statements about precision electroweak observables are model-dependent and if additional electroweak-charged fields are present, as in the Higgs accomplice scenario, or as would be expected in a complete model which addresses fine-tuning issues, then further alterations to the S and T parameters would arise. In either case one must then consult the particular model to establish consistency with electroweak precision data. As such, the bounds shown here should be considered a demonstration of consistency in the friend scenario, rather than a reflection of the consistency of a possible underlying theory.

3.5 Conclusions

Only analyses of future data can convincingly determine whether or not the Higgs boson observed at the LHC is indeed the SM Higgs. However, since there is currently no strong evidence to the contrary, it is now possible to constrain scenarios where the Higgs properties are significantly altered. Furthermore, null results in Higgs searches at other masses already place strong bounds on neutral scalars with Higgs-like production and decay properties. Motivated by this observation, in this chapter we have examined the impact this has on two simple models, the Higgs friend and Higgs accomplice scenarios, which may act as simplified models for theoretically motivated extended Higgs sectors, such as arise in the NMSSM. Both scenarios are still compatible with the data, however mixing angles with the gauge singlet are strongly constrained. Mixing angles with $\sin^2 \theta \gtrsim 0.2$ are typically disfavored at the 95% level over the mass range $200 \text{ GeV} < m_{\tilde{s}} < 1000 \text{ GeV}$.

The analysis presented in this chapter is an update of the analysis in [33], and

includes combined 7 and 8 TeV Higgs data. At the time of the original analysis, the Higgs accomplice scenario provided an improvement on the fit to the data compared to the Standard Model, mainly because of an excess in the $\gamma\gamma$ channel reported both by ATLAS and CMS. At present time, only ATLAS observes a moderate excess in the $\gamma\gamma$ channel, with the CMS measurement consistent with the SM. As shown, with current data, the Higgs accomplice scenario does not provide any statistically significant improvement over the SM fit, and the mixing angle can be strongly constrained.

Chapter 4

A New Approach to Jets

In this chapter we will define a new class of event shapes that capture the jet-like structure of the event. It is worth noting that our approach shares some of the same goals and features as other jet-like methods. For defining jet observables through event shapes, there has been previous work showing how to construct effective jet clustering procedures via optimization of event shapes [89], most recently in taking N -jettiness [153] and minimizing over the choice of jet axes [156]. The difference here is that our jet-like event shapes do not have an obvious clustering interpretation. There are also methods that cast jet finding as a more general optimization problem [30, 20, 21, 105, 104, 53, 124, 159, 90, 117], often with a probabilistic interpretation of an event. The difference here is that we (uniquely) assign an event shape value to each event. A set of variables that avoids explicit jet clustering are energy correlation functions [126], which can characterize an event's structure without reference to even a jet axis (in contrast to N -jettiness), though different correlation functions are needed for different jet multiplicities. The difference here is that we need not specify the jet multiplicity of interest, though we do need to choose the jet radius R and threshold $p_{T\text{cut}}$. Finally, for giving a global characterization of an event, there has been recent work to describe the jet-like nature of an event by summing over the contributions of large radius jets [114, 61, 85], though these observables make explicit use of tree-like recursive jet algorithms. The difference here is that we can achieve a similar global characterization through an inclusive sum over all particles in an event.

The chapter is organized as follows: we define event shapes for inclusive jet observables in Sec. 4.1 and perform Monte Carlo studies to demonstrate the correlations present with their jet-based cousins. We then show in Sec. 4.2 how to manipulate and modify these event shapes to characterize the properties of individual jets, in particular how to find the jet constituents using a hybrid event shape density with a “winner-take-all” recombination scheme. We describe our shape trimming technique in Sec. 4.3 and show how it is closely correlated with ordinary tree trimming. We suggest possible generalization of our method in Sec. 4.4 and draw conclusions in Sec. 4.5. This chapter is based on [32].

4.1 Event Shapes for Inclusive Jet Observables

Jet multiplicity (N_{jet}), summed scalar transverse momentum (H_T), and missing transverse momentum (\cancel{p}_T) are three of the most ubiquitous observables used to globally characterize an event with jets in the final state. Given jets identified through some jet algorithm with characteristic radius R , they are defined as

$$N_{\text{jet}}(p_{T\text{cut}}, R) = \sum_{\text{jets}} \Theta(p_{T\text{jet}} - p_{T\text{cut}}), \quad (4.1)$$

$$H_T(p_{T\text{cut}}, R) = \sum_{\text{jets}} p_{T\text{jet}} \Theta(p_{T\text{jet}} - p_{T\text{cut}}), \quad (4.2)$$

$$\cancel{p}_T(p_{T\text{cut}}, R) = \left| \sum_{\text{jets}} \vec{p}_{T\text{jet}} \Theta(p_{T\text{jet}} - p_{T\text{cut}}) \right|, \quad (4.3)$$

where $\vec{p}_{T\text{jet}}$ is the transverse momentum measured with respect to the beam axis, $p_{T\text{jet}} = |\vec{p}_{T\text{jet}}|$, and $p_{T\text{cut}}$ is the p_T threshold for the analysis.¹ We have made the arguments $p_{T\text{cut}}$ and R explicit in anticipation of the discussion in Sec. 4.2. These three observables are part of a broader class of inclusive jet observables

$$\mathcal{F}(p_{T\text{cut}}, R) = \sum_{\text{jets}} \mathcal{F}_{\text{jet}} \Theta(p_{T\text{jet}} - p_{T\text{cut}}), \quad (4.4)$$

¹Typically, \cancel{p}_T would include non-hadronic objects in the event as well, but we will not need that for the case studies here.

where $\mathcal{F}_{\text{jet}} = f(\{p_j^\mu\}_{j \in \text{jet}})$ depends on the kinematics of the individual jet constituents.

As written, \mathcal{F} is intrinsically tied to a given jet algorithm. Here, we wish to build a corresponding event shape $\tilde{\mathcal{F}}$ which makes no reference to a clustering procedure. The first step is to effectively replace the sum over jets with a sum over particles, using the fact that

$$1 = \frac{1}{p_{T\text{jet}}} \sum_{i \in \text{jet}} p_{Ti}, \quad \sum_{\text{jets}} \sum_{i \in \text{jet}} \Rightarrow \sum_{i \in \text{event}}, \quad (4.5)$$

where we now use a more convenient definition $p_{T\text{jet}} \equiv \sum_{i \in \text{jet}} p_{Ti}$ such that the first expression is a strict equality,² and the second expression has an implicit restriction to particles i which are part of a jet cluster. The second step is to convert jet measurements into measurements on jet-like cones of radius R around each particle:

$$\mathcal{F}_{\text{jet}} = f(\{p_j^\mu\}_{j \in \text{jet}}) \Rightarrow \mathcal{F}_{i,R} = f(\{p_j^\mu \Theta(R - \Delta R_{ij})\}_{j \in \text{event}}), \quad (4.6)$$

$$p_{T\text{jet}} = \sum_{i \in \text{jet}} p_{Ti} \Rightarrow p_{Ti,R} = \sum_{j \in \text{event}} p_{Tj} \Theta(R - \Delta R_{ij}), \quad (4.7)$$

where $\Delta R_{ij} = \sqrt{\Delta \eta_{ij}^2 + \Delta \phi_{ij}^2}$ is the distance in the rapidity-azimuth plane, and $p_{Ti,R}$ is the sum of transverse momentum contained in a cone of radius R around particle i . Applying these two steps, we derive the event shape associated with the generic inclusive jet observable in Eq. (4.4):

$$\tilde{\mathcal{F}}(p_{T\text{cut}}, R) = \sum_{i \in \text{event}} \frac{p_{Ti}}{p_{Ti,R}} \mathcal{F}_{i,R} \Theta(p_{Ti,R} - p_{T\text{cut}}). \quad (4.8)$$

Because of the weight factor $p_{Ti}/p_{Ti,R}$, this definition avoids double-counting, even though the jet-like cones around each particle are overlapping. As long as the original \mathcal{F}_{jet} was infrared/collinear safe, then $\tilde{\mathcal{F}}$ will also be infrared/collinear safe (assuming $p_{T\text{cut}} > 0$). Our general strategy is depicted in Fig. 4-1.

Following this logic, we define the following jet-like event shapes corresponding to

²Note that the two definitions $p_{T\text{jet}} \equiv |\vec{p}_{T\text{jet}}|$ vs. $\sum_{i \in \text{jet}} p_{Ti}$ yield the same value for infinitely narrow jets. Instead of p_T , one could accomplish the same goal using the energy relation $1 = (1/E_{\text{jet}}) \sum_{i \in \text{jet}} E_i$.

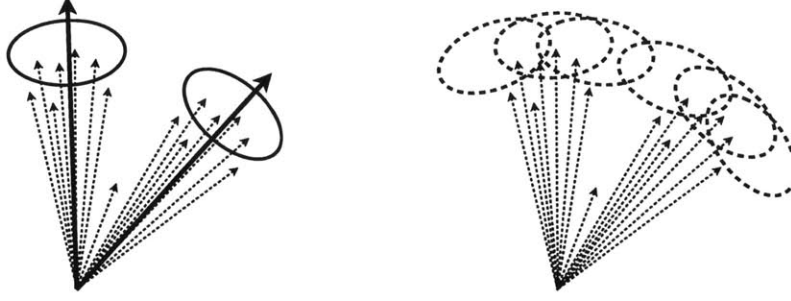


Figure 4-1: Instead of defining inclusive jet observables by summing over jet regions according to a jet algorithm (left), our event shapes sum over the contributions from cones of radius R centered on each particle i (right). The weight factor $p_{Ti}/p_{Ti,R}$ in Eq. (4.8) avoids double-counting despite overlapping cones. For infinitely narrow jets separated by more than R , the two methods yield the same result.

N_{jet} , H_T , and \not{p}_T :

$$\tilde{N}_{\text{jet}}(p_{T\text{cut}}, R) = \sum_{i \in \text{event}} \frac{p_{Ti}}{p_{Ti,R}} \Theta(p_{Ti,R} - p_{T\text{cut}}), \quad (4.9)$$

$$\tilde{H}_T(p_{T\text{cut}}, R) = \sum_{i \in \text{event}} p_{Ti} \Theta(p_{Ti,R} - p_{T\text{cut}}), \quad (4.10)$$

$$\tilde{\not{p}}_T(p_{T\text{cut}}, R) = \left| \sum_{i \in \text{event}} \vec{p}_{Ti} \Theta(p_{Ti,R} - p_{T\text{cut}}) \right|, \quad (4.11)$$

where $p_{Ti,R}$ is defined in Eq. (4.7). For the sake of simplicity, in Eq. (4.11) we approximated $\vec{p}_{Ti,R} \approx p_{Ti,R} \hat{p}_{Ti}$, which is strictly true only for infinitely narrow jets.³ For events consisting of infinitely narrow jets separated by more than R , the event shapes \tilde{N}_{jet} , \tilde{H}_T , and $\tilde{\not{p}}_T$ yield identical values to their jet-based counterparts N_{jet} , H_T , and \not{p}_T . We describe applications and generalizations of this procedure to other inclusive jet (and subjet) observables in Sec. 4.4.

To get a sense for how these event shapes behave, it is useful to study how they correlate with their jet-based counterparts. For this study, we generate event samples for the $\sqrt{s} = 8$ TeV LHC in MADGRAPH 5 [18], with showering and hadronization

³Alternatively, one could recover Eq. (4.11) by noticing that if we assume $\mathcal{F}_{\text{jet}} \equiv \vec{p}_{T\text{jet}} \simeq \sum_{j \in \text{jet}} \vec{p}_{Tj}$, then we can skip the first replacement in Eq. (4.5), and directly convert the double sum into a sum over the event.

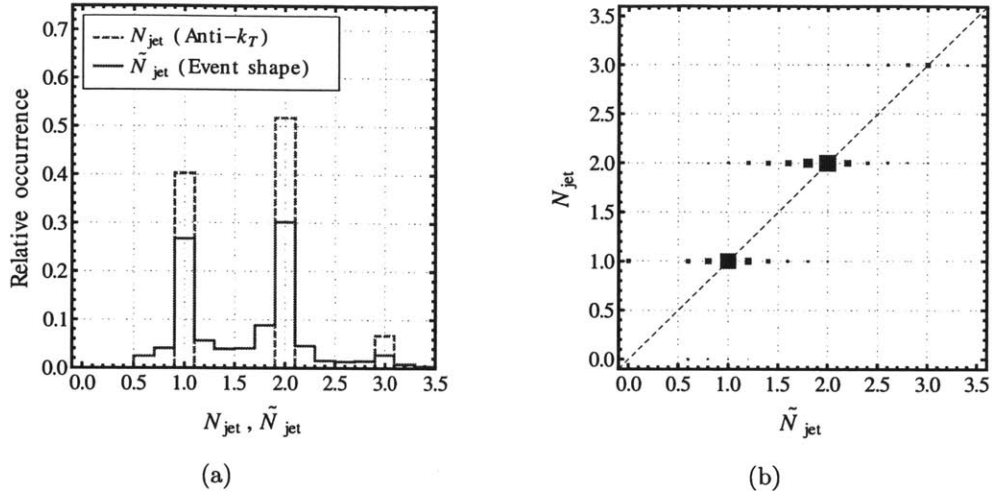


Figure 4-2: Jet multiplicity (i.e. N_{jet}) for QCD dijet events. Fig. 4-2a shows the distribution of the number of anti- k_T jets with $R = 0.6$ and $p_{T\text{cut}} = 25$ GeV (green dashed curve), and of the corresponding event shape with the same values of R and $p_{T\text{cut}}$ (red curve). Only events with $N_{\text{jet}} \geq 1$ or $\tilde{N}_{\text{jet}} \geq 0.5$ are shown, and a parton level cut of $p_{T\text{cut}}^{\text{parton}} = 25$ GeV is employed to give a reasonable sample of both one jet and two jet events. Whereas N_{jet} takes on only integer values, the event shape \tilde{N}_{jet} is continuous, albeit with spikes near integer values. Fig. 4-2b shows the correlation between the two observables, where the area of the squares is proportional to the fraction of events in each bin. In the correlation plot, events that fail one of the jet cut criteria are assigned the corresponding value of zero.

carried out in PYTHIA 8.157 [150].⁴ For the standard jet-based observables, we use FASTJET 3.0.2 with the anti- k_T jet algorithm [42] with a jet radius $R = 0.6$ and $p_{T\text{cut}} = 25$ GeV. For the event shapes, we use the same value of R and $p_{T\text{cut}}$. In order to (artificially) highlight the behavior of our event shapes on both one jet and two jet events, we set the minimum p_T at the parton level in MADGRAPH to $p_{T\text{cut}}^{\text{parton}} = 25$ GeV.⁵

In Fig. 4-2, we compare N_{jet} versus \tilde{N}_{jet} for QCD dijet events. Whereas N_{jet} takes on discrete values, \tilde{N}_{jet} yields a continuous distribution, though the observables are correlated on an event-by-event basis. Here and in the following plots we only show events with $N_{\text{jet}} \geq 1$ and $\tilde{N}_{\text{jet}} \geq 0.5$; the choice of the lower limit on \tilde{N}_{jet} will be

⁴Unless otherwise specified, this will be the standard setup for Monte Carlo studies throughout the chapter.

⁵Without a $p_{T\text{cut}}^{\text{parton}}$ cut, there would of course be more one jet than two jet events. We checked that the event shape distributions remain correlated with their jet-based counterparts as $p_{T\text{cut}}^{\text{parton}} \rightarrow 0$.

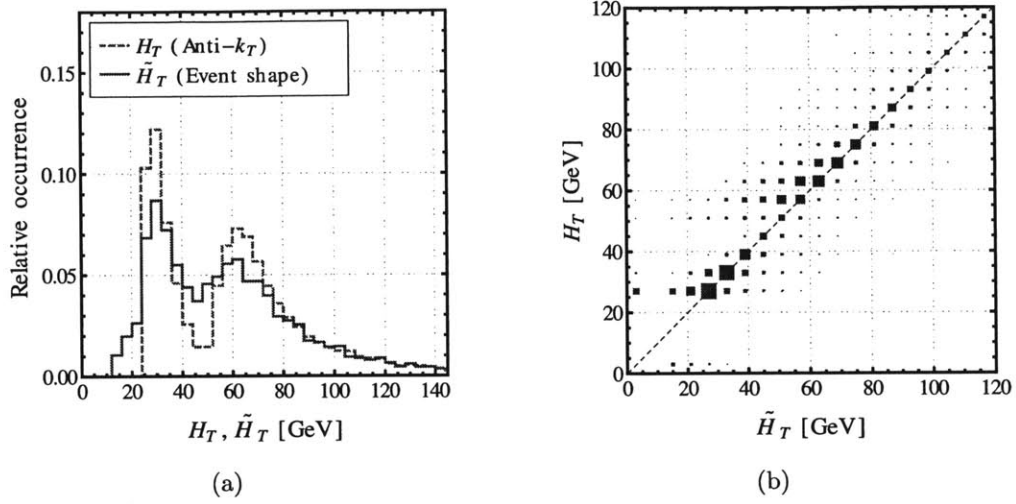


Figure 4-3: Summed scalar transverse momentum (i.e. H_T) for QCD dijet events. The jet parameters, formatting, and cuts are the same as for Fig. 4-2. Because of the smoother behavior of the event shape \tilde{H}_T , the peaks rising at $p_{T\text{cut}}$ and $2p_{T\text{cut}}$ are less pronounced than for H_T .

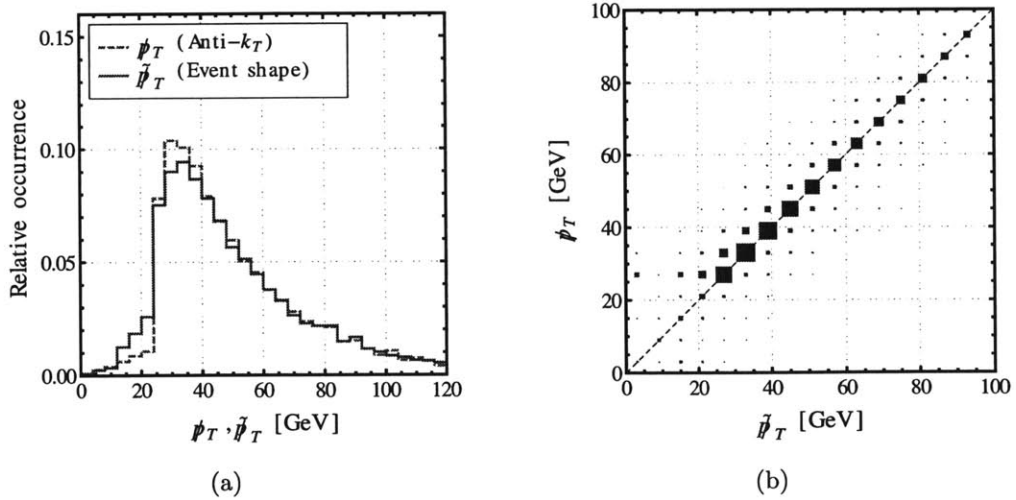


Figure 4-4: Missing transverse momentum (i.e. p_T) for $Z(\rightarrow \nu\bar{\nu}) + j$ events. The jet parameters, formatting, and cuts are the same as for Fig. 4-2. Again, we see a smoother turn on behavior for \tilde{p}_T compared to p_T .

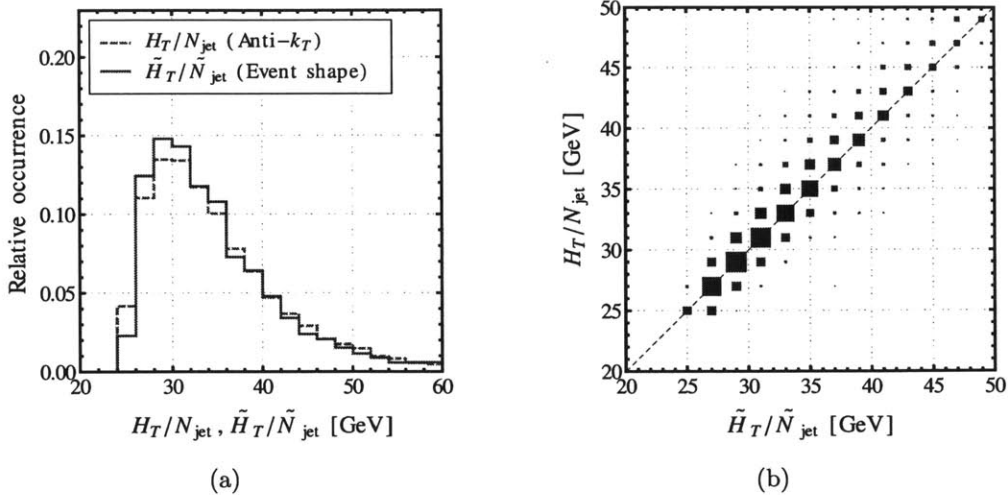


Figure 4-5: Average jet transverse momentum (i.e. H_T divided by N_{jet}) for QCD dijet events. The jet parameters, formatting, and cuts are the same as for Fig. 4-2.

justified in Sec. 4.2.1. In Fig. 4-3, we compare H_T versus \tilde{H}_T again for QCD dijet events. Because of the $p_{T\text{cut}} = 25$ GeV cut, H_T exhibits two spikes that rise starting at 25 GeV (for one jet events) and 50 GeV (for two jet events), whereas \tilde{H}_T is smoother in this turn-on region.⁶ In the tail region, the distributions of H_T and \tilde{H}_T are very similar. In Fig. 4-4, we compare \not{p}_T versus $\tilde{\not{p}}_T$ for Z plus jet events where the Z decays to neutrinos. Again we see a spike that rises starting at 25 GeV for \not{p}_T which is milder in the event shape $\tilde{\not{p}}_T$, though the distributions are quite similar throughout.

Just as for ordinary jet-based observables, one can construct interesting composite functions with the event shapes. For example, one can consider the average p_T of the jets in an event, and we compare H_T/N_{jet} versus $\tilde{H}_T/\tilde{N}_{\text{jet}}$ in Fig. 4-5. Another useful composite variable is missing p_T significance [119, 136], and we compare $\not{p}_T/\sqrt{H_T}$ versus $\tilde{\not{p}}_T/\sqrt{\tilde{H}_T}$ in Fig. 4-6.

The differences between the jet-like event shapes and their jet-based counterparts reflects the intrinsic ambiguity in how to define a jet, seen most strikingly in the fact that \tilde{N}_{jet} does not take on integer values. For jet observables that are inclusive over all

⁶With $p_{T\text{cut}}^{\text{parton}} \rightarrow 0$, the same features are visible, albeit with the one jet spike being much larger than the two jet spike.

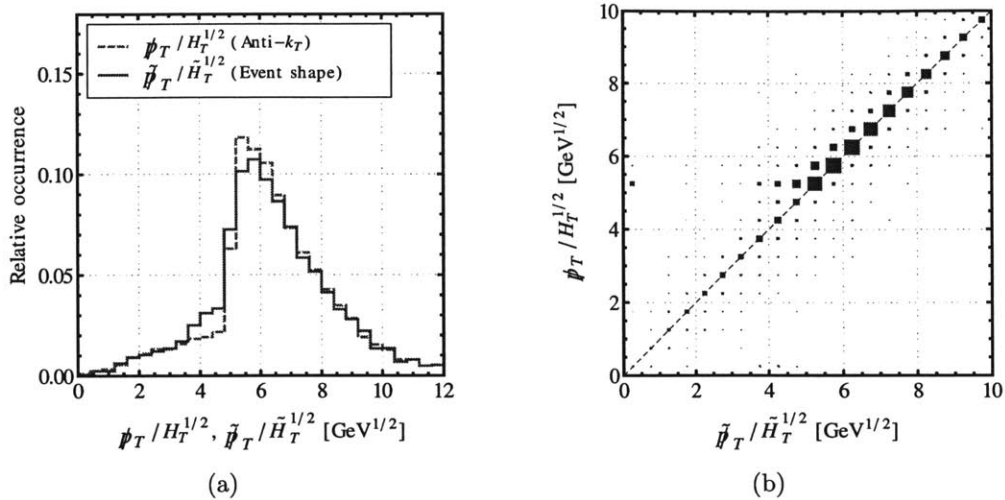


Figure 4-6: Missing transverse momentum significance (i.e. \cancel{p}_T divided by $\sqrt{H_T}$) for $Z(\rightarrow \nu\bar{\nu}) + j$ events. The jet parameters, formatting, and cuts are the same as for Fig. 4-2.

jets, \tilde{N}_{jet} , \tilde{H}_T , and $\tilde{\cancel{p}}_T$ characterize the global properties of the event without defining a clustering procedure, and appear to give very similar information to N_{jet} , H_T , and \cancel{p}_T for the same values of R and $p_{T\text{cut}}$. Of course, because there is no clustering, one cannot determine the kinematics of any individual jet with the event shape alone (see however Sec. 4.2 below). In terms of computational costs, the bottleneck is calculating $p_{T_{i,R}}$ in Eq. (4.7) for every particle i , which naively scales like N^2 for an event with N hadrons, though the computational costs are dramatically reduced if one has an efficient way to determine which particles are within a radius R of particle i .⁷ In practice, calculating \tilde{N}_{jet} using our FASTJET 3 add-on with a standard laptop takes about as long as calculating N_{jet} with anti- k_T . Moreover, \tilde{N}_{jet} can be parallelized since it only depends on the contributions from particles within a radius R (i.e. it is defined “locally”). This feature makes it possible to implement \tilde{N}_{jet} in a low-level trigger for sufficiently small R . The key question at the trigger level is whether an event-shape-based trigger has better properties (e.g. turn-on, stability, calibration,

⁷In our FASTJET add-on, we make a crude attempt in this direction by partitioning the event into overlapping blocks of size $2R \times 2R$ and by caching the results of repeated calculations. Our implementation could potentially be further optimized by using, for example, an alternative distance heuristic.

etc.) than a jet-based trigger, but a detailed study of this issue is beyond the scope of this work.

4.2 Characterizing Individual Jets

While inclusive jet observables are useful for characterizing the gross properties of an event, one would still like to gain more exclusive information about the kinematics of individual jets. In general, our jet-like event shapes do not yield that kind of exclusive information, but we will demonstrate a novel way to extract the (approximate) transverse momentum of individual jets by using the full functional form of \tilde{N}_{jet} . We will then define a hybrid event shape density that incorporates (local) jet clustering information in order to determine the constituents of individual jets.

4.2.1 Jet Transverse Momentum

Consider the jet multiplicity event shape $\tilde{N}_{\text{jet}}(p_{T\text{cut}}, R)$. As shown in App. D, there is a computationally efficient way to find the pseudo-inverse of this function with respect to $p_{T\text{cut}}$, namely $p_{T\text{cut}}(\tilde{N}_{\text{jet}}, R)$.⁸ We will see in a moment that it is useful to introduce an offset n_{off} , so we define

$$\tilde{p}_T(n, R) = p_{T\text{cut}}(n - n_{\text{off}}, R) \quad \text{with} \quad 0 \lesssim n_{\text{off}} \lesssim 1, \quad (4.12)$$

where the default value of n_{off} is 0.5. The corresponding function for ordinary jets is denoted $p_T(n, R)$.

The function $\tilde{p}_T(n, R)$ effectively gives the p_T of the n -th hardest jet. That is, it gives the value of the p_T threshold needed to include the n -th jet's contribution to \tilde{N}_{jet} . For infinitely narrow jets separated by more than R , $p_{T\text{cut}}(\tilde{N}_{\text{jet}}, R)$ takes discrete jumps as \tilde{N}_{jet} increases by integer values. More generally, the offset n_{off} accounts for the fact that an event with n jets most likely returns a value of \tilde{N}_{jet} between $n - 1$

⁸The reason this is a pseudo-inverse is that $\tilde{N}_{\text{jet}}(p_{T\text{cut}}, R)$ is a monotonically decreasing step-wise function of $p_{T\text{cut}}$, so there is a range of values of $p_{T\text{cut}}$ with the same \tilde{N}_{jet} . Once the values of $p_{Ti,R}$ are known, the algorithm in App. D scales like $N \log N$ for N particles.

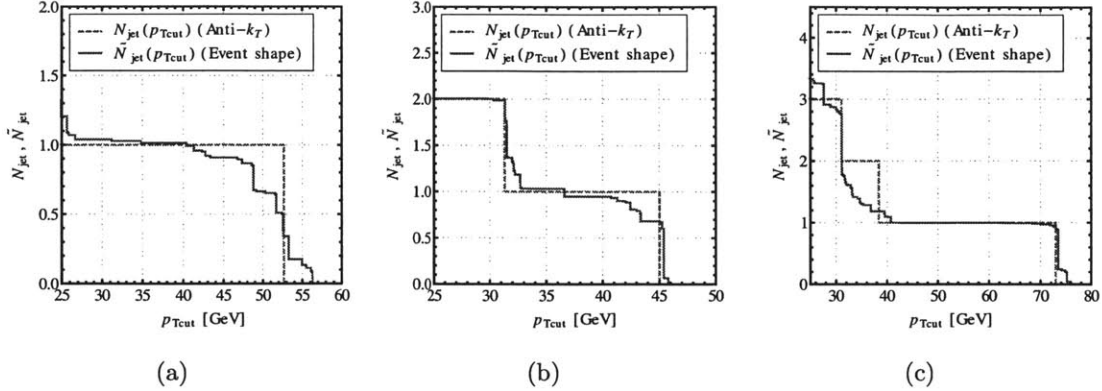


Figure 4-7: Number of jets N_{jet} as a function of $p_{T\text{cut}}$ for fixed $R = 0.6$, for three QCD dijet events. Figs. 4-7a, 4-7b, and 4-7c show example events with 1, 2, and 3 anti- k_T jets with $p_T > 25$ GeV, respectively. The anti- k_T curve (green dashed line) takes integer steps at values of $p_{T\text{cut}}$ corresponding to the p_T of the jets. The event shape curve (red line) takes smaller steps, and it roughly intersects the anti- k_T curve at $\tilde{N}_{\text{jet}} = \{0.5, 1.5, 2.5\}$.

and n .

Using the same QCD dijet event samples as in Sec. 4.1, we can see how well $\tilde{p}_T(n, R)$ corresponds to $p_T(n, R)$. First in Fig. 4-7, we show the function $\tilde{N}_{\text{jet}}(p_{T\text{cut}}, R)$ for individual events compared to $N_{\text{jet}}(p_{T\text{cut}}, R)$, fixing $R = 0.6$. Besides the obvious point that N_{jet} takes integer steps whereas \tilde{N}_{jet} takes smaller steps, we see that the curves roughly intersect at values of $\tilde{N}_{\text{jet}} = 0.5, 1.5, 2.5$, justifying the default value $n_{\text{off}} = 0.5$. In Fig. 4-8, we compare $\tilde{p}_T(n, R)$ versus $p_T(n, R)$ for $n = 1, 2, 3$, where we see that they are highly correlated, as expected from the correlations already seen in the inclusive observables in Sec. 4.1.

Besides just measuring the p_T of the n -th hardest jet, $\tilde{p}_T(n, R)$ can be used to mimic analyses that require a fixed number of jets. For example, one may wish to measure H_T on just the n hardest jets above a given $p_{T\text{cut}}$. To do that with the event shape, one has to find the value of a new scale $p'_{T\text{cut}}$ such that $(n + 1)$ -th jet would not contribute to \tilde{H}_T but the n -th jet is largely unmodified. A convenient choice for that scale is

$$p'_{T\text{cut}} = \max\{p_{T\text{cut}}, \tilde{p}_T(n + 1)\}, \quad (4.13)$$

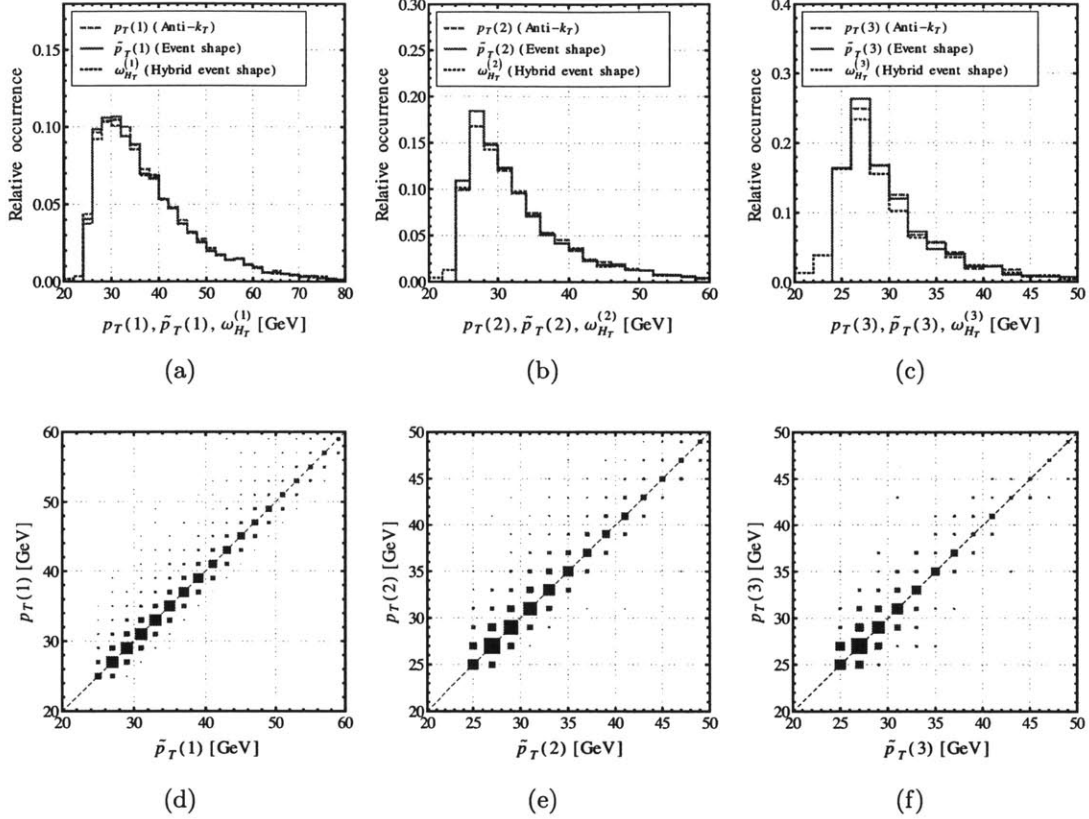


Figure 4-8: Transverse momentum of the three hardest jets (i.e. $p_T(1)$, $p_T(2)$, and $p_T(3)$ from left to right) for QCD dijet events. The top panels shows the transverse momentum distributions for anti- k_T jets with $R = 0.6$ and $p_{T\text{cut}} = 25$ GeV (green dashed curve), the corresponding event shape $\tilde{p}_T(n)$ with the same R and $p_{T\text{cut}}$ (red curve), and the weights $\omega_{Hr}^{(n)}$ returned by the hybrid event shape with the same R but $p_{T\text{cut}} = 0$ (purple dotted curve, see Sec. 4.2.2). The bottom panels shows the correlations between $p_T(n)$ and $\tilde{p}_T(n)$, with the area of the squares proportional to the fraction of events in each bin. For plots of the {1st,2nd,3rd}-hardest jets, the corresponding selection criteria are $N_{\text{jet}} \geq 1, 2, 3$ (for anti- k_T) and $\tilde{N}_{\text{jet}} \geq 0.5, 1.5, 2.5$ (for the event shape).

and we will use $p'_{T\text{cut}}$ in some of the studies in Sec. 4.4.

By using an algorithm similar to the one described in App. D, one could also try to invert the number of jets $\tilde{N}_{\text{jet}}(R)$ as a function of R , for fixed $p_{T\text{cut}}$. Strictly speaking this inverse is not possible, since $\tilde{N}_{\text{jet}}(R)$ is not guaranteed to be a monotonic function of R . Still, we expect that the R dependence of the event shapes could be exploited much in the same way as for telescoping jets [59]. For example, one could measure

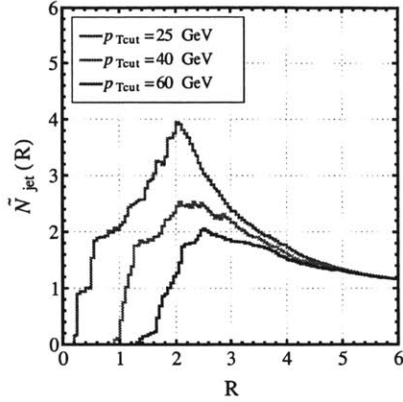


Figure 4-9: Number of jets \tilde{N}_{jet} as a function of R for a single QCD dijet event. Shown are three values of $p_{T\text{cut}} = \{25 \text{ GeV}, 40 \text{ GeV}, 60 \text{ GeV}\}$.

the volatility of an event shape (à la Q -jets [90, 117]) as R is varied. A detailed study of R dependence is beyond the scope of this work, but in Fig. 4-9 we show an example of $\tilde{N}_{\text{jet}}(R)$ for a QCD dijet event, which suggests that there is interesting information to be gained by looking at multiple R values.

4.2.2 Jet Axes and Constituents

By themselves, the event shapes do not have a clustering interpretation, so in order to (uniquely) assign particles to jets we will build a hybrid event shape that incorporates some kind of clustering procedure. Before doing that, though, it is helpful to introduce the concept of an “event shape density”.

Consider the following probability density for a jet axis to lie in a given direction \hat{n} , as determined by a standard jet clustering algorithm:

$$\rho_{N_{\text{jet}}}(\hat{n}) = \sum_{\text{jets}} \delta(\hat{n} - \hat{n}_{\text{jet}}^r) \Theta(p_{T\text{jet}} - p_{T\text{cut}}), \quad (4.14)$$

where the superscript r reminds us that we must choose a recombination scheme for defining the jet axis \hat{n}_{jet}^r in terms of the constituents of that jet. For example, in the standard E -scheme, the jet axis lies in the direction of the summed constituent four-momenta. The reason $\rho_{N_{\text{jet}}}$ is a density is that if we integrate over all directions

\hat{n} then $\int d^2\hat{n} \rho_{N_{\text{jet}}} = N_{\text{jet}}$, but $\rho_{N_{\text{jet}}}$ itself has delta function spikes at the jet locations \hat{n}_{jet}^r identified by the jet algorithm. Similarly, we can define a transverse momentum density,

$$\rho_{H_T}(\hat{n}) = \sum_{\text{jets}} p_{T\text{jet}} \delta(\hat{n} - \hat{n}_{\text{jet}}) \Theta(p_{T\text{jet}} - p_{T\text{cut}}), \quad (4.15)$$

where $\int d^2\hat{n} \rho_{H_T} = H_T$ and the height of the delta functions correspond to the p_T of the corresponding jets.

Following the general strategy outlined in Sec. 4.1, we can define corresponding event shape densities:

$$\tilde{\rho}_{N_{\text{jet}}}(\hat{n}) = \sum_{i \in \text{event}} \frac{p_{Ti}}{p_{Ti,R}} \delta(\hat{n} - \hat{n}_{i,R}^r) \Theta(p_{Ti,R} - p_{T\text{cut}}), \quad (4.16)$$

$$\tilde{\rho}_{H_T}(\hat{n}) = \sum_{i \in \text{event}} p_{Ti} \delta(\hat{n} - \hat{n}_{i,R}^r) \Theta(p_{Ti,R} - p_{T\text{cut}}), \quad (4.17)$$

where $\int d^2\hat{n} \tilde{\rho}_{N_{\text{jet}}} = \tilde{N}_{\text{jet}}$ and $\int d^2\hat{n} \tilde{\rho}_{H_T} = \tilde{H}_T$. Here, $\hat{n}_{i,R}^r$ is the direction of the recombined momenta in a cone of radius R around particle i , which of course depends on the recombination scheme r . If we choose to do recombination via the E -scheme, then $\tilde{\rho}_{N_{\text{jet}}}$ and $\tilde{\rho}_{H_T}$ can still be considered event shapes, since $\hat{n}_{i,R}^r$ can be written in closed form (i.e. in terms of the four-vector sum of constituents). For more general recombination schemes, though, $\tilde{\rho}_{N_{\text{jet}}}$ and $\tilde{\rho}_{H_T}$ are hybrid event shapes, since the specific direction of $\hat{n}_{i,R}^r$ depends on the recombination algorithm (which in general cannot be written in closed form). In contrast to standard jet clustering algorithms, finding $\hat{n}_{i,R}^r$ is a “local” procedure since it only requires knowledge about particles within a radius R of particle i .

Whereas the jet-based densities have n delta function spikes for an n -jet event, the event shape densities typically exhibit a more continuous distribution. In particular, the distribution will still show peaks corresponding to jet directions, although smeared because nearby particles will typically have (slightly) different values of $\hat{n}_{i,R}^r$. In this way, the event shape densities are similar in spirit to the jet energy flow project [30],

since they effectively give a probability distribution for the jet axis locations.

Concretely, if we let $\{\hat{m}_j^r\}$ be the set of distinct directions in $\{\hat{n}_{i,R}^r\}$, we can rewrite the distributions in Eqs. (4.16) and (4.17) as

$$\tilde{\rho}_X(\hat{n}) = \sum_j \omega_{Xj} \delta(\hat{n} - \hat{m}_j^r), \quad X = N_{\text{jet}}, H_T. \quad (4.18)$$

The coefficients ω_{Xj} can be thought as weights corresponding to each candidate jet axis \hat{m}_j^r and are given by:

$$\begin{aligned} \omega_{N_{\text{jet}}j} &= \sum_{i \in \text{event}} \frac{p_{Ti}}{p_{Ti,R}} \Theta(p_{Ti,R} - p_{T\text{cut}}) \delta_{\{\hat{n}_{i,R}^r; m_j^r\}}, \\ \omega_{H_Tj} &= \sum_{i \in \text{event}} p_{Ti} \Theta(p_{Ti,R} - p_{T\text{cut}}) \delta_{\{\hat{n}_{i,R}^r; m_j^r\}}, \end{aligned} \quad (4.19)$$

where $\delta_{\{\hat{n}_{i,R}^r; m_j^r\}}$ is a Kronecker delta over the discrete sets of directions $\{\hat{n}_{i,R}^r\}$ and $\{m_j^r\}$. The weights $\omega_{N_{\text{jet}}j}$ indicate the (fractional) number of jets that should be associated with a given axis, while ω_{H_Tj} indicate the associated transverse momentum. For an isolated narrow jet, a typical recombination scheme will yield a single axis \hat{m}^r with $\omega_{N_{\text{jet}}} = 1$ and $\omega_{H_T} = p_{T\text{jet}}$.

We emphasize that in this hybrid approach, a separate clustering algorithm is applied to each particle i , using just the particles within its neighborhood of radius R . For an event with N final state hadrons, one has to run N clustering algorithms, yielding N values of $\hat{n}_{i,R}^r$, though not all of them will be distinct. In practice, it is inconvenient to have $\mathcal{O}(N)$ candidate jet axis locations, so ideally we want a recombination scheme that returns $\mathcal{O}(n)$ unique axes \hat{m}_j^r for an n -jet event.

For this purpose, we will use a “winner-take-all” recombination scheme when performing the local clustering around each particle.⁹ This scheme guarantees that the recombined direction will always coincides with one of the input particles, dramatically decreasing the number of unique \hat{m}_j^r values. In the context of a pairwise cluster-

⁹We thank Andrew Larkoski, Duff Neill, and Gavin Salam for discussions on this point. The winner-take-all scheme is also discussed in Ref. [125] in the context of recoil-free observables.

ing algorithm like anti- k_T , the recombination scheme determines how two pseudo-jets p_1 and p_2 will be merged to form a combined pseudo-jet p_r . In the winner-take-all scheme, the transverse momentum of p_r is given by the sum of the two pseudo-jets, but the direction of p_r is given by the hardest pseudo-jet:

$$p_{Tr} = p_{T1} + p_{T2}, \quad \hat{n}_r = \begin{cases} \hat{n}_1 & \text{if } p_{T1} > p_{T2}, \\ \hat{n}_2 & \text{if } p_{T2} > p_{T1}. \end{cases} \quad (4.20)$$

For simplicity, we take p_r to be a massless four-vector. When used with an infrared/collinear safe clustering measure (anti- k_T in the later plots), the winner-take-all scheme is also infrared/collinear safe. Because the winner-take-all scheme always returns a jet direction aligned along one of the input particles (often the hardest particle), the set of recombined jet directions $\{\hat{m}_j^r\}$ is much smaller than the number of hadrons in the final state.¹⁰ Of course, for later analysis, one probably wants to use the summed four-vector of the jet constituents instead of the jet axis.¹¹

Another practical consideration concerns the value of $p_{T\text{cut}}$. As stated above, one can think of ω_{HTj} in Eq. (4.19) as the transverse momentum associated with jet j , so that a way to find the n hardest jets is by taking the n highest values of ω_{HT} . However, although the sum of the ω_{HT} returns \tilde{H}_T , $p_{T\text{cut}}$ would distort the jet p_T spectrum. The reason is that the $p_{T\text{cut}}$ requirement in Eqs. (4.16) and (4.17) vetoes particles near the periphery of jets which would be captured using standard clustering procedures. Note that this effect is relevant only for jets close to the $p_{T\text{cut}}$ threshold. This effect was not seen in Fig. 4-8 for $\tilde{p}_T(n)$ because there we could compensate for the loss of peripheral particles by using $n_{\text{off}} = 0.5$ in Eq. (4.12). This effect is visible, however, in Fig. 4-3a for H_T where the peaks in the event shape \tilde{H}_T (corresponding to

¹⁰To further reduce the number of jet directions, we could further insist that the winner-take-all axes are globally consistent. That is, if particle a has winner-take-all axis aligned with particle b , but particle b has winner-take-all axis aligned with particle c , then we could assign particle a the axis aligned with c (recursing further if necessary). This consistency criteria would ensure that the final set of jet directions $\{\hat{m}_j^r\}$ are their own winner-take-all axes. It would also imply that the jet regions can expand beyond a cone of radius R from the jet axes. This option is available in the FASTJET add-on, but not used in the following plots.

¹¹Unlike in the E -scheme, the jet axis and the jet four-momentum (i.e. the summed four-momenta of the jet constituents) will not typically be aligned in the winner-take-all scheme.

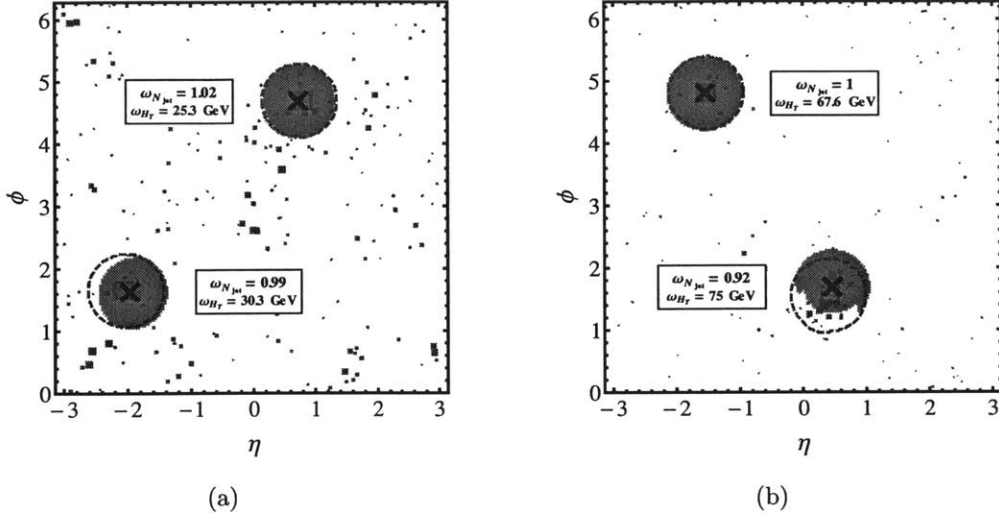


Figure 4-10: Two QCD dijet event displays with $R = 0.6$. The anti- k_T jet axes (green) are compared to the ones obtained using the hybrid event shape approach with $p_{T\text{cut}} = 0$ (blue). The standard E -scheme is used for the anti- k_T jets, whereas the hybrid event shape uses the winner-take-all recombination scheme, as explained in Sec. 4.2.2. The light blue shaded region corresponds to (passive) ghost particles which are clustered to the given axis, and the dashed green curve gives the anti- k_T boundary. The weights $\omega_{N_{\text{jet}}} \simeq 1$ and $\omega_{H_T} \simeq p_{T\text{jet}}$ associated with the event shape axes are also shown.

jets at threshold) are below the peaks for the jet-based H_T because of leakage towards smaller values of \tilde{H}_T . The most convenient way to restore the vetoed particles is to simply take $p_{T\text{cut}} = 0$ in Eq. (4.19), in which case the sum of the ω_{H_T} yields the total sum of scalar p_T in the event (though the sum of the $\omega_{N_{\text{jet}}}$ is no longer infrared safe).

We now compare standard jet clustering to the hybrid event shape approach. For anti- k_T jets, we use the standard E -scheme recombination, whereas for the hybrid event shape, we use the anti- k_T clustering measure with winner-take-all recombination for the local clustering around each particle. In Fig. 4-10 we show two QCD dijet events comparing the two hardest jets from anti- k_T with the jets defined by the two highest weights ω_{H_T} (with $p_{T\text{cut}} = 0$). We also show the corresponding values of $\omega_{N_{\text{jet}}}$ and ω_{H_T} . The displayed jet regions are determined by adding (passive) ghost particles [43]. There are differences between the jet axes caused by the different recombination schemes, and differences in the jet regions from the different effective jet splitting

criteria. But overall, there is a good correlation between the two methods, and the fact that $\omega_{N_{\text{jet}}} \simeq 1$ is a nice cross check.

Turning to the QCD dijet event sample, back in Fig. 4-8 we showed distributions for the three highest weights ω_{H_T} , which correlate strongly with the three hardest jets from anti- k_T (and with the inverse multiplicity $\tilde{p}_T(n)$). In Fig. 4-11, we compare the direction of the axis of the hardest jet found with both methods, again seeing good agreement, apart from a small set of events where the azimuth differs by π because the choice of hardest jet is ambiguous. In the three panels of Fig. 4-12, we show various effects on the hardest jet of having $p_{T\text{cut}} = 0$ versus non-zero $p_{T\text{cut}}$. The (passive) jet areas are shown in Fig. 4-12a, where the jet area distribution is peaked around πR^2 for $p_{T\text{cut}} = 0$ (similar to anti- k_T) whereas the area is smaller for non-zero $p_{T\text{cut}}$ because of peripheral vetoes. The same effect is seen in Fig. 4-12b, where a non-zero $p_{T\text{cut}}$ decreases the ω_{H_T} value. The effect is less visible for $\omega_{N_{\text{jet}}}$ in the Fig. 4-12c, since most events peak at 1, but there is a shift to lower $\omega_{N_{\text{jet}}}$ as $p_{T\text{cut}}$ is increased. We thus conclude that $p_{T\text{cut}} = 0$ gives results that are closer to the expectation from standard jet clustering.

In terms of computational cost, the hybrid event shape approach is significantly more costly than anti- k_T , since one has to effectively run a separate jet clustering procedure for each particle i to determine the direction $\hat{n}_{i,R}^r$. On a standard laptop, it is roughly a factor of four slower on dijet events. Despite the speed issue, this approach to identifying candidate jet regions might still be appropriate for trigger-level analyses because of the parallelizable and local nature of the hybrid event shapes. The winner-take-all recombination is crucial for this approach to work, since it ensures that only a small number of candidate jet axes are identified. It also has the nice feature that a given jet axis is guaranteed to align along one of the input particle directions.

4.3 Shape Trimming

Thus far, we have only discussed event shapes for observables built as a sum over all jets in an event. As discussed further in Sec. 4.4, the same basic strategy can

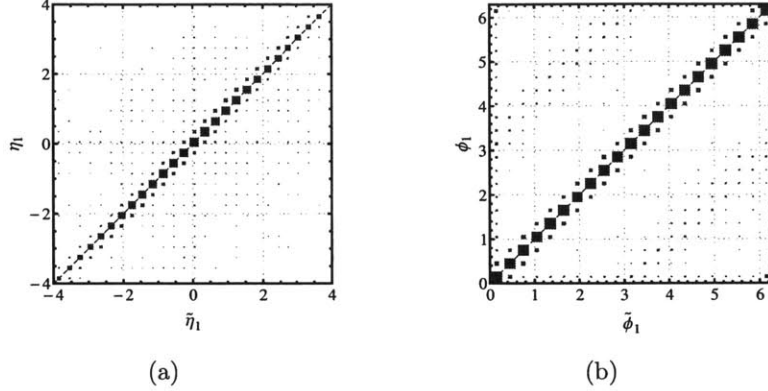


Figure 4-11: Position of the hardest jet axis for QCD dijet events, using the same jet clustering as Fig. 4-10. The (η_1, ϕ_1) coordinates correspond to the jet axis identified with anti- k_T , and $(\tilde{\eta}_1, \tilde{\phi}_1)$ are the coordinates found with the hybrid event shape. The area of the squares is proportional to the fraction of events in each bin. There is a slight difference in the jet direction due to the different recombination schemes (E -scheme for anti- k_T , winner-take-all for the hybrid event shape). Note the (small) accumulation of events at $|\phi_1 - \tilde{\phi}_1| = \pi$, which occur when the two algorithms disagree about which of the dijets is the hardest.

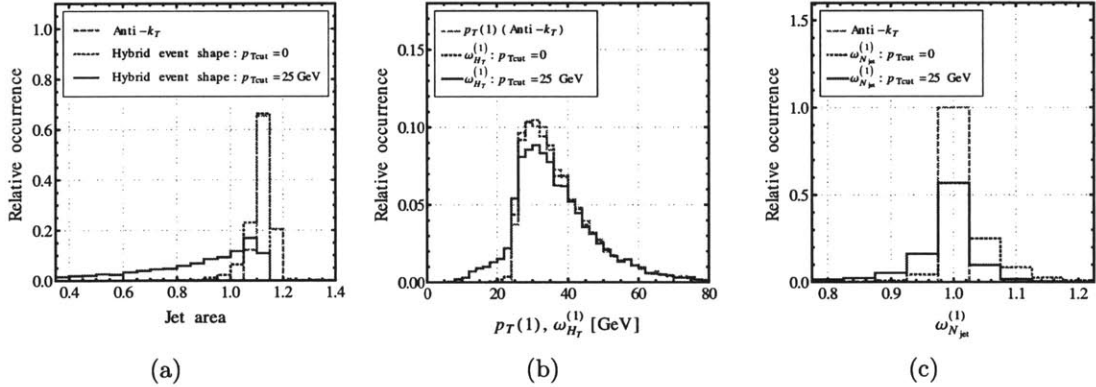


Figure 4-12: Comparison of the hardest jet found with anti- k_T (green dashed curve), the hybrid event shape result with $p_{T\text{cut}} = 0$ (blue dotted curve), and the hybrid event shape with $p_{T\text{cut}} = 25$ GeV (purple curve), all for QCD dijet events with $R = 0.6$. Left: Passive jet area, where the first two methods peak at πR^2 . Center: jet p_T (or ω_{H_T}). Right: fractional jet weight $\omega_{N_{\text{jet}}}$, where all methods peak at 1. In all cases, the $p_{T\text{cut}} = 0$ event shape is closer to the anti- k_T result, since it restores peripheral particles that are vetoed with non-zero $p_{T\text{cut}}$.

be applied to observables which are a sum over all subjets in all jets in an event. A simple application of this is to implement jet trimming [123] via an event shape. We refer to traditional jet trimming as “tree trimming” and the corresponding event shape version as “shape trimming”.

In tree trimming, one first clusters particles into jets of radius R and $p_{T\text{jet}} > p_{T\text{cut}}$, typically via the anti- k_T algorithm. For each jet, one reclusters its constituents into subjets with characteristic radius $R_{\text{sub}} < R$, typically via the CA algorithm [83, 166, 165] or k_T algorithm [47, 91]. Subjets whose transverse momentum fraction $p_{T\text{sub}}/p_{T\text{jet}}$ are above a certain threshold f_{cut} are kept, while the remaining subjets are removed. The four-momentum of a trimmed jet can be written as

$$t_{\text{jet}}^\mu = \sum_{\text{subjets}} p_{\text{sub}}^\mu \Theta \left(\frac{p_{T\text{sub}}}{p_{T\text{jet}}} - f_{\text{cut}} \right), \quad (4.21)$$

where p_{sub}^μ is the four-momentum of the subjet, $p_{T\text{sub}}$ is the corresponding transverse momentum, and $p_{T\text{jet}}$ is the transverse momentum of the un-trimmed jet. The trimmed four-momentum of the entire event is

$$t_{\text{event}}^\mu = \sum_{\text{jets}} t_{\text{jet}}^\mu \Theta(p_{T\text{jet}} - p_{T\text{cut}}) = \sum_{\text{jets}} \sum_{\text{subjets}} p_{\text{sub}}^\mu \Theta \left(\frac{p_{T\text{sub}}}{p_{T\text{jet}}} - f_{\text{cut}} \right) \Theta(p_{T\text{jet}} - p_{T\text{cut}}) \quad (4.22)$$

Along with the clustering algorithms used, the trimming procedure is specified by the jet parameters $\{p_{T\text{cut}}, R\}$ and the subjet parameters $\{f_{\text{cut}}, R_{\text{sub}}\}$.

To recast trimming as an event shape, we can follow the strategy outlined in Sec. 4.1, but adding an extra step to deal with the presence of subjets. Since $p_{\text{sub}}^\mu \simeq \sum_{i \in \text{subjet}} p_i^\mu$ can be written as a sum over subjet’s constituents, we can skip the first replacement in Eq. (4.5), and directly make the replacement

$$\sum_{\text{jets}} \sum_{\text{subjets}} p_{\text{sub}}^\mu \rightarrow \sum_{i \in \text{event}} p_i^\mu. \quad (4.23)$$

Moreover,

$$p_{T\text{jet}} \rightarrow p_{T i, R}, \quad p_{T\text{sub}} \rightarrow p_{T i, R_{\text{sub}}}, \quad (4.24)$$

where $p_{T i, R_{\text{sub}}}$ is analogous to $p_{T i, R}$ in Eq. (4.7), except it only includes particles contained in a cone around particle i of radius R_{sub} . The trimmed event shape corresponding to the overall four-momentum is therefore

$$\tilde{t}_{\text{event}}^\mu = \sum_{i \in \text{event}} p_i^\mu \Theta \left(\frac{p_{T i, R_{\text{sub}}}}{p_{T i, R}} - f_{\text{cut}} \right) \Theta(p_{T i, R} - p_{T\text{cut}}). \quad (4.25)$$

For defining more general event shapes (or for use in other jet-based analyses), we can interpret $\tilde{t}_{\text{event}}^\mu$ as defining a weight for each individual particle:

$$w_i = \Theta \left(\frac{p_{T i, R_{\text{sub}}}}{p_{T i, R}} - f_{\text{cut}} \right) \Theta(p_{T i, R} - p_{T\text{cut}}). \quad (4.26)$$

Here w_i is either 0 or 1, but one could generalize w_i to take on continuous values by smoothing out the theta functions. In practice, we implement Eq. (4.26) as a `Selector` in our `FASTJET` add-on, which takes a collection of particles and only returns those particles with $w_i = 1$. Instead of applying trimming event wide (“event shape trimming”), one could first find jets with an ordinary jet algorithm and then apply Eq. (4.26) with $p_{T i, R}$ replaced by $p_{T\text{jet}}$; we have implemented this “jet shape trimming” option as a `Transformer` in `FASTJET`.

One could also use the weights directly in the event shapes. For example, we could define the trimmed jet multiplicity as

$$\tilde{N}_{\text{jet}}^{\text{trim}}(p_{T\text{cut}}, R; f_{\text{cut}}, R_{\text{sub}}) = \sum_{i \in \text{event}} \frac{p_{T i}}{p_{T i, R}} \Theta \left(\frac{p_{T i, R_{\text{sub}}}}{p_{T i, R}} - f_{\text{cut}} \right) \Theta(p_{T i, R} - p_{T\text{cut}}), \quad (4.27)$$

and one could define the trimmed inverse $\tilde{p}_T^{\text{trim}}(n, R; f_{\text{cut}}, R_{\text{sub}})$ accordingly. Note that applying the weights in Eq. (4.26) first and then calculating \tilde{N}_{jet} is not the same as calculating $\tilde{N}_{\text{jet}}^{\text{trim}}$ directly, since in the former case, the value of $p_{T i, R}$ is affected by the weights. In most cases, one gets better performance by using the weights first,

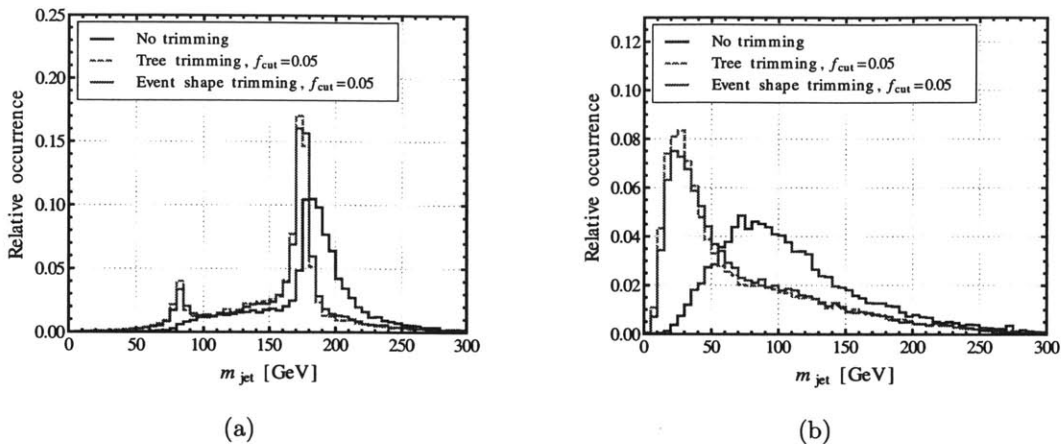


Figure 4-13: Boosted top sample (left) and corresponding QCD background (right) from the BOOST 2010 event samples [14]. For ordinary tree trimming, we identify jets anti- k_T jets with $R = 1.0$ and $p_{T\text{cut}} = 200$ GeV, and then applying trimming with $R_{\text{sub}} = 0.3$ and $f_{\text{cut}} = 0.05$. For shape trimming, we apply event-wide trimming using the same R_{sub} and f_{cut} parameter before clustering with anti- k_T . In both cases, we plot the masses of the two hardest jets per event.

especially if the jet observable \mathcal{F}_{jet} is non-linear in the inputs (as is the case for jet mass studied in Sec. 4.4.1). For $\tilde{N}_{\text{jet}}^{\text{trim}}$ there is only a mild difference, so we use $\tilde{N}_{\text{jet}}^{\text{trim}}$ for simplicity in some of the case studies in Sec. 4.4.

To compare the behavior of ordinary tree trimming and shape trimming, we use event samples from the BOOST 2010 report [14]. In particular, we analyze a boosted top signal and the corresponding QCD background in the p_T bin $500 \text{ GeV} < p_T < 600 \text{ GeV}$.¹² In Fig. 4-13, we show the effect of trimming on the jet mass spectrum for the boosted top signal and the corresponding QCD background. For tree trimming, we build anti- k_T jets with $R = 1.0$ and $p_{T\text{cut}} = 200$ GeV and trim with $R_{\text{sub}} = 0.3$ and $f_{\text{cut}} = 0.05$. For shape trimming, we use the same set of parameters to trim the entire event according to weights from Eq. (4.26), and then build anti- k_T jets with $R = 1.0$ and $p_{T\text{cut}} = 200$ GeV. We see that the behavior of both trimming methods is very similar, and that both methods emphasize the boosted top mass peak while

¹²Event samples from BOOST 2010 and details about events generation can be found at <http://www.lpthe.jussieu.fr/~salam/projects/boost2010-events/herwig65> and <http://tev4.phys.washington.edu/TeraScale/boost2010/herwig65>. These events are for the 7 TeV LHC generated with HERWIG 6.510 [66], with underlying event given by JIMMY [39] with an ATLAS tune [157].

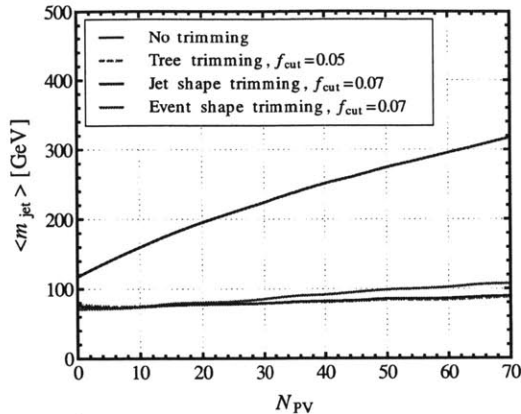


Figure 4-14: Pileup mitigation for $Z(\rightarrow \nu\nu) + j$ events. Shown is the mean of the hardest jet mass distribution as a function of the number of primary vertices N_{PV} . In all cases we use $R_{\text{sub}} = 0.3$, with $f_{\text{cut}} = 0.05$ for tree-trimming and $f_{\text{cut}} = 0.07$ for the two shape trimming options.

suppressing the high-mass QCD background. Jet shape trimming is not shown in Fig. 4-13 as it performs very similarly to event shape trimming.

One important application for trimming is pileup mitigation [52, 10]. To study its effectiveness, we take our sample of $Z(\rightarrow \nu\nu) + j$ events from Sec. 4.1 and overlay N_{PV} soft QCD events generated with PYTHIA 8.157 [150].¹³ We consider three options: ordinary tree trimming, shape trimming applied to the individual jets (jet shape trimming), and shape trimming applied to the entire event (event shape trimming). Fig. 4-14 shows the average of the hardest jet mass as a function of N_{PV} , where the jets are built using anti- k_T with $R = 1.0$ and $p_{T\text{cut}} = 500$ GeV. Taking $R_{\text{sub}} = 0.3$ in all cases, we find a comparable degree of stability against pileup for tree trimming with $f_{\text{cut}} = 0.05$ (as was done in Ref. [10]), jet shape trimming with $f_{\text{cut}} = 0.07$, and event shape trimming with $f_{\text{cut}} = 0.07$. Note that event shape trimming has the largest variation with N_{PV} , as expected since $p_{T_{i,R}}$ is typically lower than $p_{T_{\text{jet}}}$, and therefore does not groom as aggressively. Part of the reason we need a different f_{cut} value for tree trimming versus shape trimming is that the effective subjet areas of the two methods are different.

¹³Here, the minimum p_T for the hard process at generator level has been reset to $p_{T\text{cut}}^{\text{parton}} = 350$ GeV.

A complementary way to do pileup mitigation is via area subtraction [41, 43, 151]. It is straightforward to correct the trimming weights in Eq. (4.26) using area subtraction, because $p_{T_i, R_{\text{sub}}}$ and $p_{T_i, R}$ are defined in terms of fixed-radius regions, and therefore have fixed areas πR_{sub}^2 and πR^2 respectively. At present, our FASTJET implementation of shape trimming does not include area subtraction, but we anticipate including that functionality in a future version.

4.4 Generalizations

4.4.1 Other Jet-like Event Shapes

The general procedure to build event shapes $\tilde{\mathcal{F}}$ from single jet observables \mathcal{F}_{jet} was given in Sec. 4.1. Here we give a few more examples beyond \tilde{N}_{jet} , \tilde{H}_T , and \tilde{p}_T .

As a simple generalization of N_{jet} and H_T , consider the jet-based observable

$$H_T^n(p_{T\text{cut}}, R) = \sum_{\text{jets}} p_{T\text{jet}}^n \Theta(p_{T\text{jet}} - p_{T\text{cut}}), \quad (4.28)$$

where $n = 0$ ($n = 1$) corresponds to N_{jet} (H_T). Using the method in Sec. 4.1, the corresponding event shape is

$$\tilde{H}_T^n(p_{T\text{cut}}, R) = \sum_{i \in \text{event}} \frac{p_{T,i}}{p_{T_i,R}} (p_{T_i,R})^n \Theta(p_{T_i,R} - p_{T\text{cut}}). \quad (4.29)$$

In Fig. 4-15, we compare $H_T^n(p_{T\text{cut}}, R)$ to $\tilde{H}_T^n(p_{T\text{cut}}, R)$ for $n = -1$ in QCD dijet events, using the same event generation scheme as Sec. 4.1.

A more complicated example is the sum of jet masses in an event,

$$M_J(p_{T\text{cut}}, R) = \sum_{\text{jets}} m_{\text{jet}} \Theta(p_{T\text{jet}} - p_{T\text{cut}}). \quad (4.30)$$

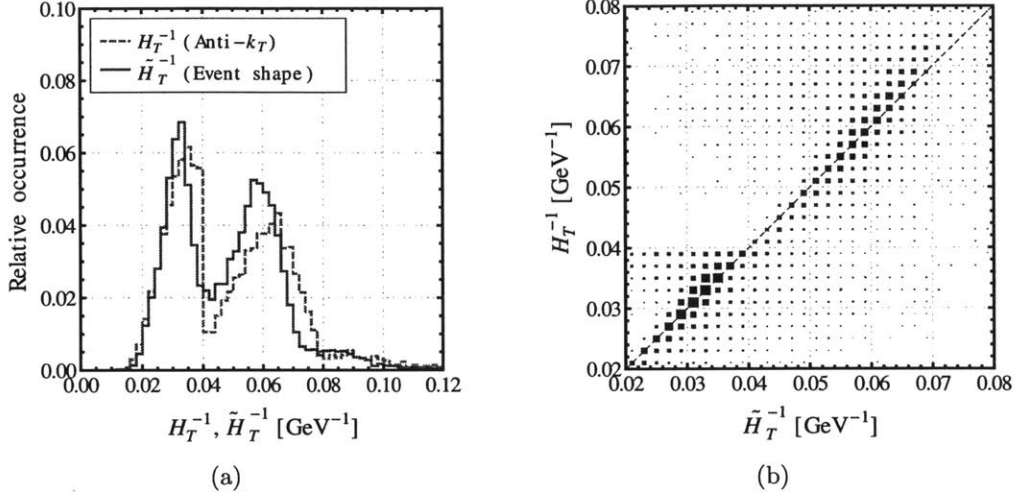


Figure 4-15: Summed transverse momentum inverse (i.e. H_T^n with $n = -1$) for QCD dijet events. The jet parameters, formatting, and cuts are the same as for Fig. 4-2.

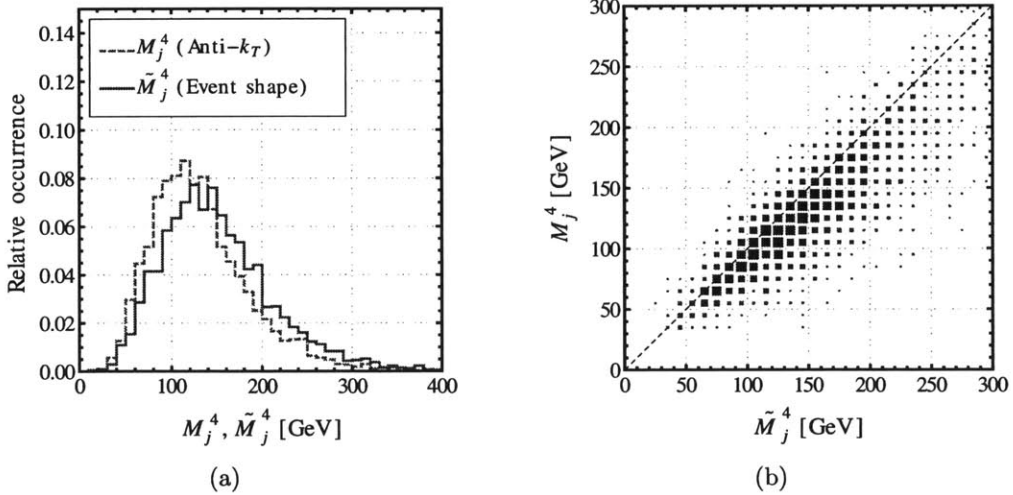


Figure 4-16: Summed jet mass analysis for M_j^4 that mimics Ref. [85]. Shown is a QCD four-jet sample with the (trimmed) summed jet mass of the four hardest jets. For the anti- k_T version, the trimmed jets have $R = 1.2$, $p_{T\text{cut}} = 50$ GeV, $R_{\text{sub}} = 0.3$, and $f_{\text{cut}} = 0.05$, requiring at least four such jets and the hardest jet above 100 GeV. For the event shape version, the event selection criteria is $\tilde{N}_{\text{jet}}^{\text{trim}} > 3.5$ and $\tilde{p}_T^{\text{trim}}(1) > 100$ GeV with the same jet and trimming parameters above, and the observable is \tilde{M}_j^4 defined in Eq. (4.32), calculated after the trimming weights in Eq. (4.26) are applied.

The corresponding event shape is given by

$$\widetilde{M}_J(p_{T\text{cut}}, R) = \sum_{i \in \text{Event}} \frac{p_{T,i}}{p_{T,i,R}} m_{i,R} \Theta(p_{T,i,R} - p_{T\text{cut}}), \quad (4.31)$$

where $m_{i,R} = \sqrt{|p_{i,R}^\mu|^2}$. One could of course raise $m_{i,R}$ to a power in analogy with \widetilde{H}_T^n .

Summed jet mass is a potentially powerful variable to study high jet multiplicity events at the LHC [114], and can be combined with other substructure observables to control QCD multijet backgrounds to new physics searches [61, 85]. As an example, it is instructive to see how to mimic aspects of such an analysis using event shapes. In Ref. [85], events were clustered into fat jets with $R = 1.2$, the fat jets were trimmed ($R_{\text{sub}} = 0.3$, $f_{\text{cut}} = 0.05$), and events were retained if they had at least four fat jets above $p_{T\text{cut}} = 50$ GeV and the hardest jet above 100 GeV. Then the (trimmed) summed jet mass was taken for just the four hardest jets. To mimic the selection procedure, one would take events with $\widetilde{N}_{\text{jet}}^{\text{trim}}(p_{T\text{cut}}, R; f_{\text{cut}}, R_{\text{sub}}) > 3.5$ (see Eq. (4.27)) and $\widetilde{p}_T^{\text{trim}}(1) > 100$ GeV. To mimic the observable, one would first apply the shape trimming weights from Eq. (4.26), and then define

$$\widetilde{M}_J^4(p_{T\text{cut}}, R) \equiv M_J(p'_{T\text{cut}}, R), \quad p'_{T\text{cut}} = \max\{p_{T\text{cut}}, \widetilde{p}_T^{\text{trim}}(5)\}, \quad (4.32)$$

where $p'_{T\text{cut}}$ effectively picks out the four hardest jets (see Eq. (4.13)). In Fig. 4-16, we compare the distributions of the (trimmed) summed mass calculated using the two different methods on a QCD four-jet sample. Despite the somewhat complicated form of the event shape version, there are clear correlations between the methods. We will discuss the subjet counting aspect of Ref. [85] in Sec. 4.4.3.¹⁴

¹⁴The event-subjettiness variable of Ref. [61] is defined as a geometric mean of N -subjettiness ratios [155, 156] measured on individual jets. To convert that to an event shape, we would first take the logarithm, since that would correspond to a sum over the logs of individual jet observables, and is therefore in the form needed in Eq. (4.4).

4.4.2 Subjet-like Jet Shapes

Thus far, we have focused on jet-like event shapes, but it is clear that the same technique can be applied to subjet-like jet shapes. These jet shapes would probe the substructure of a given jet, and can be defined according to Eqs. (4.4) and (4.8) with “jet” replaced by “subjet” and “event” replaced by “jet”. Concretely, given a jet found using an ordinary jet algorithm, consider a subjet-based observable built from subjets of radius R_{sub} above $p_{T\text{subcut}}$:

$$\mathcal{G}(p_{T\text{subcut}}, R_{\text{sub}}) = \sum_{\text{subjets}} \mathcal{G}_{\text{subjet}} \Theta(p_{T\text{sub}} - p_{T\text{subcut}}), \quad (4.33)$$

where $\mathcal{G}_{\text{subjet}} \equiv g(\{p_j^\mu\}_{j \in \text{subjet}})$ depends on the kinematics of the individual subjet constituents. The corresponding jet shape would be

$$\tilde{\mathcal{G}}(p_{T\text{cut}}, R_{\text{sub}}) = \sum_{i \in \text{jet}} \frac{p_{Ti}}{p_{Ti, R_{\text{sub}}}} \mathcal{G}_{i, R_{\text{sub}}} \Theta(p_{Ti, R_{\text{sub}}} - p_{T\text{subcut}}), \quad (4.34)$$

where $\mathcal{G}_{i, R_{\text{sub}}} \equiv g(\{p_j^\mu \Theta(R_{\text{sub}} - \Delta R_{ij})\}_{j \in \text{jet}})$.

As an example, a jet shape that counts the subjet multiplicity is

$$\tilde{N}_{\text{subjet}}(p_{T\text{subcut}}, R_{\text{sub}}) = \sum_{i \in \text{jet}} \frac{p_{Ti}}{p_{Ti, R_{\text{sub}}}} \Theta(p_{Ti, R_{\text{sub}}} - p_{T\text{subcut}}). \quad (4.35)$$

In Fig. 4-17 we study subjet multiplicity for the same boosted top sample analyzed in Sec. 4.3. Starting from anti- k_T jets with $R = 1.0$ and $p_{T\text{cut}} = 200$ GeV, we count the number of subjets in three different ways. First, we count the number of Cambridge-Aachen subjets left after trimming is applied with $R_{\text{sub}} = 0.3$ and $f_{\text{cut}} = 0.05$. Second, we re-run anti- k_T clustering on the jet with $R_{\text{sub}} = 0.3$ and $p_{T\text{subcut}} = f_{\text{cut}} p_{T\text{jet}}$. Third, we use the jet shape $\tilde{N}_{\text{subjet}}$ with the same value of R_{sub} and $p_{T\text{subcut}}$. The first two methods necessarily yield integer values, whereas $\tilde{N}_{\text{subjet}}$ is continuous. All three methods peak at $N_{\text{subjet}} = 3$, as expected since this is a boosted top quark sample.

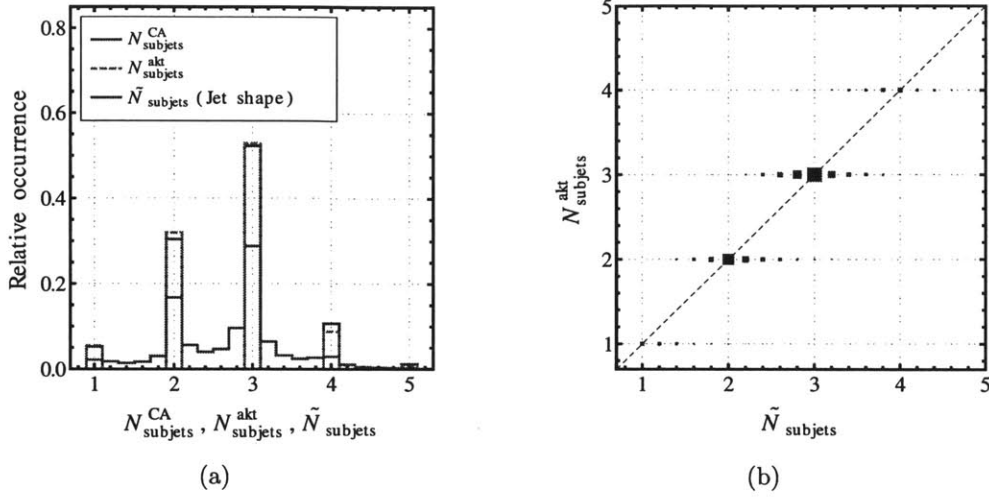


Figure 4-17: Subject multiplicity (i.e. N_{subject}) on the boosted top sample from BOOST 2010. The jet selection is the same as in Fig. 4-13, and we count subjects either with Cambridge-Aachen clustering, anti- k_T clustering, or $\tilde{N}_{\text{subject}}$. In all cases, we take $R_{\text{sub}} = 0.3$ and $p_{T\text{subcut}} = 0.05 p_{T\text{jet}}$. In the case of Cambridge-Aachen clustering, this is equivalent to counting the subjects left from (CA) trimming with $R_{\text{sub}} = 0.3$ and $f_{\text{cut}} = 0.05$.

4.4.3 Subject-like Event Shapes

Our final generalization is to observables that are inclusive over the subjects in an entire event. That is, we want to start from an observable defined in terms of the constituents in a subject, summed over all subjects in each jet, and then further summed over all jets in the event. Consider an observable built from jets of radius R above $p_{T\text{cut}}$ with subjects of radius R_{sub} above $p_{T\text{subcut}}$:

$$\mathcal{H}(p_{T\text{cut}}, R_{\text{sub}}; p_{T\text{subcut}}, R_{\text{sub}}) = \sum_{\text{jets}} \sum_{\text{subjects}} \mathcal{H}_{\text{subject}} \Theta(p_{T\text{sub}} - p_{T\text{subcut}}) \Theta(p_{T\text{jet}} - p_{T\text{cut}}) \quad (4.36)$$

where $\mathcal{H}_{\text{subject}} \equiv h(\{p_j^\mu\}_{j \in \text{subject}})$ depends on the kinematics of the subject constituents.

The corresponding event shape is

$$\tilde{\mathcal{H}}(p_{T\text{cut}}, R; p_{T\text{subcut}}, R_{\text{sub}}) = \sum_{i \in \text{event}} \frac{p_{Ti}}{p_{Ti, R_{\text{sub}}}} \mathcal{H}_{i, R_{\text{sub}}} \Theta(p_{Ti, R_{\text{sub}}} - p_{T\text{subcut}}) \Theta(p_{Ti, R} - p_{T\text{cut}}) \quad (4.37)$$

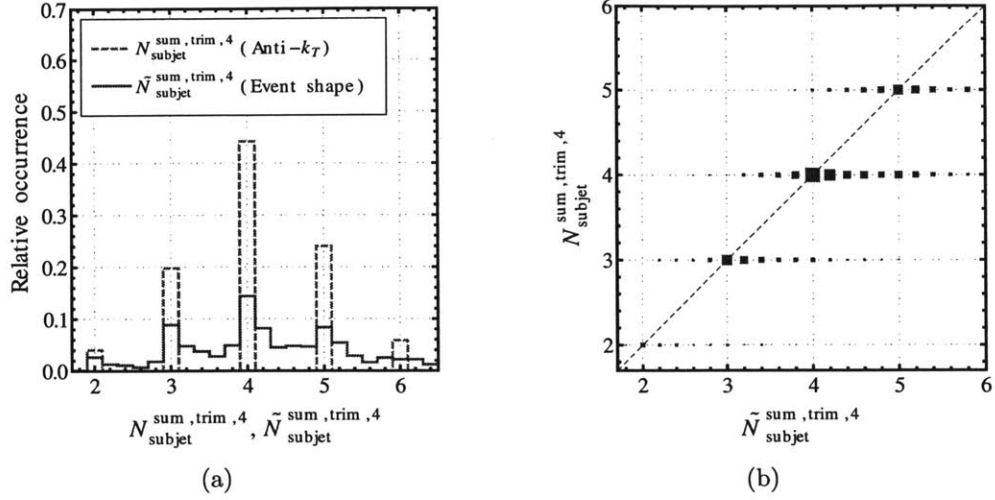


Figure 4-18: Summed subjet multiplicity (i.e. $N_{\text{subjet}}^{\text{sum}}$) on a QCD four-jet sample, in the spirit of Ref. [85]. The jet selection is the same as Fig. 4-16, and we use the event shape $\tilde{N}_{\text{subjet}}^{\text{sum,trim,4}}$ from Eq. (4.41).

where $\mathcal{H}_{i,R_{\text{sub}}} \equiv h(\{p_j^\mu \Theta(R_{\text{sub}} - \Delta R_{ij})\}_{j \in \text{event}})$. Note that the weight factor depends on $p_{T_i,R_{\text{sub}}}$, and $p_{T_i,R}$ only appears for testing $p_{T_{\text{cut}}}$.

For measurement functions $\mathcal{H}_{\text{subjet}}$ that are expressible as a sums over the subjet constituents,

$$\mathcal{H}_{\text{subjet}} = \sum_{j \in \text{subjet}} \tilde{h}(p_j^\mu), \quad (4.38)$$

where \tilde{h} is a single particle measurement function, we can elide the $p_{T_i}/p_{T_i,R_{\text{sub}}}$ weighting factor and directly write down the event shape

$$\tilde{\mathcal{H}}(p_{T_{\text{cut}}}, R; p_{T_{\text{subcut}}}, R_{\text{sub}}) = \sum_{i \in \text{event}} \tilde{h}(p_i^\mu) \Theta(p_{T_i,R_{\text{sub}}} - p_{T_{\text{subcut}}}) \Theta(p_{T_i,R} - p_{T_{\text{cut}}}). \quad (4.39)$$

The shape trimming technique from Sec. 4.3 can be expressed as such an event shape, with $p_{T_{\text{subcut}}} = f_{\text{cut}} p_{T_i,R}$ and $\tilde{h}(p_j^\mu) = p_j^\mu$ (see Eq. (4.25)).

Following the example of subjet multiplicity $\tilde{N}_{\text{subjet}}$ in Eq. (4.35), we can define

the (trimmed) summed subjet multiplicity:

$$\begin{aligned} \tilde{N}_{\text{subjet}}^{\text{sum,trim}}(p_{T\text{cut}}, R; f_{\text{cut}}, p_{T\text{subcut}}, R_{\text{sub}}) & \quad (4.40) \\ &= \sum_{i \in \text{event}} \frac{p_{Ti}}{p_{Ti, R_{\text{sub}}}} \Theta(p_{Ti, R_{\text{sub}}} - p_{T\text{subcut}}) \Theta\left(\frac{p_{Ti, R_{\text{sub}}}}{p_{Ti, R}} - f_{\text{cut}}\right) \Theta(p_{Ti, R} - p_{T\text{cut}}), \end{aligned}$$

where the trimming criteria on the subjets is only imposed if it is stricter than the $p_{T\text{subcut}}$ requirement. A similar variable was used in Ref. [85] to isolate high jet multiplicity events at the LHC, in concert with the summed jet mass already mentioned in Sec. 4.4.1. Here, however, we are restricted to defining subjets with a fixed radius R_{sub} , as opposed to the more dynamical subjet finding procedures advocated in Ref. [85].¹⁵ In Fig. 4-18, we compare subjet counting using anti- k_T for both fat jets and subjets to the comparable procedure with $\tilde{N}_{\text{subjet}}^{\text{sum}}$ on the QCD four-jet sample. We use the same event selection as in Sec. 4.4.1, and define

$$\tilde{N}_{\text{subjet}}^{\text{sum,trim,4}}(p_{T\text{cut}}, R; f_{\text{cut}}, p_{T\text{subcut}}, R_{\text{sub}}) = \tilde{N}_{\text{subjet}}^{\text{sum,trim}}(p'_{T\text{cut}}, R; f_{\text{cut}}, p_{T\text{subcut}}, R_{\text{sub}}) \quad (4.41)$$

with $p'_{T\text{cut}} = \max\{p_{T\text{cut}}, \tilde{p}_T^{\text{trim}}(5)\}$ to effectively isolate the four hardest jets. Apart from the non-integer nature of $\tilde{N}_{\text{subjet}}^{\text{sum,trim,4}}$, there is a clear correlation between the methods.

4.5 Conclusions

We have shown how inclusive jet observables can be recast as jet-like event shapes. By replacing an inclusive sum over jets in an event with an inclusive sum over particles in an event, we have removed the dependence on the jet clustering procedure, while still maintaining the jet-like radius R and jet-like momentum cut $p_{T\text{cut}}$ expected in jet-based analyses. While our original method can only be applied to inclusive jet observables, we have shown one example where more exclusive information about single jets was obtained by inverting the jet multiplicity event shape \tilde{N}_{jet} to determine

¹⁵In principle, one could choose the subjet radius R_{sub} to be a (local) function of the particles within a radius R of particle i .

the p_T of the n -th hardest jet. Our focus was on event shapes, though we have shown that there is a straightforward generalization to jet shapes, which may find use in jet substructure studies.

A promising possible application of these event shapes is for event selection at the trigger level, especially given their local computational structure. To the best of our knowledge, all jet triggers presently in use on the ATLAS and CMS experiments can be mimicked by appropriate combinations of \tilde{N}_{jet} , \tilde{H}_T , and \tilde{p}_T cuts (choosing different values of R and $p_{T\text{cut}}$ as needed). It may even be possible to do preliminary jet identification at the trigger level using the hybrid event shapes with winner-take-all recombination; the local nature of the clustering means that the approach can be parallelized across the detector without double-counting. Of course, more detailed feasibility studies are needed to see whether these event shapes can be incorporated into the trigger upgrades planned for high-luminosity LHC running.

For analysis-level jet studies, the event shapes provide a complementary characterization of the gross jet-like nature of the event. From the correlations seen in Sec. 4.1, one should expect \mathcal{F} and $\tilde{\mathcal{F}}$ to have similar performance in an experimental context. There can be important differences, however, in regions of phase space where jets are overlapping or otherwise ambiguous. Thus, a comparison between, say, a selection criteria based on N_{jet} and one based on \tilde{N}_{jet} would offer a useful test for the robustness of an analysis.

A novel application of our method is for jet grooming via shape trimming. This worked because ordinary tree trimming [123] can be written as a double sum over subjets and jets in an event, allowing an application of the general techniques in Sec. 4.4.3. Shape trimming can be applied to event shapes themselves, or it can be interpreted as simply assigning a weight to each particle in an event, after which one can perform a traditional jet-based analysis. Shape trimming has similar pileup mitigation performance to tree trimming, but can be more easily applied event-wide since it does not require the explicit identification of jets or subjets.

Other grooming techniques beyond trimming deserve future study, though we do not know (yet) how to cast them as event shapes. For example, filtering [40] is based

on keeping a fixed number of subjets, which we do not know how to implement as an inclusive sum over all particles in an event. Similarly, pruning [92, 93] and (modified) mass drop [40, 73, 72] are based on recursively applying a selection criteria, which have no obvious event shape counterpart. The modified mass drop procedure is particularly interesting because it removes Sudakov double logarithms [73, 72], and a non-recursive event shape version of this procedure would help for understanding this unique behavior.

Finally, these event shapes are particularly interesting for future analytic studies in perturbative QCD. Formally, an inclusive jet observable \mathcal{F} and its event shape counterpart $\tilde{\mathcal{F}}$ are exactly equivalent for infinitely narrow jets separated by more than R , such that they share the same soft-collinear structure. Therefore, up to non-singular and power-suppressed terms, we expect \mathcal{F} and $\tilde{\mathcal{F}}$ to have similar (if not identical) factorization and resummation properties. That said, there is clearly a difference between the integer-valued jet multiplicity N_{jet} and the continuous event shape \tilde{N}_{jet} , though the difference does not show up until $\mathcal{O}(\alpha_s)$ (for jets separated by more than R but less than $2R$) or $\mathcal{O}(\alpha_s^2)$ (for jets separated by more than $2R$). We expect that understanding the origin of non-integer \tilde{N}_{jet} values is likely to shed considerable light on the jet-like nature of QCD.

Chapter 5

Conclusions

The discovery of the Higgs boson represents a historic event in particle physics. The spontaneous breaking of the electroweak symmetry seems to be caused by a weakly coupled elementary scalar. This is the first time we observe a system in Nature that exhibits this property. Further data will allow to establish accurately the Higgs boson properties and investigate possible deviations from SM predictions. The exploration of the electroweak scale undergoing at the LHC will allow to fully unveil the mechanism responsible for the electroweak symmetry breaking, and possibly to detect signals of new physics. On one hand, new physics in the Higgs sector has been long expected because of the naturalness problem. On the other hand, even if one abandons the naturalness argument, the Higgs sector might act as a portal towards unknown sectors, possibly related to dark matter and baryogenesis. In the first part of this thesis we analyzed electroweak symmetry breaking from two different perspectives.

In Chapter 2 we adopted a “top-down” approach. We investigated how supersymmetry breaking can be linked to electroweak symmetry breaking. In particular, the dynamics of the Higgs sector in the supersymmetric standard model can contribute to supersymmetry breaking. A general consequence is a light pseudo-goldstino in the spectrum of the theory. If the mediation preserves an R -symmetry, stringent cosmological bounds can be evaded, and we investigated the consequences of this light state for collider phenomenology. We demonstrated how Higgs and neutralino decays can be potentially altered from standard supersymmetric predictions.

In Chapter 3 we took instead a “bottom-up” approach. Starting from measurements of the Higgs couplings performed by ATLAS and CMS and using exclusion limits for Higgs-like states set at higher masses we constrained simplified extensions of the SM Higgs sector. In particular, we considered the mixing of the SM Higgs with a gauge singlet, which has possibly enhanced couplings to photons. Although simplified, we believe those models map onto theoretically motivated extensions of the SM, such as the NMSSM. The data show no statistically significant preference for those models over the SM, and the mixing angle can be strongly constrained.

A second part of this thesis is developed in Chapter 4. Here, we focused on QCD. We proposed a new definition of jets, that is based on event shapes and local properties of the event around each particle, and does not require any clustering. We showed how conventional inclusive jet-based observables can be recovered within this new approach, and how subjet-based techniques, such as trimming, can also be recast in this form. We also showed how more exclusive information, such as individual jet four-momenta can be defined using “hybrid event shapes”. We discussed potential applications of this framework both at trigger and analysis level. Finally, we anticipated that an understanding of the fractional jet multiplicity defined in our approach, might reveal interesting properties of QCD.

The development of new approaches for analyzing hadronic final states at colliders has a double relevance. On one side, it is crucial for our search of new physics, as we need increasingly more powerful tools to dig out possibly rare signals from backgrounds, especially in conditions of high energy and high luminosity. The newborn and extremely active field of jet substructure testifies to the relevance of this aspect. On the other side, the need of a theoretical understanding of jet and jet substructure physics stimulated a *renaissance* of QCD physics, with the goal of improving our understanding of its behavior, especially in regimes where standard perturbative approaches cannot be used.

Understanding electroweak symmetry breaking is a major goal of particle physics today. The next decade will be crucial, with the outcomes of the next LHC runs reshaping, in any case, the future of the field.

Appendix A

One-Loop Pseudo-Goldstino Mass

In this appendix, we calculate the pseudo-goldstino mass at one loop, which gives large corrections to the tree-level mass in Eq. (2.20). In the mass eigenstate basis, the tree-level neutralino Lagrangian is:

$$\mathcal{L}_\chi = i\bar{\chi}^0\bar{\sigma}^\mu\partial_\mu\chi^0 - \left(\frac{1}{2}(\chi^0)^T\mathcal{M}_D\chi^0 + \text{h.c.}\right) + \mathcal{L}_{\text{int}}(\chi^0, \dots), \quad (\text{A.1})$$

where \mathcal{M}_D is the diagonal mass matrix. The one-loop correction to the quadratic Lagrangian can be written as:

$$\delta\mathcal{L}_\chi^{(2)} = i\bar{\chi}^0\widehat{\Xi}\bar{\sigma}^\mu\partial_\mu\chi^0 - \left(\frac{1}{2}(\chi^0)^T\widehat{\Omega}\chi^0 + \text{h.c.}\right), \quad (\text{A.2})$$

where $\widehat{\Xi}$ and $\widehat{\Omega}$ are properly renormalized self-energy functions. Using Eq. (A.2), the one-loop corrected pseudo-goldstino mass is

$$m_\zeta = (1 - \widehat{\Xi}_{\zeta,\zeta})m_\zeta^{\text{tree}} + \widehat{\Omega}_{\zeta,\zeta}. \quad (\text{A.3})$$

The tree-level mass m_ζ^{tree} in Eq. (2.20) already captures the leading contribution from gauge interactions (remember that at tree-level the pseudo-goldstino can get mass *only* through gauge interactions), so at leading order we can ignore corrections coming from $\widehat{\Xi}_{\zeta,\zeta}$. On the other hand, $\widehat{\Omega}_{\zeta,\zeta}$ is necessary to capture the leading contribution

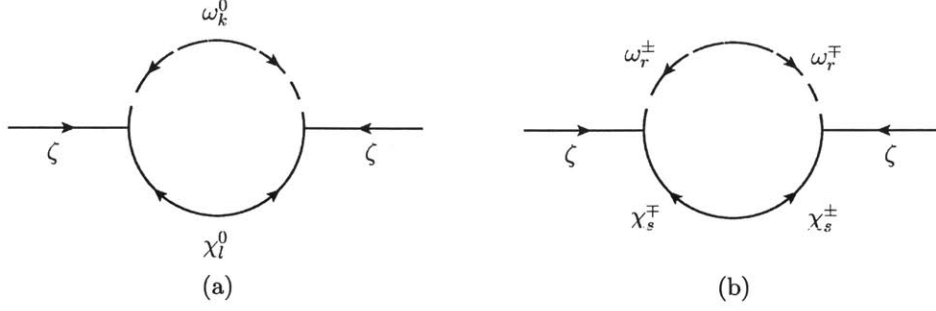


Figure A-1: One-loop self-energy diagrams contributing to the pseudo-goldstino mass.

in λ , such that

$$m_\zeta \simeq m_\zeta^{\text{tree}} + \widehat{\Omega}_{\zeta,\zeta}. \quad (\text{A.4})$$

The $\lambda X H_u H_d$ term in Eq. (2.1) contains the following interactions:

$$\mathcal{L} \supset \lambda \left(-\mathcal{Z}^{k\ell} \omega_k^0 \chi_\ell^0 + \mathcal{Y}^{rs} \omega_r^+ \chi_s^- + \mathcal{J}^{rs} \omega_r^- \chi_s^+ \right) \zeta + \text{h.c.}, \quad (\text{A.5})$$

where ω_k^0 and ω_r^\pm are the neutral and charged scalar mass eigenstates (including Goldstone bosons), and χ_ℓ^0 and χ_s^\pm are the neutralino and chargino mass eigenstates. The matrices \mathcal{Z} , \mathcal{Y} , and \mathcal{J} encode the appropriate mixing angles between gauge and mass eigenstates. The one-loop Feynman diagrams generated by Eq. (A.5) and contributing to the bare self-energy $\Omega_{\zeta,\zeta}$ are shown in Fig. A-1.¹

Because the theory has an underlying SUSY, UV divergences cancel in the sum over the states running in the loop, so at one loop the bare quantity $\Omega_{\zeta,\zeta}$ is finite and $\widehat{\Omega}_{\zeta,\zeta} \equiv \Omega_{\zeta,\zeta}$. The self-energy correction is

$$\widehat{\Omega}_{\zeta,\zeta}(p^2) = \frac{\lambda^2}{16\pi^2} \left(\sum_{k,\ell} (\mathcal{Z}^{k\ell})^2 m_l B(p^2; m_\ell^2, \mu_k^2) + 2 \sum_{r,s} \mathcal{Y}^{rs} \mathcal{J}^{rs} m_s B(p^2; m_s^2, \mu_r^2) \right), \quad (\text{A.6})$$

where m_ℓ , m_s , μ_k , and μ_r are the neutralino, chargino, neutral scalar, and charged scalar masses respectively, and p is the external momentum. The finite part of the

¹The one-loop corrections to the scalar potential will move the minimum from its tree-level position, generating tadpole diagrams that might contribute to Ω . However, if we neglect gauge interactions, there is no $\zeta\zeta\omega^0$ coupling and tadpoles do not contribute to Ω .

(one loop) Passarino-Veltman function is

$$B(p^2; x, y) = - \int_0^1 dt \log \left[\frac{tx + (1-t)y - t(1-t)p^2}{Q^2} \right], \quad (\text{A.7})$$

where the renormalization group scale Q^2 cancels in Eq. (A.6). Strictly speaking, $\widehat{\Omega}_{\zeta, \zeta}(p^2)$ should be evaluated at $\sqrt{p^2} = m_\zeta$ when used in Eq. (A.4), but since the self-energy is already $\mathcal{O}(\lambda^2)$, we can safely evaluate it at the tree-level mass $\sqrt{p^2} = m_\zeta^{\text{tree}} \approx 0$.

Appendix B

Dominant Pseudo-Goldstino Annihilation Channel

In this appendix, we confirm the statement in Sec. 2.3 that the pseudo-goldstino is a hot relic. At temperatures above the Higgs mass, the pseudo-goldstino has unsuppressed interactions with Higgs bosons and higgsinos. Therefore, the pseudo-goldstino achieves thermal equilibrium with the SSM for high enough reheat temperature. However, the interaction cross section drops rapidly for temperatures below the Higgs mass, and the freezeout temperature of the pseudo-goldstino is roughly the same as the freezeout temperature of the higgsino.

To see this, note that at temperatures below the Higgs mass, the dominant coupling of the pseudo-goldstino to light SM fields is Higgs exchange, shown in Fig. B-1.

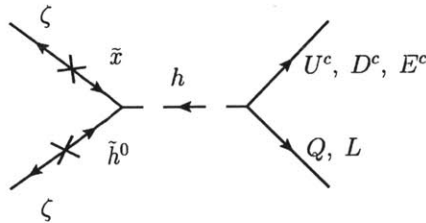


Figure B-1: The pseudo-goldstino can annihilate through its higgsino component to SM quarks and leptons. However, this cross section is very small, and the pseudo-goldstino is a cosmologically dangerous hot relic.

We can estimate this cross-section as

$$\begin{aligned}\sigma v &\approx \sum_f \Theta_{h^0, \zeta}^2 \lambda^2 y_f^2 \frac{(m_\zeta v)^2}{m_{h^0}^4} \left(1 - \frac{4m_f^2}{s}\right)^{3/2} \\ &\approx (10^{-14} \text{ pb}) v^2 \left(\frac{\lambda}{1.0}\right)^2 \left(\frac{y_f}{10^{-3}}\right)^2 \left(\frac{\Theta_{h^0, \zeta}}{10^{-3}}\right)^2 \left(\frac{120 \text{ GeV}}{m_{h^0}}\right)^4 \left(\frac{m_\zeta}{100 \text{ MeV}}\right)^2,\end{aligned}\tag{B.1}$$

where y_f (m_f) is the Yukawa coupling (mass) of the relevant fermion, m_{h^0} is the physical Higgs mass, v is the relative velocity, and s is the squared center-of-mass energy. We have ignored the phase space suppression in the last estimate, and have used typical masses and mixing angles from Figs. 2-2 and 2-3.

Comparing the scattering and Hubble rates at $T = m_\zeta$, we have

$$\left.\frac{\Gamma}{H}\right|_{T=m_\zeta} \simeq \frac{m_\zeta^3 \sigma v}{g_*(m_\zeta^2/M_{pl})} \approx 10^{-7} \left(\frac{g_*}{50}\right) \left(\frac{m_\zeta}{100 \text{ MeV}}\right) \left(\frac{\sigma v}{10^{-14} \text{ pb}}\right),\tag{B.2}$$

where g_* is the number of degrees of freedom in equilibrium at this temperature. The scattering rate is much smaller than the Hubble rate, implying that the pseudo-goldstino freezes out while relativistic.

Appendix C

Neutralino Decay Widths

In order to calculate the neutralino decay rates for Sec. 2.4.3, we have to account for the fact that a neutralino LOSP is in general an admixture of the higgsinos, gauginos, r -inos, and x -ino. The values of the soft parameters determine the relative fractions of these components, which is especially important when the scale of R -violation in the visible sector is small.

The generalization of Fig. 2-8 is shown in Fig. C-1. Taking into account all of the mixings at tree-level and following the treatment in Ref. [84], we obtain the partial

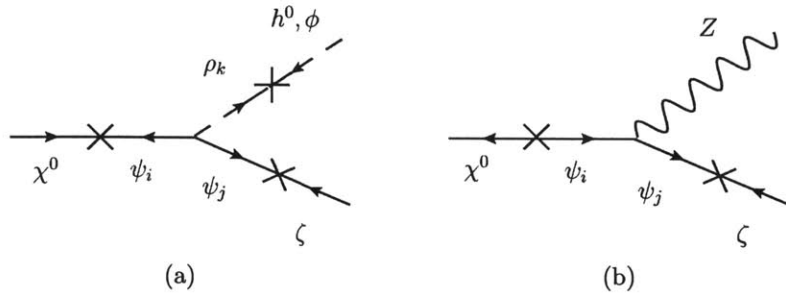


Figure C-1: Illustrations of the general structure contributing to the neutralino LOSP decay to a pseudo-goldstino. The left figure shows the decays to scalars h^0 and ϕ , while the right figure shows the decay to the Z . The fermion interaction eigenstates contributing to the decay are $\psi = \{\tilde{x}, \tilde{h}_u^0, \tilde{h}_d^0, \tilde{r}_u^0, \tilde{r}_d^0, \tilde{B}, \tilde{W}_3\}$, and the relevant scalar interaction eigenstates are $\rho = \{x, h_u^0, h_d^0, r_u^0, r_d^0\}$.

widths

$$\Gamma(\chi^0 \rightarrow Z + \zeta) = \frac{g^2 m_{\chi^0}}{64\pi \cos^2 \theta_w} |\alpha_1|^2 \left(1 - \frac{m_Z^2}{m_{\chi^0}^2}\right) \left(1 - 2\frac{m_Z^2}{m_{\chi^0}^2}\right), \quad (\text{C.1})$$

$$\Gamma(\chi^0 \rightarrow h^0 + \zeta) = \frac{m_{\chi^0}}{64\pi} |\alpha_2|^2 \left(1 - \frac{m_{h^0}^2}{m_{\chi^0}^2}\right)^2, \quad (\text{C.2})$$

$$\Gamma(\chi^0 \rightarrow \phi + \zeta) = \frac{m_{\chi^0}}{64\pi} |\alpha_3|^2 \left(1 - \frac{m_\phi^2}{m_{\chi^0}^2}\right)^2, \quad (\text{C.3})$$

where the relevant combinations of the mixing angles are

$$\alpha_1 = \Theta_{\tilde{r}_d, \zeta}^* \Theta_{\tilde{r}_d, \chi^0} - \Theta_{\tilde{r}_u, \zeta}^* \Theta_{\tilde{r}_u, \chi^0}, \quad (\text{C.4})$$

$$\begin{aligned} \alpha_2 = & (\Theta_{\tilde{r}_u, h^0}^* \Theta_{\tilde{r}_u, \zeta} - \Theta_{\tilde{r}_d, h^0}^* \Theta_{\tilde{r}_d, \zeta})(g' \Theta_{\tilde{B}, \chi^0} - g \Theta_{\tilde{W}, \chi^0}) \\ & + \sqrt{2} \lambda \Theta_{\tilde{x}, \zeta} (\Theta_{\tilde{h}_u, \chi^0} \Theta_{\tilde{h}_d, h^0} - \Theta_{\tilde{h}_d, \chi^0} \Theta_{\tilde{h}_u, h^0}), \end{aligned} \quad (\text{C.5})$$

$$\alpha_3 = (\Theta_{\tilde{r}_u, \phi}^* \Theta_{\tilde{r}_u, \zeta} - \Theta_{\tilde{r}_d, \phi}^* \Theta_{\tilde{r}_d, \zeta})(g' \Theta_{\tilde{B}, \chi^0} - g \Theta_{\tilde{W}, \chi^0}),$$

and we have neglected terms that depend on the mixing of the higgsinos and gauginos with the pseudo-goldstino. In all these expressions, the pseudo-goldstino is approximated as massless.

Appendix D

Inverting Jet Multiplicity

In Sec. 4.2, we want to find the pseudo-inverse of $\tilde{N}_{\text{jet}}(p_{T\text{cut}}, R)$ as a function of $p_{T\text{cut}}$ to get the function $\tilde{p}_T(n, R)$. Here, we provide a computationally efficient way to perform this inverse. Consider a general function of the form

$$f(c) = \sum_{i=1}^N f_i \Theta(c_i - c), \quad (\text{D.1})$$

where f_i and c_i are properties of the i -th particle, and c is some value of a cut. We wish to calculate the pseudo-inverse $c(f)$, which exists because $f(c)$ is a monotonically decreasing function of c . There is an ambiguity in the inverse because $f(c)$ is a step-wise function (with N steps), so there exists a range of values for c with the same value of f .

First, construct a list of length N with all of the values of c_i , keeping track of the corresponding value of f_i for each entry:

$$\{\{c_1, f_1\}, \{c_2, f_2\}, \dots, \{c_N, f_N\}\}. \quad (\text{D.2})$$

This list can be sorted from highest value of c_i to lowest value of c_i with computational scaling $N \log N$. Let i_j be the particle number i for the j -th highest element in the

sorted list:

$$\{\{c_{i_1}, f_{i_1}\}, \{c_{i_2}, f_{i_2}\}, \dots, \{c_{i_N}, f_{i_N}\}\}, \quad (\text{D.3})$$

with $c_{i_1} > c_{i_2} > \dots > c_{i_N}$. (If there are two value of c_i that are truly identical, one can add a small offset to arbitrarily break the degeneracy.)

From the sorted list, one then calculates the cumulative totals for the corresponding f_{i_j} :

$$\{\{c_{i_1}, f_{i_1}\}, \{c_{i_2}, f_{i_1} + f_{i_2}\}, \dots, \{c_{i_N}, \sum_{j=1}^N f_{i_j}\}\}. \quad (\text{D.4})$$

Eq. (D.4) gives the function $f(c)$. To find the pseudo-inverse $c(f)$, one finds the value of J such that

$$\sum_{j=1}^J f_{i_j} < f < \sum_{j=1}^{J+1} f_{i_j}. \quad (\text{D.5})$$

(For a sorted list, the computational cost of searching scales like $\log N$.) The pseudo-inverse $c(f)$ can then take on any value between c_{i_J} and $c_{i_{J+1}}$. For concreteness, we use

$$c(f) = c_{i_{J+1}}, \quad (\text{D.6})$$

which makes sure that calculating $\tilde{p}_T(n, R)$ with $0 < n_{\text{off}} < 1$ on infinitely narrow jets gives back the p_T of the n -th jet.

Bibliography

- [1] An update to the combined search for the Standard Model Higgs boson with the ATLAS detector at the LHC using up to 4.9 fb^{-1} of pp collision data at $\sqrt{s} = 7 \text{ TeV}$. Technical Report ATLAS-CONF-2012-019, CERN, Geneva, Mar 2012.
- [2] Combination of sm, sm4, fp higgs boson searches. Technical Report CMS-PAS-HIG-12-008, CERN, Geneva, 2012.
- [3] Combined coupling measurements of the Higgs-like boson with the ATLAS detector using up to 25 fb^{-1} of proton-proton collision data. 2013.
- [4] Measurements of the properties of the Higgs-like boson in the four lepton decay channel with the ATLAS detector using 25 fb^{-1} of proton-proton collision data. 2013.
- [5] Combination of standard model Higgs boson searches and measurements of the properties of the new boson with a mass near 125 GeV. 2013.
- [6] Properties of the Higgs-like boson in the decay $H \rightarrow ZZ \rightarrow 4l$ in pp collisions at $\sqrt{s} = 7$ and 8 TeV. 2013.
- [7] Update on the search for the standard model Higgs boson in pp collisions at the LHC decaying to $W + W$ in the fully leptonic final state. 2013.
- [8] Georges Aad et al. Measurement of event shapes at large momentum transfer with the ATLAS detector in pp collisions at $\sqrt{s} = 7 \text{ TeV}$. *Eur.Phys.J.*, C72:2211, 2012.
- [9] Georges Aad et al. Observation of a new particle in the search for the Standard Model Higgs boson with the ATLAS detector at the LHC. *Phys.Lett.*, B716:1–29, 2012.
- [10] Georges Aad et al. Performance of jet substructure techniques for large- R jets in proton-proton collisions at $\sqrt{s} = 7 \text{ TeV}$ using the ATLAS detector. *JHEP*, 1309:076, 2013.
- [11] T. Aaltonen et al. Measurement of Event Shapes in Proton-Antiproton Collisions at Center-of-Mass Energy 1.96 TeV. *Phys.Rev.*, D83:112007, 2011.

- [12] G. Abbiendi et al. Measurement of event shape distributions and moments in $e^+e^- \rightarrow j$ hadrons at 91-GeV - 209-GeV and a determination of $\alpha(s)$. *Eur. Phys. J.*, C40:287–316, 2005.
- [13] J. Abdallah et al. A Study of the energy evolution of event shape distributions and their means with the DELPHI detector at LEP. *Eur. Phys. J.*, C29:285–312, 2003.
- [14] A. Abdesselam, E. Bergeaas Kuutmann, U. Bitenc, G. Brooijmans, J. Butterworth, et al. Boosted objects: A Probe of beyond the Standard Model physics. *Eur.Phys.J.*, C71:1661, 2011.
- [15] P. Achard et al. Studies of hadronic event structure in e^+e^- annihilation from 30-GeV to 209-GeV with the L3 detector. *Phys.Rept.*, 399:71–174, 2004.
- [16] P.A.R. Ade et al. BICEP2 I: Detection Of B-mode Polarization at Degree Angular Scales. 2014.
- [17] A. Altheimer, S. Arora, L. Asquith, G. Brooijmans, J. Butterworth, et al. Jet Substructure at the Tevatron and LHC: New results, new tools, new benchmarks. *J.Phys.*, G39:063001, 2012.
- [18] Johan Alwall, Michel Herquet, Fabio Maltoni, Olivier Mattelaer, and Tim Stelzer. MadGraph 5 : Going Beyond. *JHEP*, 1106:128, 2011.
- [19] Sarah Andreas, Chiara Arina, Thomas Hambye, Fu-Sin Ling, and Michel H.G. Tytgat. A light scalar WIMP through the Higgs portal and CoGeNT. *Phys.Rev.*, D82:043522, 2010.
- [20] L. Angelini, P. De Felice, M. Maggi, G. Nardulli, L. Nitti, et al. Jet analysis by deterministic annealing. *Phys.Lett.*, B545:315–322, 2002.
- [21] L. Angelini, G. Nardulli, L. Nitti, M. Pellicoro, D. Perrino, et al. Deterministic annealing as a jet clustering algorithm in hadronic collisions. *Phys.Lett.*, B601:56–63, 2004.
- [22] Riccardo Argurio, Zohar Komargodski, and Alberto Mariotti. Pseudo-Goldstini in Field Theory. *Phys.Rev.Lett.*, 107:061601, 2011.
- [23] Aleksandr Azatov, Roberto Contino, Daniele Del Re, Jamison Galloway, Marco Grassi, et al. Determining Higgs couplings with a model-independent analysis of h to $\gamma\gamma$. 2012.
- [24] Aleksandr Azatov, Roberto Contino, and Jamison Galloway. Model-Independent Bounds on a Light Higgs. *JHEP*, 1204:127, 2012.
- [25] Andrea Banfi, Gavin P. Salam, and Giulia Zanderighi. Resummed event shapes at hadron - hadron colliders. *JHEP*, 0408:062, 2004.

- [26] Andrea Banfi, Gavin P. Salam, and Giulia Zanderighi. Phenomenology of event shapes at hadron colliders. *JHEP*, 1006:038, 2010.
- [27] Brian Batell, Stefania Gori, and Lian-Tao Wang. Exploring the Higgs Portal with 10/fb at the LHC. *JHEP*, 1206:172, 2012.
- [28] Brando Bellazzini, Csaba Csaki, Adam Falkowski, and Andreas Weiler. Buried Higgs. *Phys.Rev.*, D80:075008, 2009.
- [29] Karim Benakli and Cesar Moura. Brane-Worlds Pseudo-Goldstinos. *Nucl.Phys.*, B791:125–163, 2008.
- [30] C.F. Berger, Edmond L. Berger, P.C. Bhat, J.M. Butterworth, S.D. Ellis, et al. Snowmass 2001: Jet energy flow project. *eConf*, C010630:P512, 2001.
- [31] J. Beringer et al. Review of particle physics. *Phys.Rev.*, D86, 2012.
- [32] Daniele Bertolini, Tucker Chan, and Jesse Thaler. Jet Observables Without Jet Algorithms. *JHEP*, 1404:013, 2014.
- [33] Daniele Bertolini and Matthew McCullough. The Social Higgs. *JHEP*, 1212:118, 2012.
- [34] Daniele Bertolini, Keith Rehermann, and Jesse Thaler. Visible Supersymmetry Breaking and an Invisible Higgs. *JHEP*, 1204:130, 2012.
- [35] Daniele Bertolini, Jesse Thaler, and Zachary Thomas. TASI 2012: Super-Tricks for Superspace. 2013.
- [36] Matthew Bowen, Yanou Cui, and James D. Wells. Narrow trans-TeV Higgs bosons and H to hh decays: Two LHC search paths for a hidden sector Higgs boson. *JHEP*, 0703:036, 2007.
- [37] Matthew R. Buckley and Dan Hooper. Are There Hints of Light Stops in Recent Higgs Search Results? 2012.
- [38] C.P. Burgess, Maxim Pospelov, and Tonnis ter Veldhuis. The Minimal model of nonbaryonic dark matter: A Singlet scalar. *Nucl.Phys.*, B619:709–728, 2001.
- [39] J.M. Butterworth, Jeffrey R. Forshaw, and M.H. Seymour. Multiparton interactions in photoproduction at HERA. *Z.Phys.*, C72:637–646, 1996.
- [40] Jonathan M. Butterworth, Adam R. Davison, Mathieu Rubin, and Gavin P. Salam. Jet substructure as a new Higgs search channel at the LHC. *Phys.Rev.Lett.*, 100:242001, 2008.
- [41] Matteo Cacciari and Gavin P. Salam. Pileup subtraction using jet areas. *Phys.Lett.*, B659:119–126, 2008.

- [42] Matteo Cacciari, Gavin P. Salam, and Gregory Soyez. The Anti-k(t) jet clustering algorithm. *JHEP*, 0804:063, 2008.
- [43] Matteo Cacciari, Gavin P. Salam, and Gregory Soyez. The Catchment Area of Jets. *JHEP*, 0804:005, 2008.
- [44] Matteo Cacciari, Gavin P. Salam, and Gregory Soyez. FastJet User Manual. *Eur.Phys.J.*, C72:1896, 2012.
- [45] Dean Carmi, Adam Falkowski, Eric Kuflik, and Tomer Volansky. Interpreting LHC Higgs Results from Natural New Physics Perspective. 2012.
- [46] Dean Carmi, Adam Falkowski, Eric Kuflik, Tomer Volansky, and Jure Zupan. Higgs After the Discovery: A Status Report. 2012.
- [47] S. Catani, Yuri L. Dokshitzer, M.H. Seymour, and B.R. Webber. Longitudinally invariant K_t clustering algorithms for hadron hadron collisions. *Nucl.Phys.*, B406:187–224, 1993.
- [48] Spencer Chang, Radovan Dermisek, John F. Gunion, and Neal Weiner. Non-standard Higgs Boson Decays. *Ann. Rev. Nucl. Part. Sci.*, 58:75–98, 2008.
- [49] Spencer Chang, Can Kilic, and Rakhi Mahbubani. The new fat Higgs: Slimmer and more attractive. *Phys. Rev.*, D71:015003, 2005.
- [50] Serguei Chatrchyan et al. Combined results of searches for the standard model Higgs boson in pp collisions at $\sqrt{s} = 7$ TeV. *Phys.Lett.*, B710:26–48, 2012.
- [51] Serguei Chatrchyan et al. Observation of a new boson at a mass of 125 GeV with the CMS experiment at the LHC. *Phys.Lett.*, B716:30–61, 2012.
- [52] Serguei Chatrchyan et al. Studies of jet mass in dijet and W/Z + jet events. *JHEP*, 1305:090, 2013.
- [53] S. Chekanov. A New jet algorithm based on the k-means clustering for the reconstruction of heavy states from jets. *Eur.Phys.J.*, C47:611–616, 2006.
- [54] Hsin-Chia Cheng, Wei-Chih Huang, Ian Low, and Arjun Menon. Goldstini as the decaying dark matter. *JHEP*, 1103:019, 2011.
- [55] Clifford Cheung, Francesco D’Eramo, and Jesse Thaler. Supergravity Computations without Gravity Complications. 2011.
- [56] Clifford Cheung, Francesco D’Eramo, and Jesse Thaler. The Spectrum of Goldstini and Modulini. *JHEP*, 1108:115, 2011.
- [57] Clifford Cheung, Jeremy Mardon, Yasunori Nomura, and Jesse Thaler. A Definitive Signal of Multiple Supersymmetry Breaking. *JHEP*, 1007:035, 2010.

- [58] Clifford Cheung, Yasunori Nomura, and Jesse Thaler. Goldstini. *JHEP*, 1003:073, 2010.
- [59] Yang-Ting Chien. Telescoping Jets: Multiple Event Interpretations with Multiple R's. 2013.
- [60] S.Y. Choi, D. Choudhury, A. Freitas, J. Kalinowski, and P.M. Zerwas. The Extended Higgs System in R -symmetric Supersymmetry Theories. *Phys.Lett.*, B697:215–221, 2011.
- [61] Timothy Cohen, Eder Izaguirre, Mariangela Lisanti, and Hou Keong Lou. Jet Substructure by Accident. *JHEP*, 1303:161, 2013.
- [62] CMS Collaboration. Search for a Standard Model-like Higgs boson decaying into $WW \rightarrow l \nu q \bar{q}$ in pp collisions at $\sqrt{s} = 8$ TeV. 2013.
- [63] CMS Collaboration. Search for a standard model like Higgs boson in the decay channel $H \rightarrow ZZ \rightarrow l+l- q \bar{q}$ at CMS. 2013.
- [64] The ATLAS collaboration. Search for a high-mass Higgs boson in the $H \rightarrow WW \rightarrow l\nu l\nu$ decay channel with the ATLAS detector using 21 fb^{-1} of proton-proton collision data. 2013.
- [65] Tyler Corbett, O.J.P. Eboli, J. Gonzalez-Fraile, and M.C. Gonzalez-Garcia. Constraining anomalous Higgs interactions. 2012.
- [66] G. Corcella, I.G. Knowles, G. Marchesini, S. Moretti, K. Odagiri, et al. HERWIG 6.5 release note. 2002.
- [67] G. Cowan. *Statistical data analysis*. 1998.
- [68] Glen Cowan, Kyle Cranmer, Eilam Gross, and Ofer Vitells. Asymptotic formulae for likelihood-based tests of new physics. *Eur.Phys.J.*, C71:1554, 2011.
- [69] Nathaniel Craig, John March-Russell, and Matthew McCullough. The Goldstini Variations. *JHEP*, 1010:095, 2010.
- [70] Nathaniel Craig, Daniel Stolarski, and Jesse Thaler. A Fat Higgs with a Magnetic Personality. 2011.
- [71] Csaba Csaki, Yuri Shirman, and John Terning. A Seiberg Dual for the MSSM: Partially Composite W and Z. 2011.
- [72] Mrinal Dasgupta, Alessandro Fregoso, Simone Marzani, and Alexander Powlung. Jet substructure with analytical methods. 2013.
- [73] Mrinal Dasgupta, Alessandro Fregoso, Simone Marzani, and Gavin P. Salam. Towards an understanding of jet substructure. *JHEP*, 1309:029, 2013.

- [74] Mrinal Dasgupta and Gavin P. Salam. Event shapes in e^+e^- annihilation and deep inelastic scattering. *J. Phys.*, G30:R143, 2004.
- [75] Hooman Davoudiasl, Ryuichiro Kitano, Tianjun Li, and Hitoshi Murayama. The New minimal standard model. *Phys.Lett.*, B609:117–123, 2005.
- [76] S. Dawson. Radiative corrections to Higgs boson production. *Nucl.Phys.*, B359:283–300, 1991.
- [77] S. Dawson and R.P. Kauffman. Higgs boson plus multi - jet rates at the SSC. *Phys.Rev.Lett.*, 68:2273–2276, 1992.
- [78] A. De Rujula. To be or not to be: Higgs impostors at the LHC. 2010.
- [79] A. De Rujula, Joseph Lykken, Maurizio Pierini, Christopher Rogan, and Maria Spiropulu. Higgs look-alikes at the LHC. *Phys.Rev.*, D82:013003, 2010.
- [80] Antonio Delgado and Timothy M. P. Tait. A fat Higgs with a fat top. *JHEP*, 07:023, 2005.
- [81] A. Djouadi, M. Spira, and P.M. Zerwas. Production of Higgs bosons in proton colliders: QCD corrections. *Phys.Lett.*, B264:440–446, 1991.
- [82] Abdelhak Djouadi, Adam Falkowski, Yann Mambrini, and Jeremie Quevillon. Direct detection of Higgs-portal dark matter at the LHC. 2012.
- [83] Yuri L. Dokshitzer, G.D. Leder, S. Moretti, and B.R. Webber. Better jet clustering algorithms. *JHEP*, 9708:001, 1997.
- [84] Herbi K. Dreiner, Howard E. Haber, and Stephen P. Martin. Two-component spinor techniques and Feynman rules for quantum field theory and supersymmetry. *Phys.Rept.*, 494:1–196, 2010.
- [85] Sonia El Hedri, Anson Hook, Martin Jankowiak, and Jay G. Wacker. Learning How to Count: A High Multiplicity Search for the LHC. *JHEP*, 1308:136, 2013.
- [86] John Ellis and Tevong You. Global Analysis of the Higgs Candidate with Mass 125 GeV. 2012.
- [87] R. Keith Ellis, I. Hinchliffe, M. Soldate, and J.J. van der Bij. Higgs Decay to $\tau^+\tau^-$: A Possible Signature of Intermediate Mass Higgs Bosons at the SSC. *Nucl.Phys.*, B297:221, 1988.
- [88] S.D. Ellis, J. Huston, K. Hatakeyama, P. Loch, and M. Tonnesmann. Jets in hadron-hadron collisions. *Prog.Part.Nucl.Phys.*, 60:484–551, 2008.
- [89] S.D. Ellis, J. Huston, and M. Tonnesmann. On building better cone jet algorithms. *eConf*, C010630:P513, 2001.

- [90] Stephen D. Ellis, Andrew Hornig, Tuhin S. Roy, David Krohn, and Matthew D. Schwartz. Qjets: A Non-Deterministic Approach to Tree-Based Jet Substructure. *Phys.Rev.Lett.*, 108:182003, 2012.
- [91] Stephen D. Ellis and Davison E. Soper. Successive combination jet algorithm for hadron collisions. *Phys.Rev.*, D48:3160–3166, 1993.
- [92] Stephen D. Ellis, Christopher K. Vermilion, and Jonathan R. Walsh. Techniques for improved heavy particle searches with jet substructure. *Phys.Rev.*, D80:051501, 2009.
- [93] Stephen D. Ellis, Christopher K. Vermilion, and Jonathan R. Walsh. Recombination Algorithms and Jet Substructure: Pruning as a Tool for Heavy Particle Searches. *Phys.Rev.*, D81:094023, 2010.
- [94] Christoph Englert, Tilman Plehn, Dirk Zerwas, and Peter M. Zerwas. Exploring the Higgs portal. *Phys.Lett.*, B703:298–305, 2011.
- [95] J.R. Espinosa, C. Grojean, M. Muhlleitner, and M. Trott. First Glimpses at Higgs’ face. 2012.
- [96] J.R. Espinosa, Christophe Grojean, M. Muhlleitner, and Michael Trott. Fingerprinting Higgs Suspects at the LHC. *JHEP*, 1205:097, 2012.
- [97] Patrick J. Fox, Ann E. Nelson, and Neal Weiner. Dirac gaugino masses and supersoft supersymmetry breaking. *JHEP*, 08:035, 2002.
- [98] Patrick J. Fox, David Tucker-Smith, and Neal Weiner. Higgs friends and counterfeits at hadron colliders. *JHEP*, 1106:127, 2011.
- [99] Pier Paolo Giardino, Kristjan Kannike, Martti Raidal, and Alessandro Strumia. Is the resonance at 125 GeV the Higgs boson? 2012.
- [100] Pier Paolo Giardino, Kristjan Kannike, Martti Raidal, and Alessandro Strumia. Reconstructing Higgs boson properties from the LHC and Tevatron data. 2012.
- [101] G. F. Giudice and A. Masiero. A natural solution to the μ -problem in supergravity theories. *Physics Letters B*, 206:480–484, May 1988.
- [102] Gian F. Giudice, Markus A. Luty, Hitoshi Murayama, and Riccardo Rattazzi. Gaugino mass without singlets. *JHEP*, 9812:027, 1998.
- [103] S.L. Glashow. Partial Symmetries of Weak Interactions. *Nucl.Phys.*, 22:579–588, 1961.
- [104] D. Yu. Grigoriev, E. Jankowski, and F.V. Tkachov. Optimal jet finder. *Comput.Phys.Commun.*, 155:42–64, 2003.
- [105] D. Yu. Grigoriev, E. Jankowski, and F.V. Tkachov. Towards a standard jet definition. *Phys.Rev.Lett.*, 91:061801, 2003.

- [106] CDF Group, D0 Collaborations, the Tevatron New Physics, and Higgs Working. Updated Combination of CDF and D0 Searches for Standard Model Higgs Boson Production with up to 10.0 fb^{-1} of Data. 2012.
- [107] Rick S. Gupta and James D. Wells. Higgs boson search significance deformations due to mixed-in scalars. *Phys.Lett.*, B710:154–158, 2012.
- [108] Howard E. Haber. Introductory low-energy supersymmetry. 1993.
- [109] Kaoru Hagiwara, S. Ishihara, R. Szalapski, and D. Zeppenfeld. Low-energy effects of new interactions in the electroweak boson sector. *Phys.Rev.*, D48:2182–2203, 1993.
- [110] Kaoru Hagiwara, S. Matsumoto, D. Haidt, and C.S. Kim. A Novel approach to confront electroweak data and theory. *Z.Phys.*, C64:559–620, 1994.
- [111] Roni Harnik, Graham D. Kribs, Daniel T. Larson, and Hitoshi Murayama. The minimal supersymmetric fat Higgs model. *Phys. Rev.*, D70:015002, 2004.
- [112] Xiao-Gang He and Jusak Tandeau. Hidden Higgs Boson at the LHC and Light Dark Matter Searches. *Phys.Rev.*, D84:075018, 2011.
- [113] A. Heister et al. Studies of QCD at $e^+ e^-$ centre-of-mass energies between 91-GeV and 209-GeV. *Eur. Phys. J.*, C35:457–486, 2004.
- [114] Anson Hook, Eder Izaguirre, Mariangela Lisanti, and Jay G. Wacker. High Multiplicity Searches at the LHC Using Jet Masses. *Phys.Rev.*, D85:055029, 2012.
- [115] Jay Hubisz, Joseph Lykken, Maurizio Pierini, and Maria Spiropulu. Missing energy look-alikes with 100 pb^{-1} at the LHC. *Phys.Rev.*, D78:075008, 2008.
- [116] K.I. Izawa, Yuichiro Nakai, and Takashi Shimomura. Higgs Portal to Visible Supersymmetry Breaking. *JHEP*, 1103:007, 2011.
- [117] Dilani Kahawala, David Krohn, and Matthew D. Schwartz. Jet Sampling: Improving Event Reconstruction through Multiple Interpretations. *JHEP*, 1306:006, 2013.
- [118] Vardan Khachatryan et al. First Measurement of Hadronic Event Shapes in pp Collisions at $\sqrt{s} = 7 \text{ TeV}$. *Phys.Lett.*, B699:48–67, 2011.
- [119] Bruce Knuteson, Mark Strovink, Bob Olivier, Ursula Bassler, Frederic Fleuret, and Gregorio Bernardi. The missing transverse energy resolution of an event. *DØ Note*, 3629, 1999.
- [120] Zohar Komargodski and David Shih. Notes on SUSY and R-Symmetry Breaking in Wess-Zumino Models. *JHEP*, 04:093, 2009.

- [121] Lawrence M. Krauss and Frank Wilczek. From B Modes to Quantum Gravity and Unification of Forces. 2014.
- [122] Graham D. Kribs, Erich Poppitz, and Neal Weiner. Flavor in supersymmetry with an extended R-symmetry. *Phys.Rev.*, D78:055010, 2008.
- [123] David Krohn, Jesse Thaler, and Lian-Tao Wang. Jet Trimming. *JHEP*, 1002:084, 2010.
- [124] Yue-Shi Lai and Brian A. Cole. Jet reconstruction in hadronic collisions by Gaussian filtering. 2008.
- [125] Andrew J. Larkoski, Duff Neill, and Jesse Thaler. Jet Shapes with the Broadening Axis. 2014.
- [126] Andrew J. Larkoski, Gavin P. Salam, and Jesse Thaler. Energy Correlation Functions for Jet Substructure. 2013.
- [127] Ian Low, Joseph Lykken, and Gabe Shaughnessy. Have We Observed the Higgs (Imposter)? 2012.
- [128] Markus A. Luty. 2004 TASI lectures on supersymmetry breaking. 2005.
- [129] Y. Mambrini. Higgs searches and singlet scalar dark matter: Combined constraints from XENON 100 and the LHC. *Phys.Rev.*, D84:115017, 2011.
- [130] Yann Mambrini. Invisible Higgs and Scalar Dark Matter. 2011.
- [131] John March-Russell, Stephen M. West, Daniel Cumberbatch, and Dan Hooper. Heavy Dark Matter Through the Higgs Portal. *JHEP*, 0807:058, 2008.
- [132] Stephen P. Martin. A Supersymmetry Primer. 1997.
- [133] Matthew McCullough. Stimulated Supersymmetry Breaking. *Phys.Rev.*, D82:115016, 2010.
- [134] John McDonald. Gauge singlet scalars as cold dark matter. *Phys.Rev.*, D50:3637–3649, 1994.
- [135] Marc Montull and Francesco Riva. Higgs discovery: the beginning or the end of natural EWSB? 2012.
- [136] Benjamin Nachman and Christopher G. Lester. Significance Variables. 2013.
- [137] Heinz Pagels and Joel R. Primack. Supersymmetry, Cosmology and New TeV Physics. *Phys. Rev. Lett.*, 48:223, 1982.
- [138] Brian Patt and Frank Wilczek. Higgs-field portal into hidden sectors. 2006.
- [139] R.D. Peccei and Helen R. Quinn. Constraints Imposed by CP Conservation in the Presence of Instantons. *Phys.Rev.*, D16:1791–1797, 1977.

- [140] R.D. Peccei and Helen R. Quinn. CP Conservation in the Presence of Instantons. *Phys.Rev.Lett.*, 38:1440–1443, 1977.
- [141] Michael E. Peskin and Tatsu Takeuchi. A New constraint on a strongly interacting Higgs sector. *Phys.Rev.Lett.*, 65:964–967, 1990.
- [142] Michael E. Peskin and Tatsu Takeuchi. Estimation of oblique electroweak corrections. *Phys.Rev.*, D46:381–409, 1992.
- [143] Martti Raidal and Alessandro Strumia. Hints for a non-standard Higgs boson from the LHC. *Phys.Rev.*, D84:077701, 2011.
- [144] Lisa Randall and Raman Sundrum. Out of this world supersymmetry breaking. *Nucl.Phys.*, B557:79–118, 1999.
- [145] Joshua T. Ruderman and David Shih. General Neutralino NLSPs at the Early LHC. 2011.
- [146] Abdus Salam. Weak and Electromagnetic Interactions. *Conf.Proc.*, C680519:367–377, 1968.
- [147] Abdus Salam and John Clive Ward. Electromagnetic and weak interactions. *Phys.Lett.*, 13:168–171, 1964.
- [148] Gavin P. Salam. Towards Jetography. *Eur.Phys.J.*, C67:637–686, 2010.
- [149] Vanda Silveira and A. Zee. SCALAR PHANTOMS. *Phys.Lett.*, B161:136, 1985.
- [150] Torbjorn Sjostrand, Stephen Mrenna, and Peter Z. Skands. A Brief Introduction to PYTHIA 8.1. *Comput.Phys.Commun.*, 178:852–867, 2008.
- [151] Gregory Soyez, Gavin P. Salam, Jihun Kim, Souvik Dutta, and Matteo Cacciari. Pileup subtraction for jet shapes. *Phys.Rev.Lett.*, 110:162001, 2013.
- [152] M. Spira, A. Djouadi, D. Graudenz, and P.M. Zerwas. Higgs boson production at the LHC. *Nucl.Phys.*, B453:17–82, 1995.
- [153] Iain W. Stewart, Frank J. Tackmann, and Wouter J. Waalewijn. N-Jettiness: An Inclusive Event Shape to Veto Jets. *Phys.Rev.Lett.*, 105:092002, 2010.
- [154] Jesse Thaler and Zachary Thomas. Goldstini Can Give the Higgs a Boost. *JHEP*, 1107:060, 2011.
- [155] Jesse Thaler and Ken Van Tilburg. Identifying Boosted Objects with N-subjettiness. *JHEP*, 1103:015, 2011.
- [156] Jesse Thaler and Ken Van Tilburg. Maximizing Boosted Top Identification by Minimizing N-subjettiness. *JHEP*, 1202:093, 2012.
- [157] The ATLAS collaboration. ATLAS Monte Carlo tunes for MC09. Technical Report ATL-PHYS-PUB-2010-002, 08 Mar 2010.

- [158] Matt Visser. SOME GENERALIZATIONS OF THE O'RAIFEARTAIGH MODEL. *J.Phys.A*, A18:L979, 1985.
- [159] I. Volobouev. FFTJet: A Package for Multiresolution Particle Jet Reconstruction in the Fourier Domain. 2009.
- [160] A Wald. Tests of statistical hypotheses concerning several parameters when the number of observations is large. *Trans. Amer. Math. Soc.*, 54(3):426–482, 1943.
- [161] Steven Weinberg. A Model of Leptons. *Phys.Rev.Lett.*, 19:1264–1266, 1967.
- [162] Steven Weinberg. A New Light Boson? *Phys.Rev.Lett.*, 40:223–226, 1978.
- [163] Frank Wilczek. Problem of Strong p and t Invariance in the Presence of Instantons. *Phys.Rev.Lett.*, 40:279–282, 1978.
- [164] Edward Witten. Constraints on Supersymmetry Breaking. *Nucl. Phys.*, B202:253, 1982.
- [165] M. Wobisch. Measurement and QCD analysis of jet cross-sections in deep inelastic positron proton collisions at $\sqrt{s} = 300$ GeV. 2000.
- [166] M. Wobisch and T. Wengler. Hadronization corrections to jet cross-sections in deep inelastic scattering. 1998.